Underwater Pressure Pulses Generated by Mechanically Alloyed Intermolecular Composites

by

Geoffrey C. Maines

Thesis submitted to the
Faculty of Graduate and Postdoctoral Studies
In partial fulfillment of the requirements
For the M.A.Sc degree in
Mechanical Engineering

Ottawa-Carleton Institute for Mechanical and Aerospace Engineering
Faculty of Engineering
University of Ottawa

Abstract

Recently, the use of thermite-based pressure waves for applications in cellular transfection and drug delivery have shown significant improvements over previous technologies. In the present study, a new technique for producing thermite-generated pressure pulses using fully-dense nano-scale thermite mixtures was evaluated. This was accomplished by evaluation of a stoichiometric mixture of aluminium (Al) and copper(II)-oxide (CuO) prepared by mechanical alloying. Flame propagation speeds, constant-volume pressure characteristics and underwater pressure characteristics of both a micron-scale and mechanically alloyed mixture were measured experimentally and compared with conventional nano-scale thermites. It was determined that mechanically alloyed mixtures are capable of attaining flame propagation speeds on the same order as nano-scale mixtures, with flame speeds reaching as high as approximately 100 m/s. Constant-volume pressure experiments indicated that mechanically alloyed mixtures result in lower pressurization rates compared with conventional nano-scale mixtures, however, an improvement by as much as an order of magnitude was achieved compared with micron-scale mixtures. Thermochemical equilibrium predictions for pressures observed in constant-volume reactions were found to capture relatively well the equilibrium pressure for both low and high values of relative density. Generally, the predictions over-estimated the measured pressures by approximately 60%.

Results from underwater experiments indicated that the mechanically alloyed samples produced peak shock pressures and waveforms similar to those for a nano-scale Al-Bi_2O_3 mixture reported by Apperson *et al.* (2008). In an effort to model the pressure signal obtained from the underwater reaction, calculations were performed based on the rate of expansion of the high pressure gas sphere. Predicted pressures were found to agree fairly well in terms of both the peak pressure and pressurization rate.

The present study has thus identified the ability for mechanically alloyed thermite mixtures to produce underwater pressure profiles that may be conducive for applications in cellular transfection and drug delivery.

Résumé

Récemment, l'utilisation d'ondes de pression produite par des mélanges de thermite pour des applications dans la transfection cellulaire et l'administration de médicaments ont démontré des améliorations importantes par rapport aux technologies précédentes. Dans l'étude ci jointe, une nouvelle technique pour produire des impulsions de pression générée par un mélange thermite, soumit a de l'alliage mécanique, a été évaluée. Ceci a été accompli par l'évaluation d'un mélange stoechiométrique d'aluminium (Al) et de l'oxyde de cuivre(II) (CuO), préparé par mécanosynthèse. Les vitesses de propagation de la flamme, les caractéristiques de pression pour la combustion à volume constant et les caractéristiques de pression pour la combustion sous l'eau ont été mesurées expérimentalement et comparés avec les thermites conventionnel à l'échelle nano. Nous avons déterminé que les mélanges alliés mécaniquement sont capables d'atteindre des vitesses de propagation de flamme du même ordre que les mélanges à l'échelle nanométrique, atteignant jusqu'à environ 100 m/s. Les expériences de combusition à volume constant, indique que les mélanges alliés mécaniquement induit des taux de pressurisation inférieures à celles des mélanges de nano-échelle conventionnel, cependant, une amélioration de près d'un ordre de grandeur a été atteint par rapport aux mélanges d'échelle micronique. Prédictions thermochimiques des pression de combustion se sont révélés capable de relativement bien saisir les valeurs observées dans les expériences à volume constant. En règle générale, les prévisions sur-estimé les pressions mesurées par environ 60% .

Les résultats des expériences sous-marines ont indiqué que les échantillons alliés mécaniquement ont produit des pressions et des profils d'onde similaires à celles produites par un mélange de Al-Bi_2O_3 de nano-échelle, comme indiqué par Apperson *et al.* (2008). Pour modéliser les pressions obtenues dans les expériences sous-marines, des calculs basés sur le taux d'expansion de la bulle de gaz à haute pression ont été obtenus. Les pressions prédites ont été trouvés d'être relativement en accord avec la pression maximale et le taux de pressurisation observé.

Cette étude a ainsi identifié la possibilité pour l'utilisation des mélanges de thermites alliés mécaniquement pour produire des profils de pression sous l'eau propices pour des applications de transfection cellulaire et l'administration de médicaments.

Acknowledgements

I would like to thank my supervisor, Dr. Matei Radulescu, for all his guidance and feedback throughout my academic pursuits, Dr. Antoine Bacciochini for his mentorship and expertise in the laboratory, and Dr. Mohammed Yandouzi for the use of his equipment. I would also like to thank the staff at the University of Ottawa's Faculty of Mechanical Engineering machine shop for their contributions, and everyone involved in the Detonation and Reactive Dynamics Laboratory (DRDL) at the University of Ottawa for their academic help and support. Finally, I would like to thank Defense Research and Development Canada (DRDC), with Dr. Julian Lee and technical authority, for financial support and Dr. Julian Lee for useful discussions throughout this work.

Contents

List of Figures

List of Tables

Nomenclature

Roman Symbols

A	Amplitude fit parameter
C	Specific heat
c	Sound speed
E	Internal energy
e, $\bar{e}$	Specific/Molar internal energy
G	Gibbs free energy
g, $\bar{g}$	Specific/Molar Gibbs free energy
H	Enthalpy
h, $\bar{h}$	Specific/Molar enthalpy
I	Impulse
m	Mass
N	Number of moles
n	Arbitrary number
p	Pressure
Q	Heat addition/release
R	Bubble radius

r	Radial distance
S	Entropy
s, $\bar{s}$	Specific/Molar entropy
T	Temperature
t	Time
V	Velocity
$\forall$	Volume
W	Work
X	Mole fraction
x	Input signal
Y	Mass fraction
y	Output signal
Z	Volume flux

Greek Symbols

α	Smoothing factor
Φ	Equivalence ratio
ϕ	Velocity potential
ρ	Density
τ	Time-scale fit parameter
ξ	Dummy variable

Superscripts

$()^0$	Reference state
$\dot{()}$	Time derivative

Subscripts

$()_{0-9}$ Thermodynamic states

$()_{i,j}$ i^{th} or j^{th} component

$()_p$ Constant pressure process

$()_V$ Constant volume process

Acronyms

ARM Arrested Reactive Milling

BSE Back-Scattered Electron

CEA Chemical Equilibrium with Applications

CJ Chapman-Jouguet

EDS Energy Dispersive Spectrometer

FITC Fluorescein Isothiocyanate-Dextran

fps Frames Per Second

MFU Mean Fluorescent Uptake

PCA Process Control Agent

rpm Revolutions Per Minute

SEM Scanning Electron Microscope

TMD Theoretical Maximum Density

XRD X-Ray Diffraction

Chapter 1

Introduction

1.1 Background

In recent years, pressure pulses produced by piezoelectric generators, gas-driven shock tubes and lasers have shown the capability of transferring genetic material into biological cells. This comes as a result of numerous studies that have identified the ability to delivery drugs and genetic material by pressure-induced permeabilization of the target cells (Lee *et al.*, 2000; Kendall, 2002; Kodama *et al.*, 2003; Koshiyama *et al.*, 2006). Early on, Kodama *et al.* (2000) evaluated the effectiveness of laser- and shock tube-generated pressure pulses on the transfection of two fluorophores into HL-60 leukemia cells. Results indicated that pressure pulses produced by shock tube-based systems were able to successfully deliver both fluorophores into the target cells, while laser-based systems were not. Furthermore, higher peak pressures of the leading wave were found to have little to no effect on transfection rates although survivability rates were significantly compromised. Highest transfection rates were found for waves with the longest impulses, reaching a maximum of approximately 47% for the shock-tube driven pressure waves. These waves had pulse durations of up to 10 μs compared to approximately 200 ns for laser-driven waves.

Since then, advancements in the design of shock tube-based drug delivery systems have been made, most notably by Kodama *et al.* (2002) who were able to increase transfection rates by exposing target cells to multiple pressure pulses and increasing the concentration of fluorophores in the solution. In their investigation, shock waves were used to effectively deliver macromolecules of fluorescein isothiocyanate-dextran (FITC) to NIH:OVCAR-5 cancer cells. In particular, the effects of increasing the number of shock

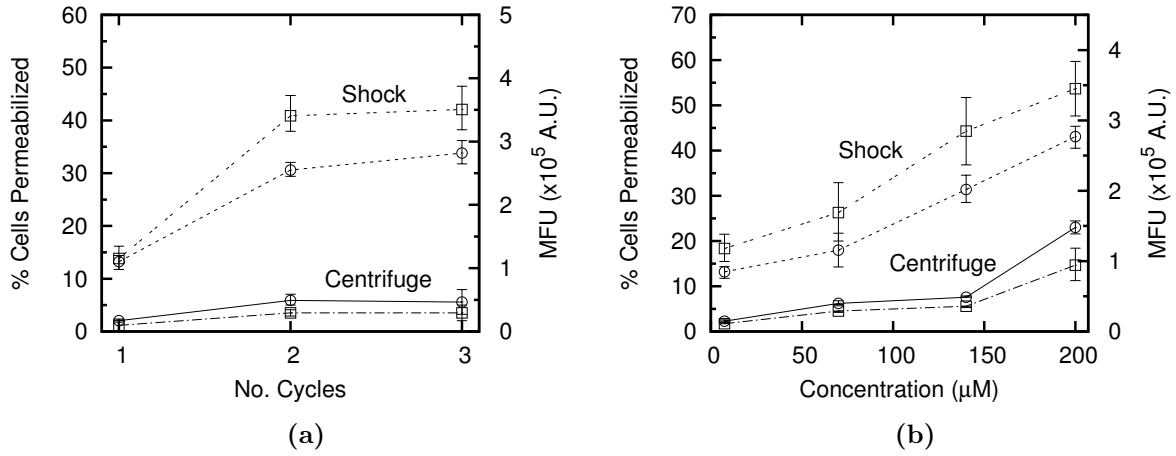

Figure 1.1: Effects of (a) increasing number of shock/centrifuge cycles and (b) increasing concentration of FITC on the permeabilization of living cells with FITC. The efficiency of permeabilization (⊙) is shown on the left axis while the mean fluorescent uptake (MFU) of the cells (⊡) is shown on the right axis, modified from Kodama *et al.* (2002).

pulses transmitted to the target cells and increasing the concentration of FITC in the solution on the permeabilization of the cancer cells were evaluated. To illustrate the benefits of pressure pulsing, a comparison was made between cycles of shock pulsing and centrifuging. The results of this study are presented in Fig. 1.1. Results indicated that transfection efficiencies as high as approximately 35% could be obtained by exposing cells to 3 pressure pulses, and 45% by increasing the concentration of fluorophores from 7.5 to 200 μM. While shock pulsing yielded significantly higher permeabilization efficiencies compared to an equivalent number of centrifuge cycles, modest transfection rates were still observed in all cases. Furthermore, increasing the number of pressure pulses resulted in a decrease in the cell survivability by as much as 5%. As a result, the authors discussed the success of the technology concluding that a compromise between achieving sufficient delivery and causing excessive cellular damage must be made.

While limitations on the control of the pressure dynamics for shock tube-based systems have led to low transfection rates or survival rates of the target cells, significant improvements have been made by implementing thermite mixtures as the constitutive material in generating the pressure waves. This comes as a result of a relatively new finding that certain nano-scale thermites have combustion velocities lower than conven-

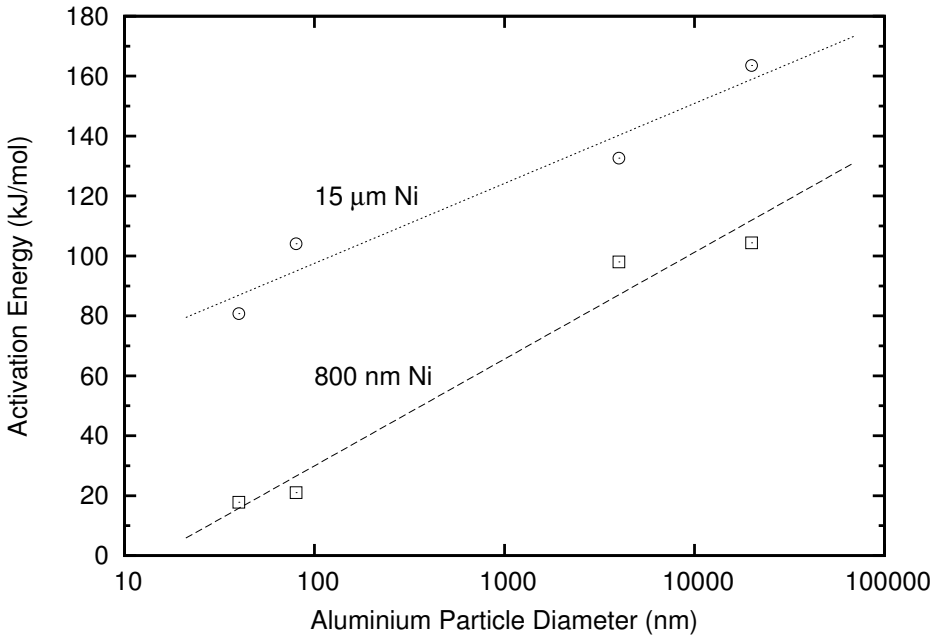

Figure 1.2: Activation energy as a function of Al particle diameter for an Al-Ni intermetallic composite, modified from Hunt & Pantoya (2005).

tional explosives with lower pressures than predicted by Chapman-Jouguet (CJ) theory (Apperson *et al.*, 2007; Shende *et al.*, 2008). Nano-scale thermites, while having energy densities similar to conventional explosives, have less gas production. Furthermore, certain reactive characteristics such as peak pressure and rate of pressure increase have been shown to be modulated by the burning rate. These unique and tunable pressure profiles have been found to be conducive to applications in cellular transfection (Apperson *et al.*, 2008). In their study, pressure pulses produced by the ignition of nano-scale thermites were used to transfect fluorescent plasmids into primary cells, cell lines and tissues. Microchips formed by the consolidation of nano-scale Al-Bi_2O_3 and Al-CuO were used as the driver in generating pressure pulses. In all cases, survivability rates were upwards of 99%, while transfection rates were as high as 99% for primary cells and 60% for cell lines.

1.2 Mechanical alloying

While reductions in particle sizes continuously offer potential advancements in nano-scale energetics, the safety precautions and cost of equipment necessary for proper production,

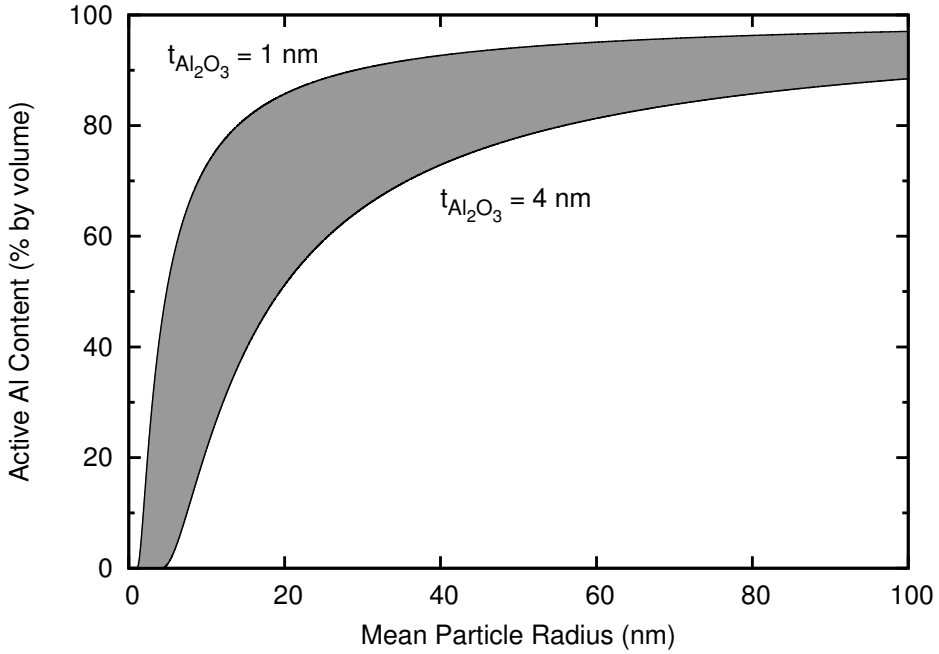

Figure 1.3: Effect of the oxide passivation layer on the active aluminium content of nano-scale particles, modified from Granier *et al.* (2004).

handling and storing of the materials are extensive. One particular issue is the increased sensitivity to thermal ignition for nano-scale mixtures. Compared to micron-scale intermetallic composites, the ignition delay times for nano-scale mixtures are approximately two orders of magnitude shorter while the activation energies are as much as 10 times lower (Hunt & Pantoya, 2005). Results for the activation energy of an aluminium-nickel (Al-Ni) intermetallic composite for increasing Al particle diameter are shown in Fig. 1.2. It was found that the activation energy follows a logarithmic function with aluminium particle diameter. Furthermore, mixtures with smaller Ni particles had significantly lower activations energies. While technological advancements continuously result in smaller particle diameters, these associated lower activation energies increase the material's sensitivity to spontaneous reaction. To avoid complications, special equipment is necessary for proper handling and storing of the materials. As a result, the costs associated with nano-scale materials are significantly amplified compared to their micron-scale counterparts.

Another issue in the preparation of nano-scale mixtures is the presence of an oxide passivation shell surrounding the metal particles. For aluminium, this oxide layer typically has a thickness between 1 and 4 nm (Campbell *et al.*, 1999; Granier *et al.*, 2004).

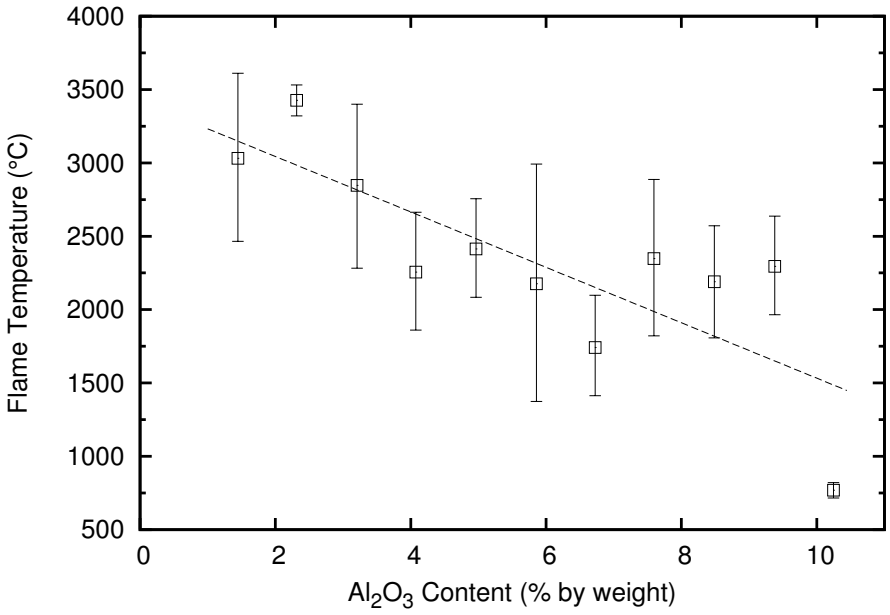

Figure 1.4: Peak flame temperature as a function of Al_2O_3 in the reactants, modified from Granier *et al.* (2004)

As the size of the grains decrease, the content of active aluminium within each particle is exponentially reduced, compromising the purity of the mixture. This effect is shown in Fig. 1.3 where the active content of aluminium particles is shown as a function of the particle radius. In these calculations, the particle sizes were assumed to be spherical with a uniform passivation layer thickness. To evaluate this effect, Granier *et al.* (2004) produced Al-Ni intermetallic composite samples consisting of larger quantities of nano-scale Al and thus Al_2O_3 passivation layers. The peak flame temperatures of the resulting mixtures were evaluated as a function of the Al_2O_3 content. Results indicated that a loss in temperature from approximately 3000°C to 850°C occurred for an increase in Al_2O_3 from 0 to 10%. These results are shown in Fig. 1.4. The loss in reaction temperature for higher Al_2O_3 content was primarily attributed to reductions in the volume of pure Al within each particle.

Recently, a novel method for producing micron-sized, fully dense powders in which the reactive components are uniformly mixed on the nano-scale has shown to be effective in the production of both intermetallic and thermite mixtures (Suryanarayana, 2001). This process, termed *mechanical alloying*, involves the cold welding of metal powders induced by energy deposited into the raw materials by hardened balls in the form of

kinetic energy. In this process, micron-sized powders are formed containing reactive components mixed on the nano-scale. The development of these mechanically alloyed energetic formulations is largely attributed to the pioneering research at the New Jersey Institute of Technology, where the technique has been adopted in the production of a wide variety of energetic formulations. In an early investigation, Schoenitz *et al.* (2004) produced energetic mixtures of Al-Fe_2O_3 and Al-MoO_3 with particles in the range of 1-50 μm containing layered assemblages of the reactants mixed on a 10-100 nm scale. This was accomplished using a technique of arrested reactive milling (ARM), in which the initial materials are mechanically milled to the point just prior to ignition. The resulting increased surface area between the fuel and oxidizer was shown to significantly increase the reactivity of the mixtures, as shown by evaluations of the burn rates.

Since these early investigations, further research on the characterization of the process and resulting material have led to improvements in their production and performance (Schoenitz *et al.*, 2005; Umbrajkar *et al.*, 2006*a*,*b*, 2007; Aly *et al.*, 2013). Most prominently, these studies aimed at optimizing the preparation of the material by identifying the role of milling parameters on the resulting material. In one study, Umbrajkar *et al.* (2006*b*) refined and optimized the process for producing a mechanically alloyed Al-CuO mixture. In their investigation, a highly-pure micron-scale mixture consisting of nano-scale layers of Al and CuO was produced. Mixtures were prepared by use of a shaker mill paired with a process control agent (PCA), which was found to significantly improve the process by inhibiting reactions during milling. A comparison between the initial materials and the resulting mechanically alloyed powder is shown in Fig. 1.5.

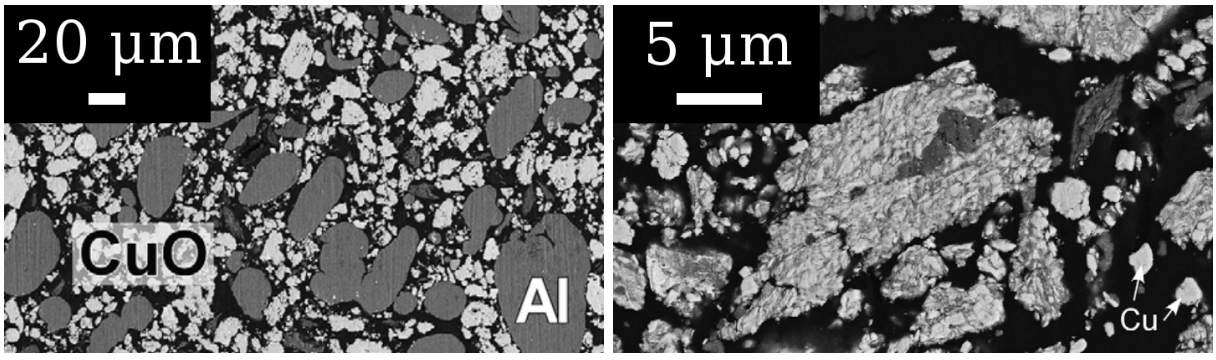

(a) **(b)**

Figure 1.5: SEM images comparing the (a) unmilled and (b) milled 2Al-3CuO mixtures produced by Umbrajkar *et al.* (2006*b*).

Since then, a significant effort has been made towards identifying the thermal and mechanical properties of these materials. Interestingly, it has been shown that the onset of ignition for mechanically alloyed thermite mixtures occurs at relatively low temperatures compared with conventional mixtures (Umbrajkar *et al.*, 2006*b*; Schoenitz *et al.*, 2007; Umbrajkar *et al.*, 2008). In particular, it was determined that the highly exothermic reaction between Al and CuO starts at temperatures as low as 400 K and can be well-described by four parallel reaction steps. Although the bulk energy release was found to occur during the strongest, fourth reaction step, which was found to occur at temperatures of approximately 900 K, it was found that the reaction is primarily driven by the lower-temperature oxidation process. Similar results for the ignition temperature were obtained by Williams *et al.* (2013) and Stamatis *et al.* (2008) who evaluated various mechanically alloyed Al-based mixtures using varying heating rates. Results of their investigations determined that thermal runaway for a mechanically alloyed Al-CuO thermite mixtures occurs at temperatures of approximately 820 K to 980 K for heating rates between 250 K/s and 17,500 K/s. In another investigation, Stamatis *et al.* (2011) evaluated the mechanical properties for consolidated pellets of fully dense nano-scale Al-CuO and Al-MoO_3 prepared via ARM. Results indicated that higher tensile and flexural strengths were observed for higher relative densities, while the strength of composite materials was comparable to that of consolidated aluminium powders. In terms of yield strength, composite materials were found to show higher strengths compared to micron-scale powder blends and consolidated aluminium.

While significant research has been devoted towards investigating the mechanisms governing the reaction kinetics for mixtures prepared by mechanical alloying, minimal effort has been made towards evaluating their combustion performance compared with traditional mixtures.

1.3 Objectives

The present study evaluates a new method for producing thermite-generated pressure pulses in water for applications in cellular transfection. A mixture of aluminium (Al) and copper(II)-oxide (CuO) is prepared via mechanical alloying and compared with results by Umbrajkar *et al.* (2006*b*). Initially, the combustion performance of the assembled mixture is evaluated and compared with conventional micron- and nano-scale thermites via open-channel flame speed measurements and constant-volume pressure measurements. The viability of mechanically alloyed mixtures on attaining flame propagation speeds

and constant-volume pressurization rates similar to conventional nano-scale energetics is discussed. With the performance of the assembled mixture well-characterized, the underwater pressure signatures for both micron-scale and mechanically alloyed mixtures are obtained and compared with results by Apperson *et al.* (2008). Predictions of the constant-volume pressure characteristics of thermite mixtures were obtained using thermochemical equilibrium calculations and compared with experimental data. Finally, a method for estimating the underwater pressure signature from the rate of growth of the gas-bubble is discussed and compared with experiment.

This thesis is organized as follows. The experimental apparatus used in the various experiments is documented in Chapter 2. Details on the experimental procedure are provided in Chapter 3. Results of the mechanical alloying, flame propagation speed measurements, pressure and pressurization measurements at constant-volume and underwater measurements are presented and discussed in Chapter 4. A method for predicting the pressures observed in constant-volume measurements is presented and compared with experimental results in Chapter 5. A method for estimating the pressure profile formed by the expansion of the high-pressure gas bubble in underwater experiments is presented and compared with actual measurements in Chapter 6. Finally, Chapter 7 summarizes the current investigation and draws conclusions from the experimental results and calculations.

Chapter 2

Experimental apparatus

The physical apparatus used to prepare and characterize thermite mixtures are outlined in this chapter. Some equipment was designed and manufactured specifically for these experiments. Descriptions of all major components and their associated instruments are provided.

2.1 Mechanical alloying

2.1.1 Fritsch Pulverisette 7 planetary micro mill

To prepare mechanically alloyed mixtures, a planetary ball mill (Fritsch Pulverisette 7, Fig. 2.1a) was used. The mill consists of a rotating drum supporting two 80 mL tempered steel vials. Each vial contains a quantity of hardened steel balls that crush and re-shape the materials. The vials are sealed using lids mounted with a thermocouple and pressure transducer (Fritsch Easy-GTM). These sensors allow for continuous monitoring of thermal and pressure effects within each of the vials, capturing the onset of chemical reaction of the reactive materials. The vials and lid assembly are rated to a maximum pressure of 1 MPa, which restricts the amount of reactant material that can be refined at once. An additional set of lids was constructed by Akbarnejad (2013) for use in the cleaning phase. The vials and lids are shown in Fig. 2.1b.

2.1.2 Inert atmosphere glovebox

An argon environment was created using a Labconco Precise Controlled Atmosphere Glovebox when loading milling vials with reactant materials. The glovebox consists of

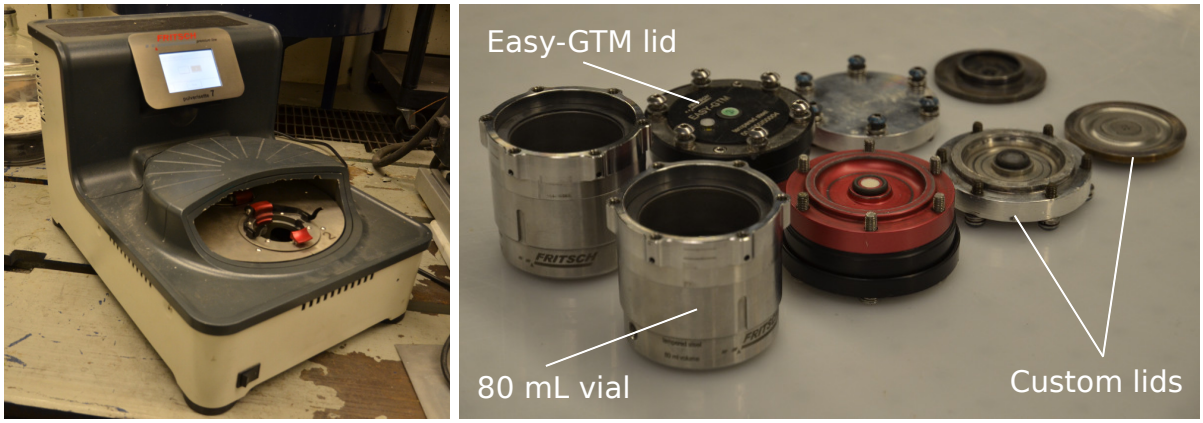

(a) **(b)**

Figure 2.1: Photographs of the (a) Fritsch Pulverisette 7 planetary ball mill and (b) vials and lids used in the mechanical alloying process.

a transfer chamber and a main chamber, both connected to the inlet gas and a vacuum pump. Each chamber is mounted with a pressure gauge to monitor the internal pressure. Argon was used as the inert gas in the preparation of mechanically alloyed samples. The glovebox and its accessories are shown in Fig. 2.2.

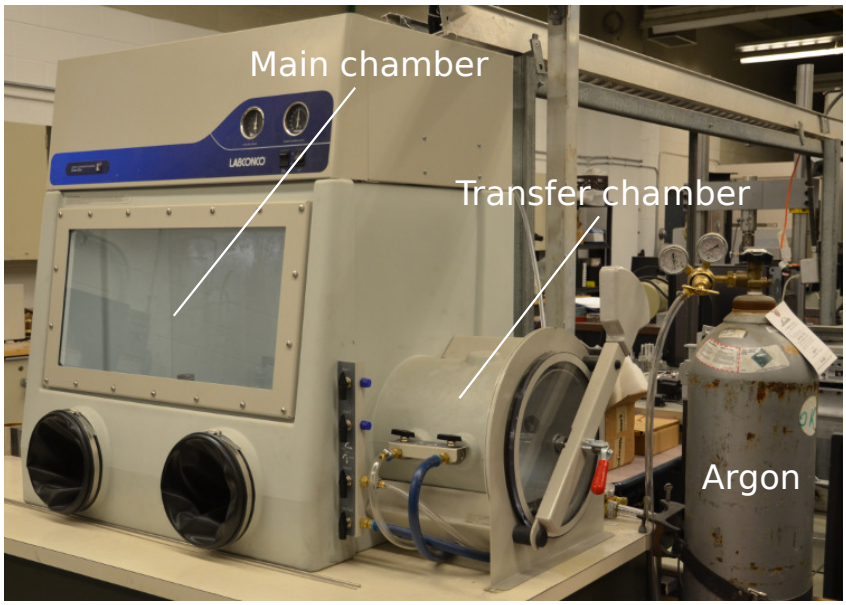

Figure 2.2: Labconco Precise Controlled Atmosphere Glovebox used in creating an argon environment for mechanical alloying.

2.2 Flame speed measurements

Measurements of the flame propagation speed were conducted using a steel channel (Fig. 2.3). The channel consists of two sections; a smaller ignition section, and a measurement section with dimensions 2.5 × 2.5 × 70 mm. All measurements on the flame propagation speeds were conducted in the measurement section of the channel.

In an investigation by Akbarnejad (2013), the effect of heat losses on the flame propagation speed of an Al-Ni intermetallic mixture was evaluated. Heat loss effects were found to be negligible for the channel size used in the current study permitting for accurate measurements of flame propagation speeds.

To capture the reaction event, a Phantom V1210 high-speed camera with an AF Nikkor 80-200mm lens was used. A mirror located approximately 3.0 m from the camera was set at an angle of 45° with the optical table's surface. The filled burn-channel was placed below the mirror during experiments. A schematic representation of the physical setup is shown in Fig. 2.4.

2.3 Combustion vessels

Pressure experiments were conducted using two different combustion vessels, each designed for a specific application. These combustion vessels were designed and manufactured for the current investigation. Details of each combustion vessel are discussed in the following sections.

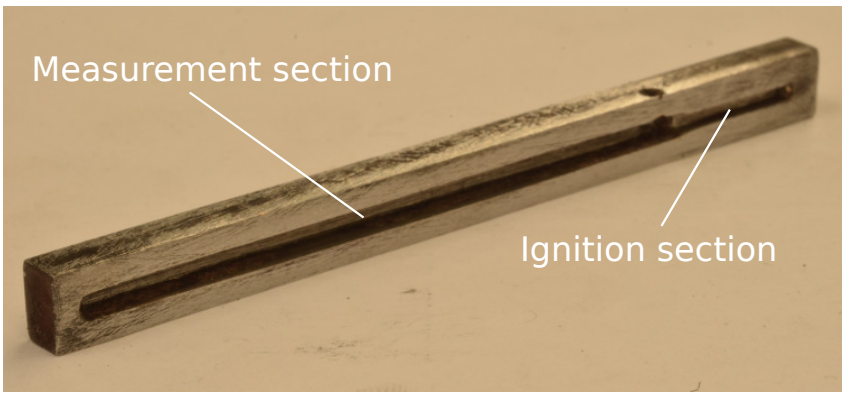

Figure 2.3: Burn-channel used in flame speed measurements.

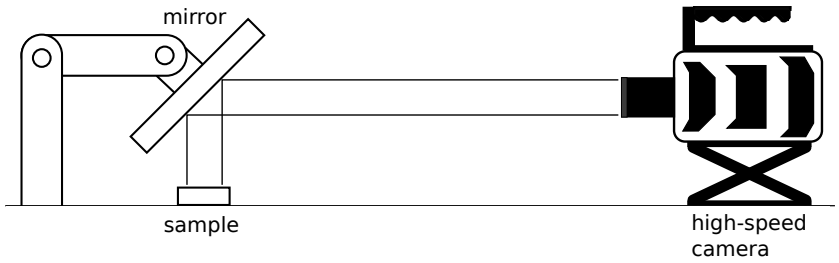

Figure 2.4: Schematic representation of the setup for the measurement of flame propagation speeds.

2.3.1 3.96-mL-custom-designed miniature pressure cell

The 3.96-mL-combustion vessel was primarily used to measure constant-volume combustion characteristics of energetic materials, namely peak pressure and pressurization rate. The vessel contains a cylindrical reaction chamber with a diameter and height of 17.2 mm. The material used in its construction is AISI 304 stainless steel. The vessel consists of two components: a body containing the reaction chamber, an o-ring and a spark plug, and a head containing a pressure transducer. The spark plug's center electrode is attached to a steel rod insulated from the outer walls by a Delrin sleeve that is flush with the base of the reaction chamber. A PCB pressure transducer (Model 113B24) with a maximum pressure of 7 MPa and a rise time of less than 1 μs was used to record pressure data during the experiments. The sensing element was covered with a 1 mm

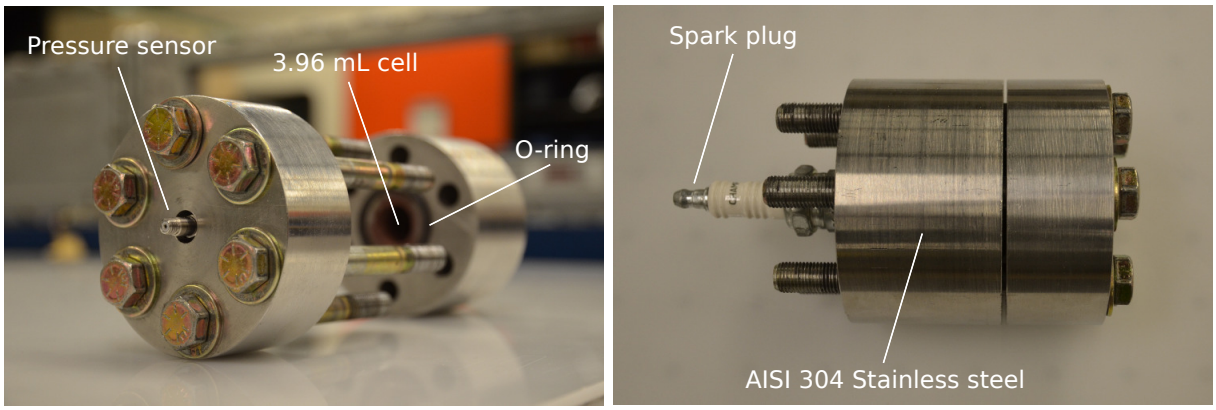

(a) **(b)**

Figure 2.5: Features of the 3.96-mL-combustion vessel depicting the location of the (a) pressure sensor, test cavity and o-ring, and (b) spark plug.

thick silicone film in order to minimize the loss of signal due to heat transfer. The walls of the chamber are 29.5 mm thick, which permits for internal pressures upwards of 20 MPa. The apparatus is shown in Fig. 2.5 identifying the major components and features of its construction. Detailed drawings for the design and construction of the vessel are shown in Appendix D.

2.3.2 1.06-L-custom-designed combustion chamber

The 1.06-L-combustion vessel was used for underwater experiments measuring characteristic wave speeds, bubble expansion rates, and pressures. The vessel has a rectangular internal cavity with dimensions of 101.6 × 101.6 × 95.25 mm and a wall thickness of 60.325 mm. The chamber is constructed from aluminium 6061-T6 and is designed to withstand internal pressures upwards of 50 MPa when sealed with 44.45 mm thick aluminium plates. Six aluminium plugs penetrate the chamber; two for wall-mounted pressure transducers, two for gas- and liquid-handling, one for the ignition system, and one for the submerged pressure transducer. The wall-mounted pressure transducers (PCB Model 113B24) have a maximum pressure of 7 MPa and a rise time of less than 1 μs, while the in-situ pressure transducer (Neptune Sonar Model T11 underwater shock-gauge) has a maximum pressure of 275 MPa and a rise time of less than 4 μs. A spark-plug mounted in a threaded plug on one of the side walls acts as the igniter for the experiments. When op-

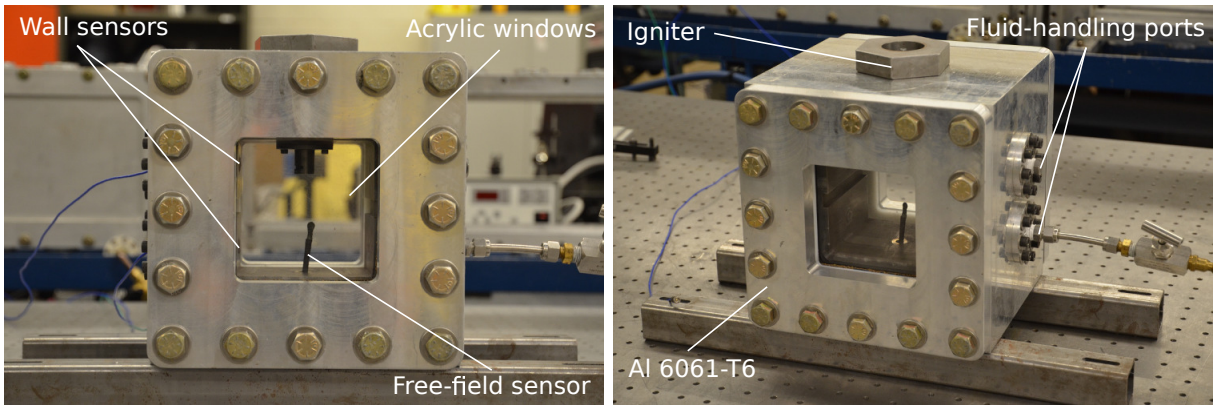

(a) **(b)**

Figure 2.6: Features of the 1.06-L-underwater combustion chamber depicting the location of the (a) pressure sensors and windows, and (b) igniter plug and fluid-handling ports.

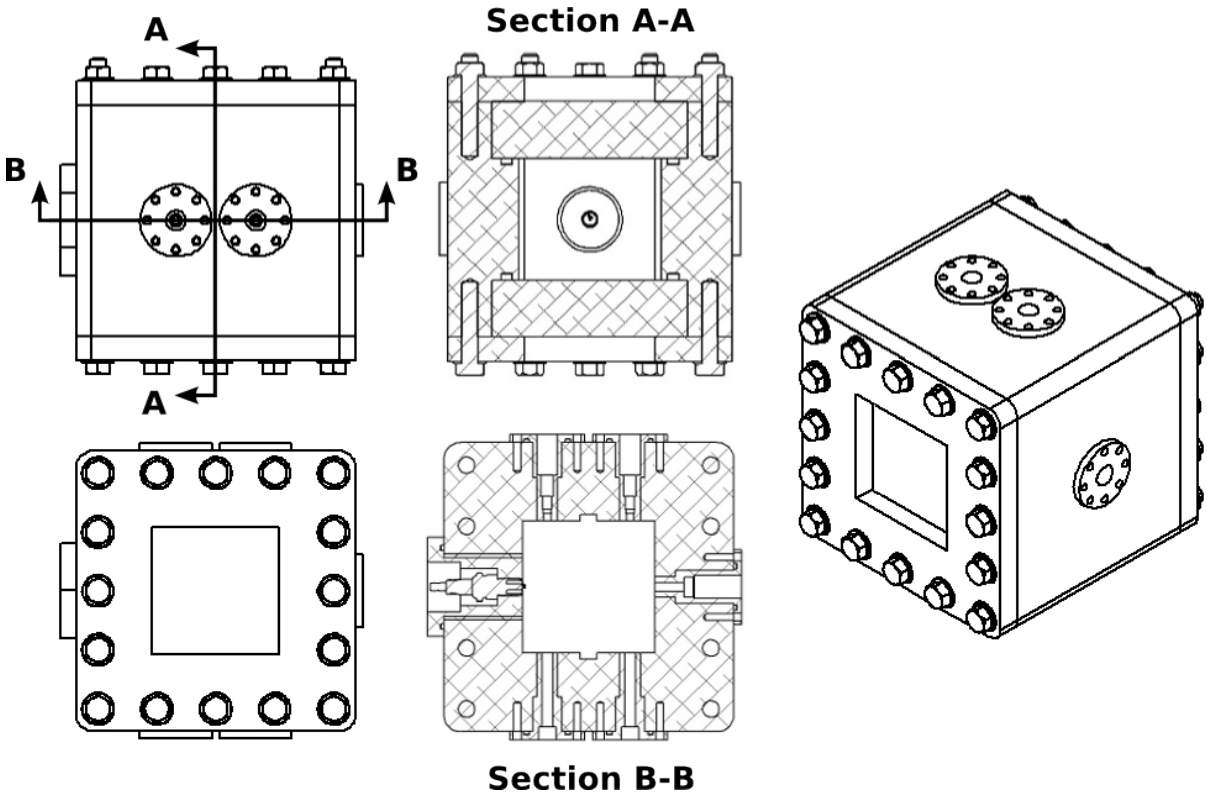

Figure 2.7: Schematic representation of the 1.06-L-combustion vessel showing the external and internal features of the apparatus.

tical measurements were to be made, aluminium plates were replaced with optical-grade acrylic windows, which allow for observations of the combustion event and subsequent phenomena. Photographs of the apparatus detailing its features are shown in Fig. 2.6. A schematic of the vessel is provided in Fig. 2.7. A complete set of detailed drawings is provided in Appendix E.

2.4 Ignition system

The ignition system for both combustion vessels consists of a variable power supply (Hewlett-Packard Harrison 6434B) capable of supplying up to 30 A at 50 V. The power supply was connected to the spark plug housed in the combustion vessel. The reaction event was initiated by hot-wire resistance heating of a tungsten wire. For the miniature pressure cell, a 30 gauge (0.254 mm) tungsten wire running through the sample mixture

was connected between the spark plug and the outer casing, while for the underwater combustion vessel a pre-existing hot-wire filament was embedded in the samples.

2.5 Data acquisition and optical systems

For constant-volume pressure measurements, pressure signals were recorded using a National Instruments data acquisition system (Model PXIe-1073 hub with PXIe-6358 card) connected to a personal computer. The signals from the pressure transducers were amplified and conditioned using a signal conditioner (PCB Model 482C16). A LabVIEW program was used to record the pressure data and control the sampling rate. A schematic representation of the data acquisition system for the miniature pressure cell is shown in Fig. 2.8.

For underwater measurements, pressure signals were recorded using a National Instruments data acquisition card (PCI-6133) connected to a personal computer. The signals from PCB transducers were amplified and conditioned using a signal conditioner (PCB Model 482C05), while the signal from the Neptune Sonar shock-gauge was amplified by a charge amplifier (Kistler Model 504D). Again, the number of samples and sample rate were set within the LabVIEW program.

Schlieren visualization was achieved using an optical setup consisting of a Phantom V1210 high-speed camera, a 1600 W Newport Xenon arc lamp, and two parabolic mirrors arranged in a Z-type pattern (Settles, 2001). A knife-edge in front of the camera cuts the light entering the lens, permitting density gradients within the flow to be visualized.

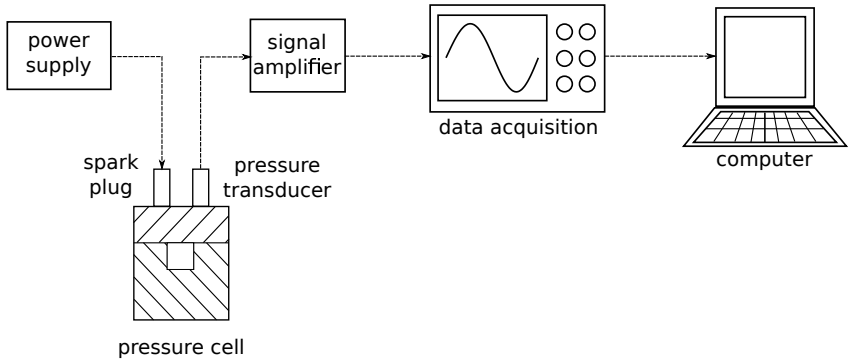

Figure 2.8: Schematic representation of the 3.96-mL-miniature reaction vessel and the corresponding data acquisition system.

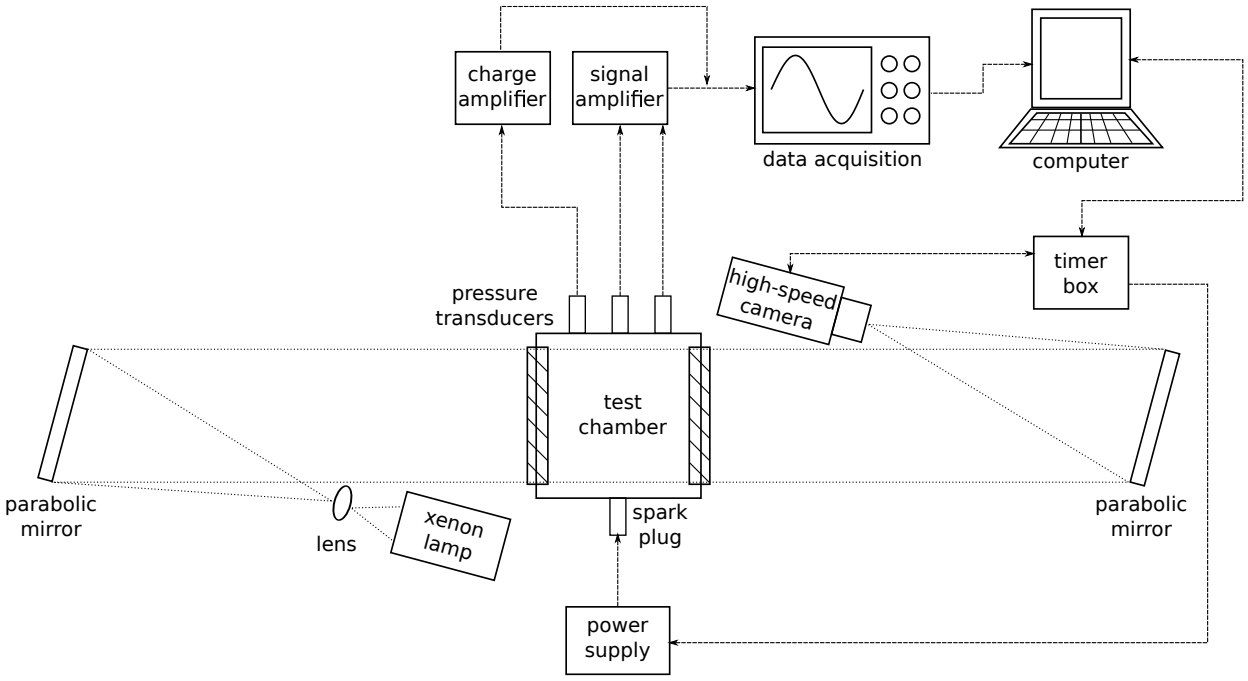

Figure 2.9: Schematic representation of the physical apparatus, optical setup and data acquisition system for the 1.06-L-underwater blast chamber.

The camera and data acquisition system were triggered by a timer box (BNC Model 575 Pulse Generator). The camera was connected to a personal computer outfitted with the Phantom PCC software while the data acquisition system was connected to a personal computer with the LabVIEW program. A schematic representation of the data acquisition system and optical setup for the underwater combustion vessel is shown in Fig. 2.9.

Chapter 3

Experimental procedure

In this chapter, the details of all experimental procedures are provided. Methods utilized in the preparation of mechanically alloyed materials, conduction of open-channel flame propagation speed measurements, measurement of constant volume pressure and pressurization rates and underwater experiments are presented.

3.1 Material preparation

3.1.1 Synthesis

In the present study, aluminium (Al, Atlantic Equipment Engineers AL-101, 99.9% pure, -325 mesh) and copper(II)-oxide (CuO, Atlantic Equipment Engineers CU-602, 99.9% pure, 1-5 μm) were used as the constituent materials. Aluminium powders were sifted for particle sizes less than 32 μm. Properties for both powders are provided in Table 3.1. The microstructure of each individual powder was evaluated using a scanning electron microscope (SEM, Model EVO MA-10, Carl Zeiss NTS GmbH, Germany) equipped with a back-scattered electron (BSE) detector and an energy dispersive spectrometer (EDS) probe (INCA-x-act, Oxford Instruments, United Kingdom). The morphology and particle size of the aluminium and copper(II)-oxide powders are shown in Fig. 3.1a and 3.1b, respectively.

To prepare the sample mixture, raw powders were mechanically blended in stoichiometric proportions of 2:3 by mole of aluminium and copper(II)-oxide. This corresponds to a mixture containing 18.4% Al and 81.6% CuO by mass. To accurately control the amount of each powder used in the mixture, a digital scale accurate to 1 mg was used. The synthesized mixture was then evaluated using scanning electron microscopy to ensure

Table 3.1: Properties for the metals used in the present study.

Property	Al	CuO
Purity (%)	99.9	99.9
Particle Size (μm)	< 32	1-5
Density (kg/m^3)	2700	6310
Molecular Weight (g/mol)	26.98	79.55
Melting Point (°C)	660.1	1326

proper mixing.

3.1.2 Mechanical alloying

To produce mechanically alloyed ball-milled samples, blended powders were placed inside the milling vials containing fifteen hardened steel milling balls of 9.3 mm diameter. Owing to the rated pressure of the vial assembly, the amount of mixture capable of being processed was restricted to approximately 1 g, as estimated using NASA's chemical equilibrium with applications (CEA) package (see Chapter 5). Once the powders were added, the vials were transferred to the glovebox. To ensure that an argon environment was present, argon was cycled through both the main chamber and transfer chamber three times. An oxygen sensor was used to determine the concentration of oxygen in

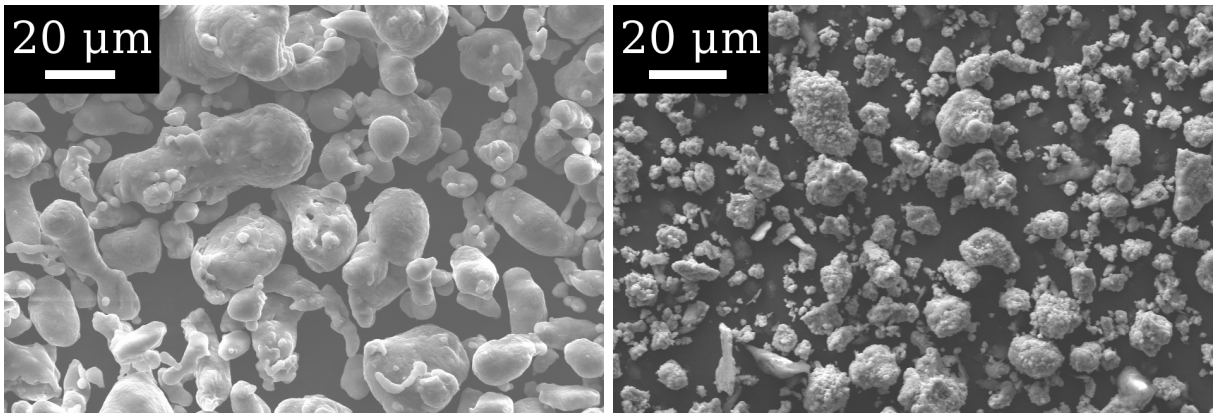

(a) Aluminium (Al) **(b)** Copper(II)-oxide (CuO)

Figure 3.1: Microstructures of the constituent powders obtained using the scanning electron microscope (SEM).

Table 3.2: Details of the samples prepared via mechanical alloying.

Sample No.	Speed (rpm)	Cycle Duration (min/cycle)	No. Cycles	Mill Duration (min)	V_{Hexane} (mL)	m_{powder} (g)	No. balls
1	450	2	8	16	4	1	15
2	450	2	15	30	4	1	15
3	450	2	23	46	4	1	15
4	450	2	30	60	4	1	15

the glovebox, which was sufficiently low ($< 0.25\%$ O_2 by volume) after three cycles. In a process similar to Umbrajkar *et al.* (2006*b*), Hexane (C_6H_{14}) was used as a process control agent (PCA) to inhibit reactions during the milling procedure. Once in the glovebox, 4 mL of Hexane was added to each vial and the vials were sealed. Vials were then placed in the planetary mill. The mill operated at a rotational speed of 450 rpm with a cycle duration of 2 minutes. The direction of rotation was set to reverse at the end of each cycle. The number of cycles was varied to evaluate the mixture at numerous stages of milling. Four milled samples were investigated in this study. Details on the milling parameters are highlighted in Table 3.2.

The pressure sensor and thermocouple on the lid of the vials allowed for continuous monitoring of the milling process. Typical pressure and temperature measurements for a milling cycle are shown in Fig. 3.2 in which pressure and temperature slowly in-

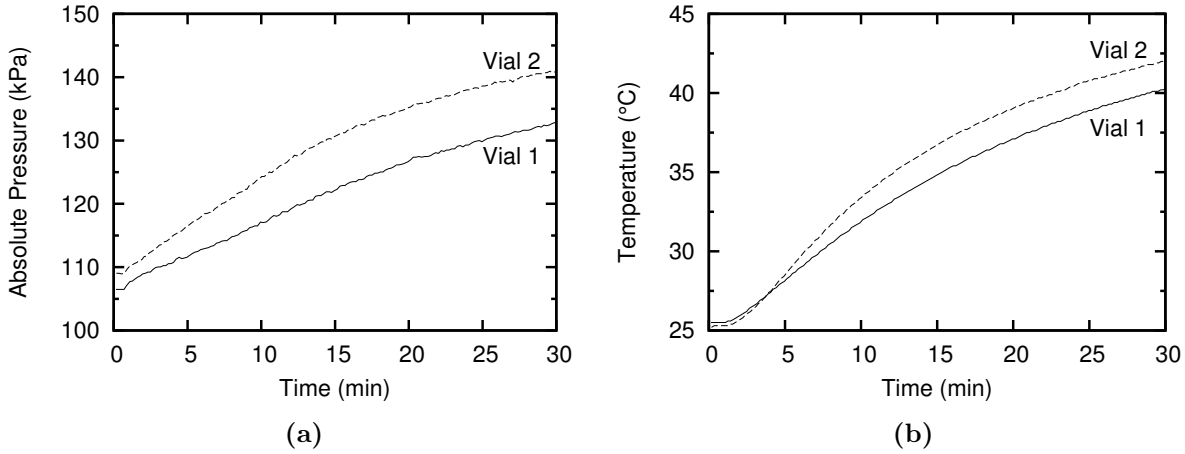

Figure 3.2: Typical curves for the (a) pressure and (b) temperature of the milling vials during mechanical alloying.

crease owing to the dissipation of energy in the form of heat from the grinding balls and surrounding surfaces.

Prior to every milling operation, a cleaning cycle was used to ensure that the grinding balls and vials were free of contaminants. Approximately 10 mL of ethanol (C_2H_6O) was added to each of the vials, which were sealed with the custom lids. Vials were placed in the mill, which operated at a rotational speed of 450 rpm for 15 cycles of 2 minutes, reversing at the end of each cycle. Once completed, the grinding balls, vials and lids were rinsed with water and dried using compressed air.

3.2 Flame propagation speed measurements

To conduct flame propagation speed measurements, powders were added to the channel described in Section 2.2. To ensure that powders were equally distributed within the channel, cycles of adding and agitating small quantities of the sample mixture were implemented. Once filled, the mass of the sample was recorded using a digital scale. In all cases, the mass of the sample was 530 ± 69 mg corresponding to 26.5 ± 3.5% of the theoretical maximum density (TMD). A glass slide was placed over the measurement section of the channel to reduce the volume of gas-phase products expelled in the field of view of the high-speed camera. The setup used for the burn channel is shown in Fig. 3.3.

To initiate the reaction, a butane torch was placed over the ignition section of the

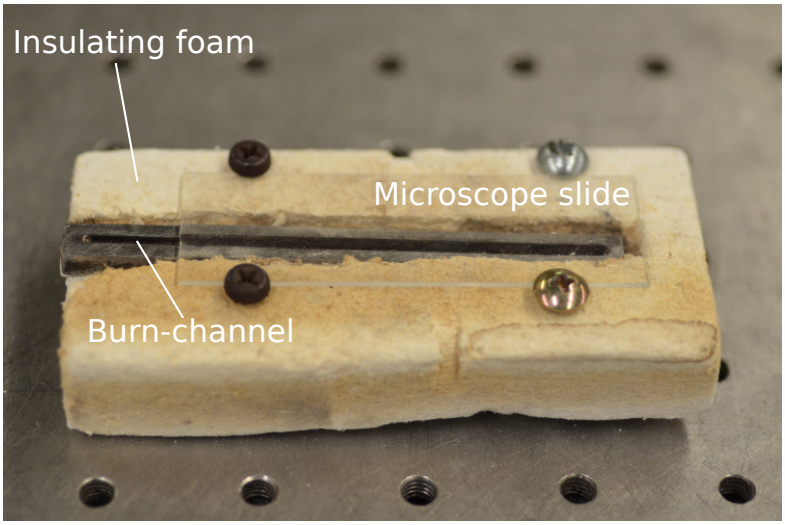

Figure 3.3: Experimental setup for the burn-channel in flame propagation speed measurements.

channel. Depending on the sample, the capture speed of the high-speed camera was adjusted. Capture speeds between 6,000 and 20,000 frames per second (fps) were necessary to accurately capture the reaction event. The aperture of the lens was set to $f/2.8$ while focal length was adjusted such that the channel was completely in focus. The zoom was set such that the channel occupied the entire width of the frame at the set resolution.

Once captured, the frames were extracted from the high-speed videos using FFmpeg, an open-source command-line multimedia conversion software (Bellard, 2000). Analysis of the images was conducted using ImageJ, a java-based image processing software developed at the National Institutes of Health (Rasband, 1997). Using this software, locations of the flame front were accurately measured as a function of time. Linear regressions of the distance-time data allowed for measurements of the average flame propagation speed. Details of the conducted measurements and their results are shown in Table A.1.

3.3 Pressure cell measurements

Pressure cell measurements were conducted in the 3.96-mL-miniature pressure cell discussed in Section 2.3.1. Varying amounts of the sample mixtures were placed inside the cell cavity to determine the effect of relative density on the constant-volume combustion behaviour. Measurements were conducted for relative densities from approximately 0.4% to 5.3% TMD. To measure the mass of the sample, powders were placed on a glass tray and weighed using a digital scale accurate to 1 mg. Once inside the cell cavity, the tungsten wire was coiled and attached to the center electrode and the outer casing, as shown in Fig. 3.4. The vessel was then sealed and attached to the power supply. Data sampling rates of 10-20 kHz and 50 kHz were used for the unmilled and milled powders, respectively.

Upon completion of one experiment, the combustion products were removed from the pressure cell using a rotating wire brush. The cell was then cleaned prior to the next experiment.

To analyze the pressure data, a Python-based script was created to filter the raw data, calculate relevant information and store it in data files. Pressure data was filtered using a simple infinite impulse response filter with a smoothing factor ($0 \leq \alpha \leq 1$) of 0.2. This filter is a time-discretized realization of a low-pass RC filter and is expressed by

$$y_i = \alpha x_i + (1 - \alpha) y_{i-1} \tag{3.1}$$

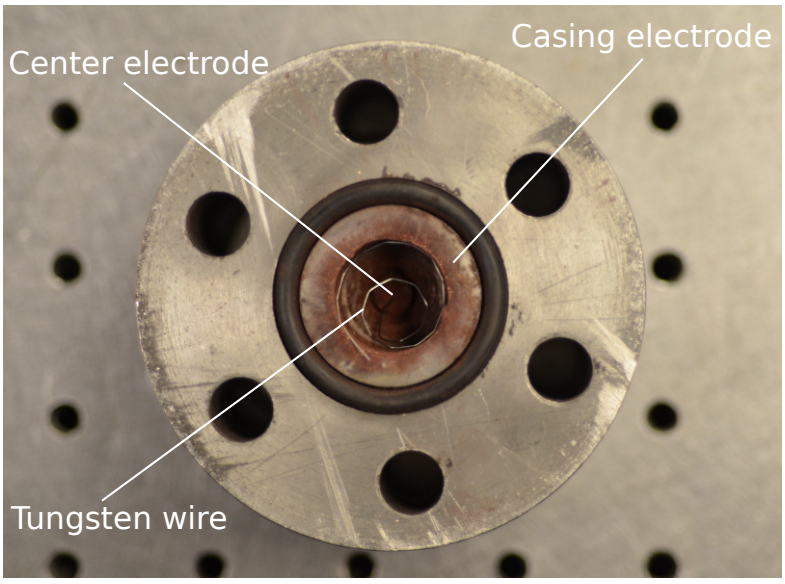

Figure 3.4: Experimental setup for the pressure cell in constant-volume pressure measurements.

where y is the output signal and x is the input signal. To obtain the pressurization rate, a forward-difference scheme was implemented on the filtered pressure data. This pressurization rate was then further refined using a smoothing factor of 0.5. The results of the filtering process are shown in Fig. 3.5. The unfiltered pressure and pressurization curves

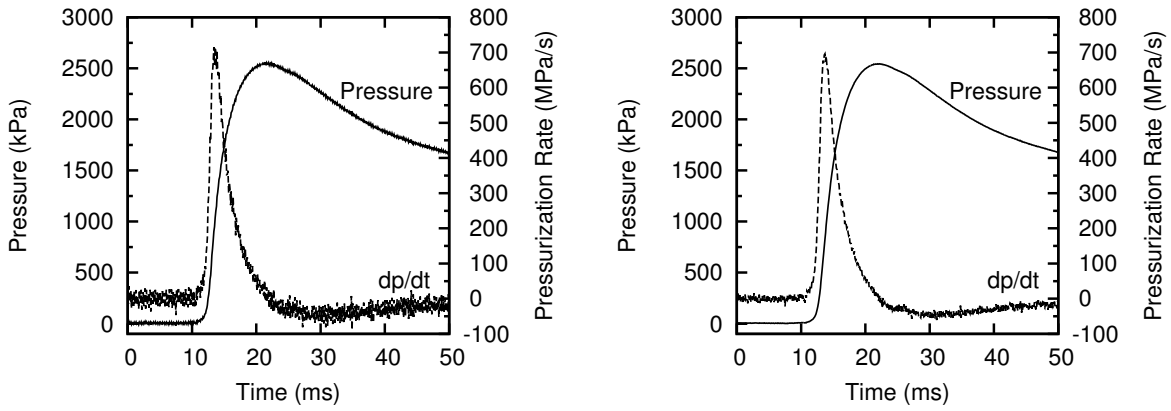

(a) Unfiltered **(b)** Filtered

Figure 3.5: Results of the filtering process on the pressure and pressurization rate of a constant-volume reaction (Table B.1, No. 9).

are shown in Fig. 3.5a, while filtered curves are shown in Fig. 3.5b. The filtering process was used to acquire accurate measurements of the peak pressure and peak pressurization rates to be withdrawn from the data. Details of the implemented script are shown in Appendix F.3.

3.4 Underwater measurements

Underwater experiments were conducted in the 1.06-L-combustion vessel discussed in Section 2.3.2. Samples consisted of miniature light bulbs filled with the reactive mixture. In this investigation two light bulb types were used: cylindrical and nearly-spherical light bulbs as shown in Fig. 3.6a and 3.6b, respectively. Figure 3.6a shows the cylindrical bulb while Fig. 3.6b shows the nearly spherical bulb. The bulbs had approximate volumes of 0.20 ± 6% and 0.10 ± 5% mL, respectively, measured using an equivalent volume of water.

Prepared mixtures were loaded into the light bulbs via a 1-2 mm diameter hole cut into the side of the glass. Holes were cut using a diamond-tip dremel tool. Powders were then carefully loaded into the light bulb by addition and agitation until completely filled. The mass of powder added to the bulbs was measured using a digital scale. In all cases, the relative density of the sample was 23.0 ± 5.1% TMD. Once filled, the hole was sealed using 30-minute epoxy and cured for 24 hours. A filled sample is shown in Fig. 3.7a.

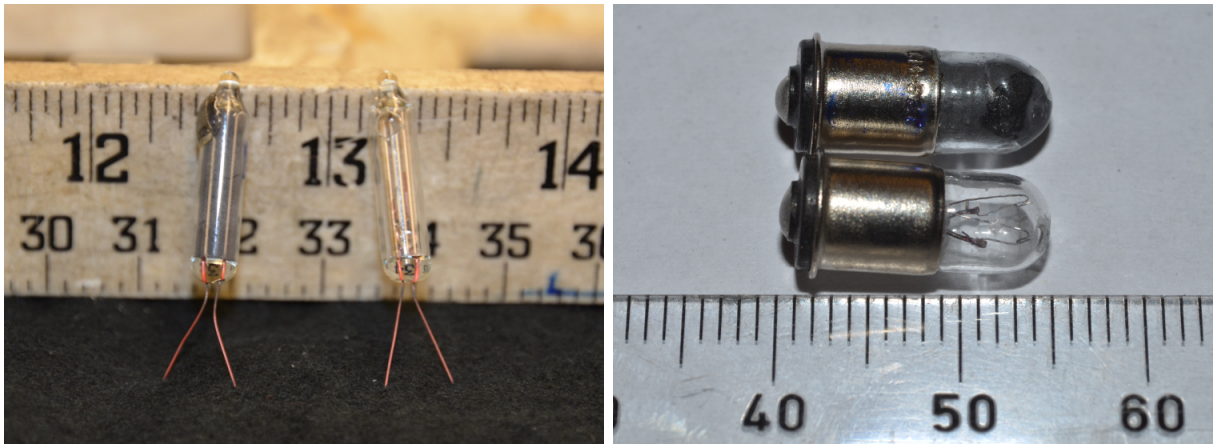

(a) Cylindrical **(b)** Nearly spherical

Figure 3.6: Types of light bulbs used in the preparation of samples for underwater pressure measurements.

Samples were then loaded onto the igniter plug using a custom-designed holder, which connects the sample to the two electrodes of the spark plug (Fig. 3.7b). The igniter plug was then inserted into the water-filled combustion vessel. In all experiments, the free-field pressure transducer was located approximately 35 mm away from the charge.

Upon completion of one experiment, the sample was removed from the igniter plug and the water was removed from the combustion vessel. The water was then flushed three times to sufficiently remove combustion products from within the vessel. Once completely evacuated, the next sample was loaded into the vessel.

The data sampling rate for the experiments varied from 50 to 500 kHz. The exposure time of the high-speed camera was set to 0.46-0.468 μs with a capture speed of 100,000 fps. A resolution of 256 $\times$ 256 was used in all experiments to maximize the number of frames that could be captured. The aperture of the lens was set to $f/2.8$ with an infinite (∞) focal length necessary for Schlieren systems owing to the presence of parallel light. The zoom was set such that the internal cavity of the apparatus filled the entire frame at the set resolution.

To analyze the pressure data, a Python-based script was created to calculate relevant information and store it in data files. In particular the peak pressure of the leading wave, the maximum pressure of the pressure signal and the overall impulse were calculated. In all cases, the values were extracted from data obtained from the free-field sensor.

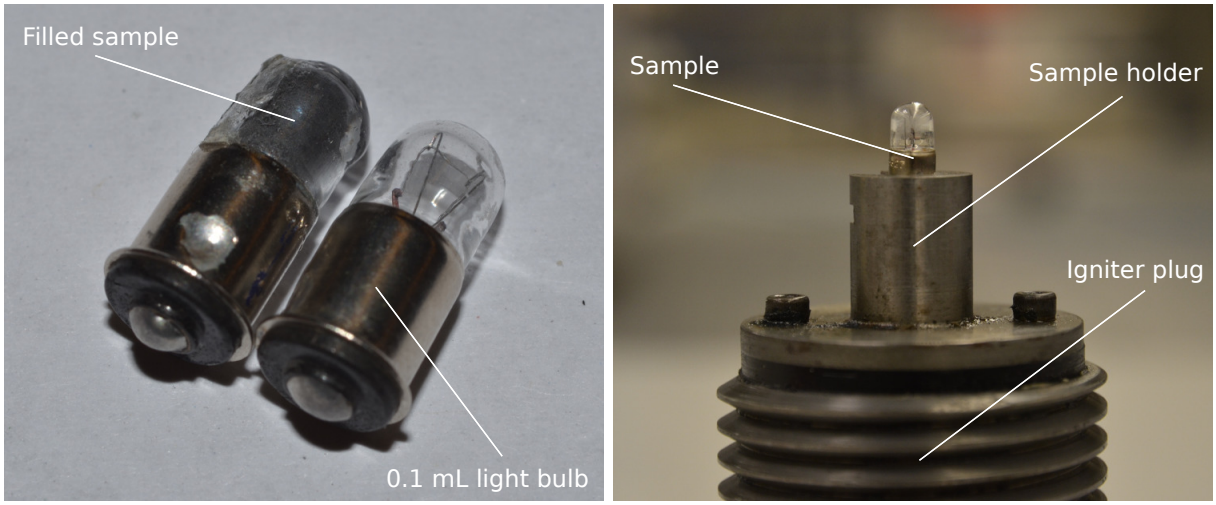

(a) **(b)**

Figure 3.7: Photographs of the (a) prepared samples and (b) sample holder used in underwater pressure measurements.

Impulses were calculated based on Equation (3.2) and evaluated from the initial pressure rise to the time at which the pressure signal dropped below a specific value. This value was selected based on experimental data and is described in Section 4.4.

$$I = \int p dt \tag{3.2}$$

Numerical integration for the impulse was achieved using a trapezoidal scheme given by Equation (3.3). Details of the implemented script are shown in Appendix F.4.

$$\int_a^b f(x)dx \approx (b-a)\left[\frac{f(a)+f(b)}{2}\right] \tag{3.3}$$

Once captured, the frames were extracted from the high-speed videos using FFmpeg and analysed using ImageJ. Linear regressions of the distance-time data for the acoustic wave and the high-pressure gas bubble provided estimates of the acoustic wave speed and volumetric expansion of the gas. Details of the conducted measurements and their results are shown in Table C.1 and C.2.

Chapter 4

Results

4.1 Material preparation and mechanical alloying

The synthesized stoichiometric mixture of Al and CuO is shown in Fig. 4.1. Aluminium particles are shown in dark grey while copper(II)-oxide particles are shown in light grey. The prepared mixture has particle sizes between 1-32 μm, resulting from the powders used in its production. TMD for the mixture was calculated via Equation (4.1) to be 5061.9 kg/m^3. Particle distributions were inspected by SEM to ensure that proper mixing was achieved for the prepared mixture.

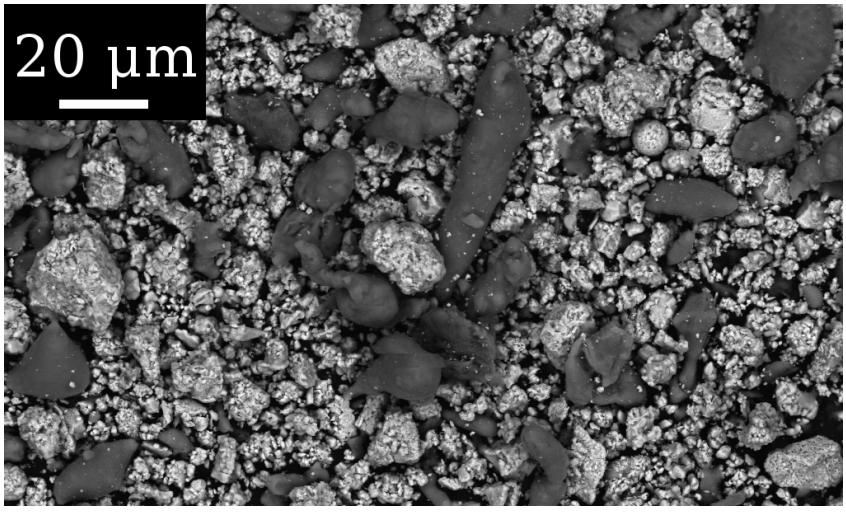

Figure 4.1: SEM photograph of the unmilled mixture depicting the size, morphology and distribution of Al (dark grey) and CuO (light grey).

$$TMD = \frac{\rho_{Al}\rho_{CuO}}{Y_{Al}\rho_{CuO} + Y_{CuO}\rho_{Al}} \tag{4.1}$$

To evaluate the mechanically alloyed mixtures, the SEM permit for monitoring the small-scale structures obtained at each of the different milling times. The overall particle distribution for the samples prepared via mechanical alloying are shown in Fig. 4.2. Figures 4.2a to 4.2d correspond to samples 1 through 4 from Table 3.2. A magnification of 2500 times was used in each of the photographs.

Results indicate that there is a general trend toward reductions in the overall grain size with increased milling time. Samples corresponding to 16 minutes of refinement were found to have particle sizes on the order of 1-10 μm as shown in Fig. 4.2a. Particles

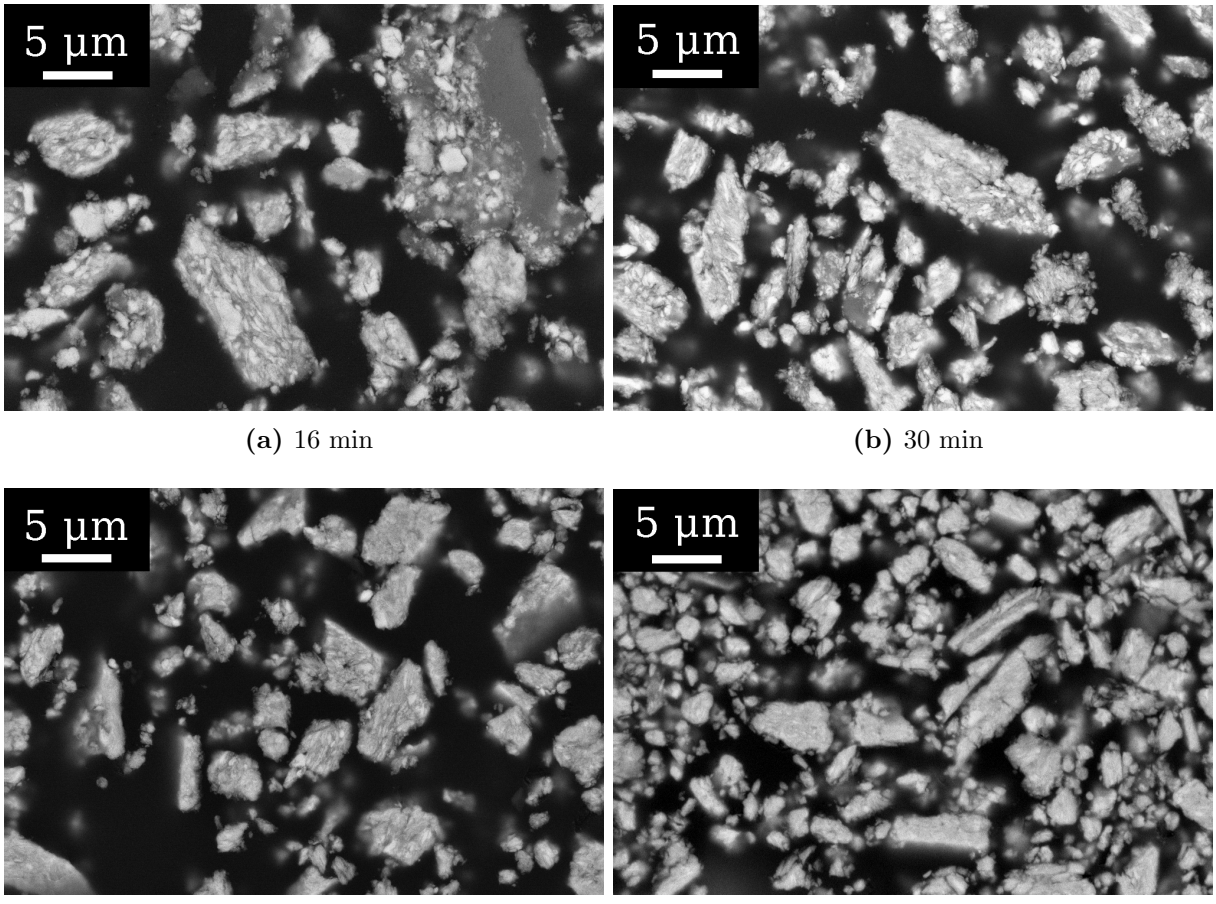

(a) 16 min **(b)** 30 min

(c) 46 min **(d)** 60 min

Figure 4.2: SEM photographs of the mechanically alloyed mixtures illustrating the size and distribution of particles.

corresponding to 60 minutes of refinement (Fig. 4.2d) were found to have averaged particle sizes on the order of 1-2 μm or less. In addition to reductions in the particle sizes, small-scale structures were also found to be reduced with increased milling times. To evaluate this effect, Fig. 4.3 shows the small-scale structures of Al and CuO within the individual grains of the mechanically alloyed mixtures. A magnification of 8500 times was used in each of these photographs. In all cases, CuO particles were found to retain

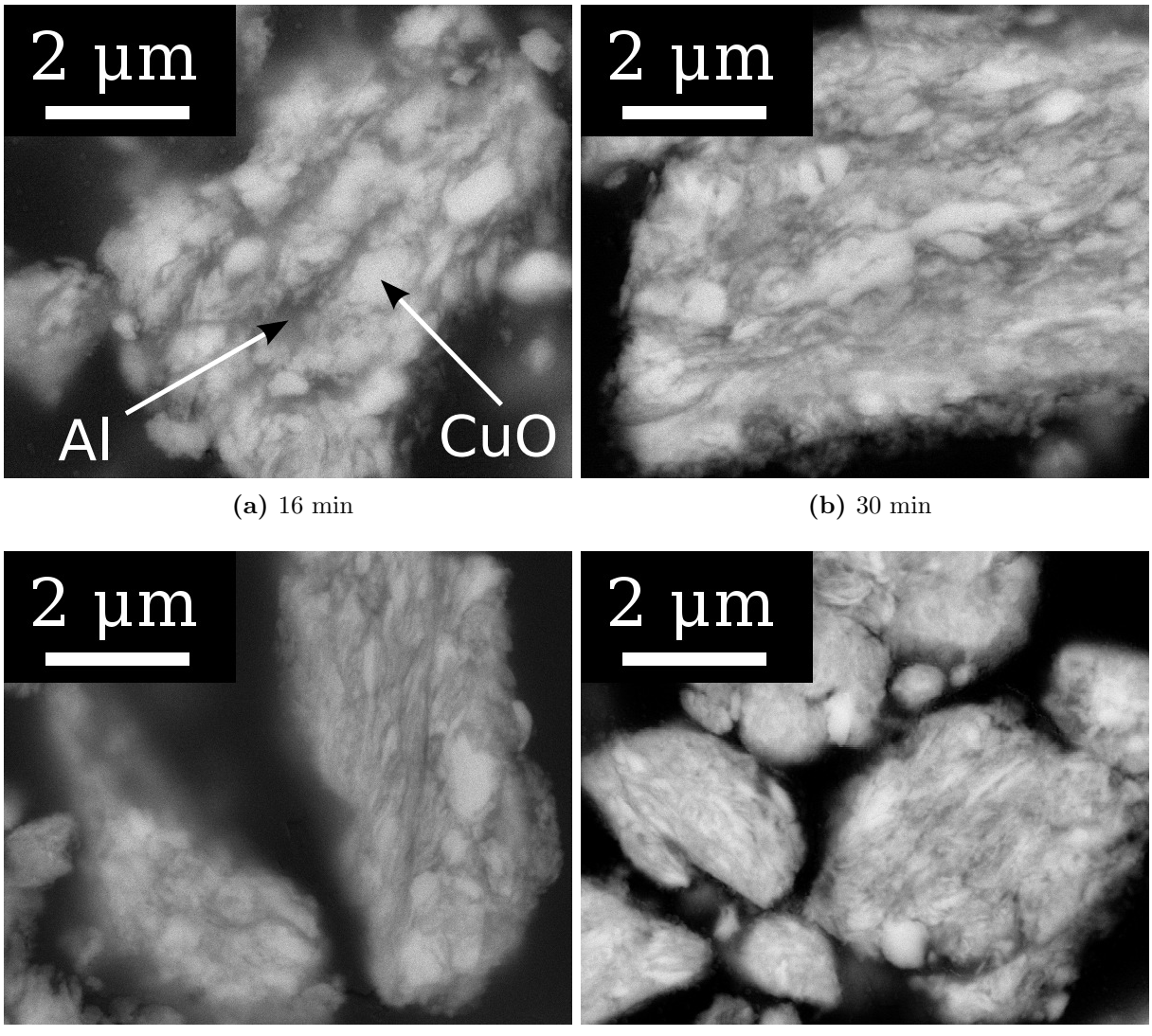

(a) 16 min **(b)** 30 min

(c) 46 min **(d)** 60 min

Figure 4.3: SEM photographs of the mechanically alloyed mixtures illustrating the small-scale structures of Al (dark grey) and CuO (light grey) within the particles.

their shape compared with Al owing to their higher yield strength. This results in each particle consisting of CuO particles embedded in an Al-matrix.

After 16 minutes of refinement (Fig. 4.3a), a well-mixed structure of both constituents is obtained with layers on the sub-micron scale. In general, layers have widths on the order of a few hundred nanometers with the boundaries of each layer being well-defined. Milling for a duration of 30 minutes produced a reduction in the size of these sublayers, as shown in Fig. 4.3b. Again, the boundaries between the layers are fairly well-defined, with layers of both constituents visible. Further refining for 46 minutes (Fig. 4.3c), the layers of Al and CuO become less distinguishable in some regions indicating the possibility of new phases being present in the mixture. Finally, after 60 minutes of milling, the layers of Al and CuO were found to be nearly indistinguishable as shown in Fig. 4.3d.

To further characterize the material, X-ray diffraction (XRD) patterns were obtained for each of the prepared samples. This analysis was used to identify phases within the mixtures to determine whether any reactions had occurred during mechanical alloying. While pressure and temperature traces obtained during the milling process were able

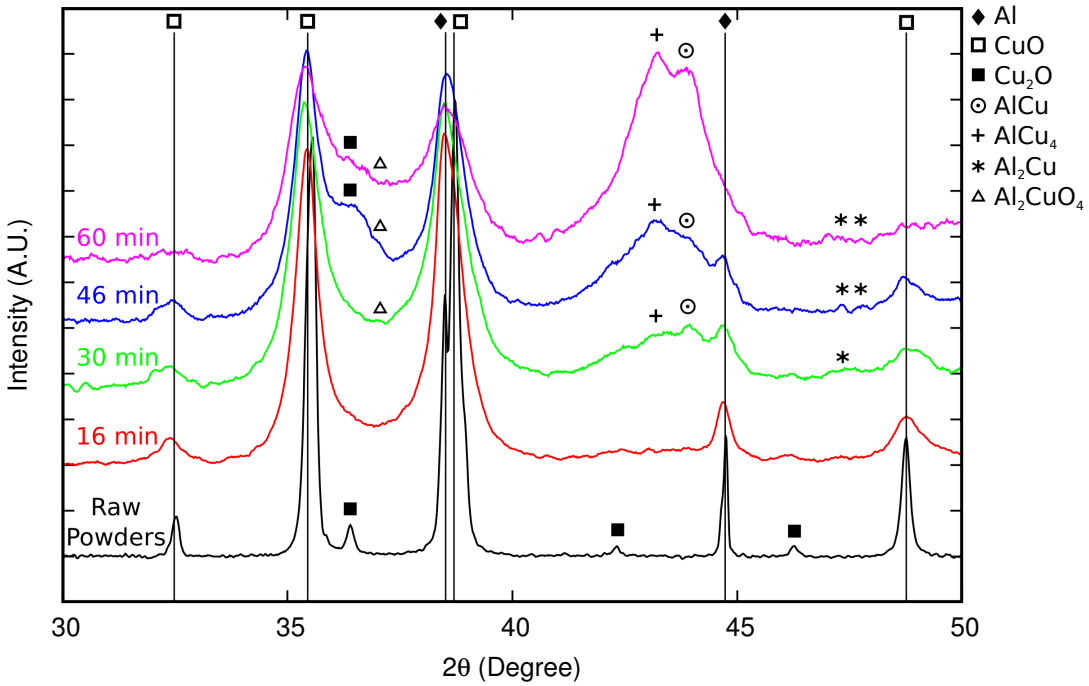

Figure 4.4: XRD patterns of mechanically alloyed samples compared with the unmilled mixture. Al and CuO phases are indicated by vertical lines, all other peaks correspond to intermediate and product phases.

to capture the thermodynamic properties of the bulk sample, they do not capture local reaction events. Instead, XRD patterns were used to identify reactions that may have occurred locally within the sample during refinement. Patterns for each sample are shown in Fig. 4.4 where phases corresponding to relevant peaks are shown in the legend. The unmilled raw powders are found to have peaks corresponding to Al, CuO and a small quantity of Cu_2O. The XRD pattern for the unmilled mixtures served as a comparison for the alloyed mixtures.

After 16 minutes of milling, the composition of the mixture was found to be nearly identical to that of the unmilled powder. Minor broadening of the reactant peaks was apparent, which can be an attributed to local reactions within the mixture that form intermediate and product species or grain refinement. By 30 minutes of milling, peaks corresponding to Al_2Cu, Al_2CuO_4, AlCu and elemental Cu were found. These species correspond to intermediate and product species from the thermite reaction between Al and CuO. Broadening of the peaks further increased, likely owing to the formation of these new phases. After 46 minutes of refinement, the concentration of intermediates and products was found to further increase. Cu_2O re-appeared in the mixture owing to increasing concentrations, which may have been previously masked by the peak broadening at earlier times. Finally, after 60 minutes of alloying these peaks become comparable with those of the initial powders suggesting the formation of substantial amounts of the intermediate species.

As a result of both SEM and XRD analyses, it was shown that increased milling times

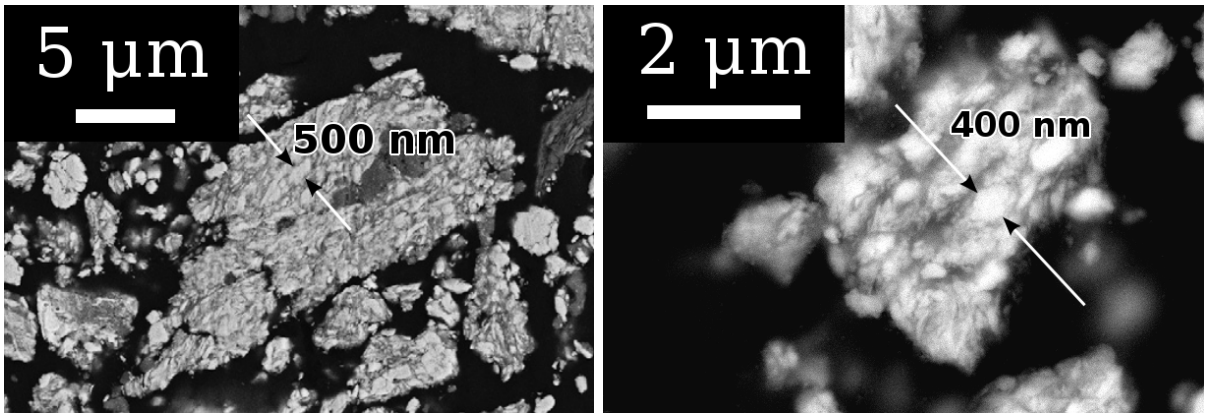

(a) **(b)**

Figure 4.5: Comparison of the small-scale layers between (a) Umbrajkar *et al.* (2006*b*) and (b) the current investigation.

coincide with reductions in the macroscopic scale of the grains as well as the dimensions of the nano-scale layers. Furthermore, alloying for a duration of 30 minutes or more produced significant amounts of intermediate and product phases. It was thus determined that mixtures refined for 16 minutes consisted of well-mixed nano-scale layers of the raw materials with a composition similar to that of the unmilled mixture. While some of the large-scale grains within the 16 minute mixture consist of mostly one constituent, the majority of the particles were found to be well-mixed nano-scale layers of Al and CuO. This result was similarly found by Umbrajkar *et al.* (2006*b*).

A qualitative comparison between the mixture prepared by Umbrajkar *et al.* (2006*b*) and the 16-minute mixture prepared in this investigation is shown in Fig. 4.5. A measurement of the approximate layer thickness of the CuO inclusions within each of the agglomerated particles is shown. In both cases, individual grains had particle sizes on the order of a 1-10 μm with sub-layers of Al and CuO on the order of a few hundred nanometers. Furthermore, both mixtures were found to have well-defined boundaries between the Al and CuO layers and consisted of CuO particles embedded within an Al-matrix. The good agreement between results obtained in the current investigation and those from Umbrajkar *et al.* (2006*b*) indicate that the parameters used in the synthesis of sample 1 (Table 3.2) were effective in producing a desirable mixture.

4.2 Flame propagation speed measurements

Figure 4.6 shows a comparison the reaction event for the unmilled mixture and a mixture prepared via mechanical alloying. Sequential frames captured from the high-speed camera allowed for observations on the behaviour of the flame front for both mixtures. The steady flame produced by the reaction of unmilled mixtures is shown in Fig. 4.6a to 4.6f. The flame is shown propagating from right to left with a well-defined leading edge. The flame was found to propagate at a relatively low constant speed until reaching the end of the channel. In contrast, the flame front produced by the mixture refined for 16 minutes is shown in Fig. 4.6g to 4.6l propagating from right to left at a much higher velocity. Interestingly, these mixtures exhibit a noticeable V-shaped flame front. While it has been previously shown that the convection-driven flame propagation inherent in loosely-packed thermite materials is fastest for higher porosities (Bacciochini *et al.*, 2013), this flame front profile is likely attributed to the increased porosity at the powder-wall interface typical for packed beds (McWhirter *et al.*, 1997). By analysis of the sequential frames obtained from the high-speed camera, a linear regression of the position-time plot

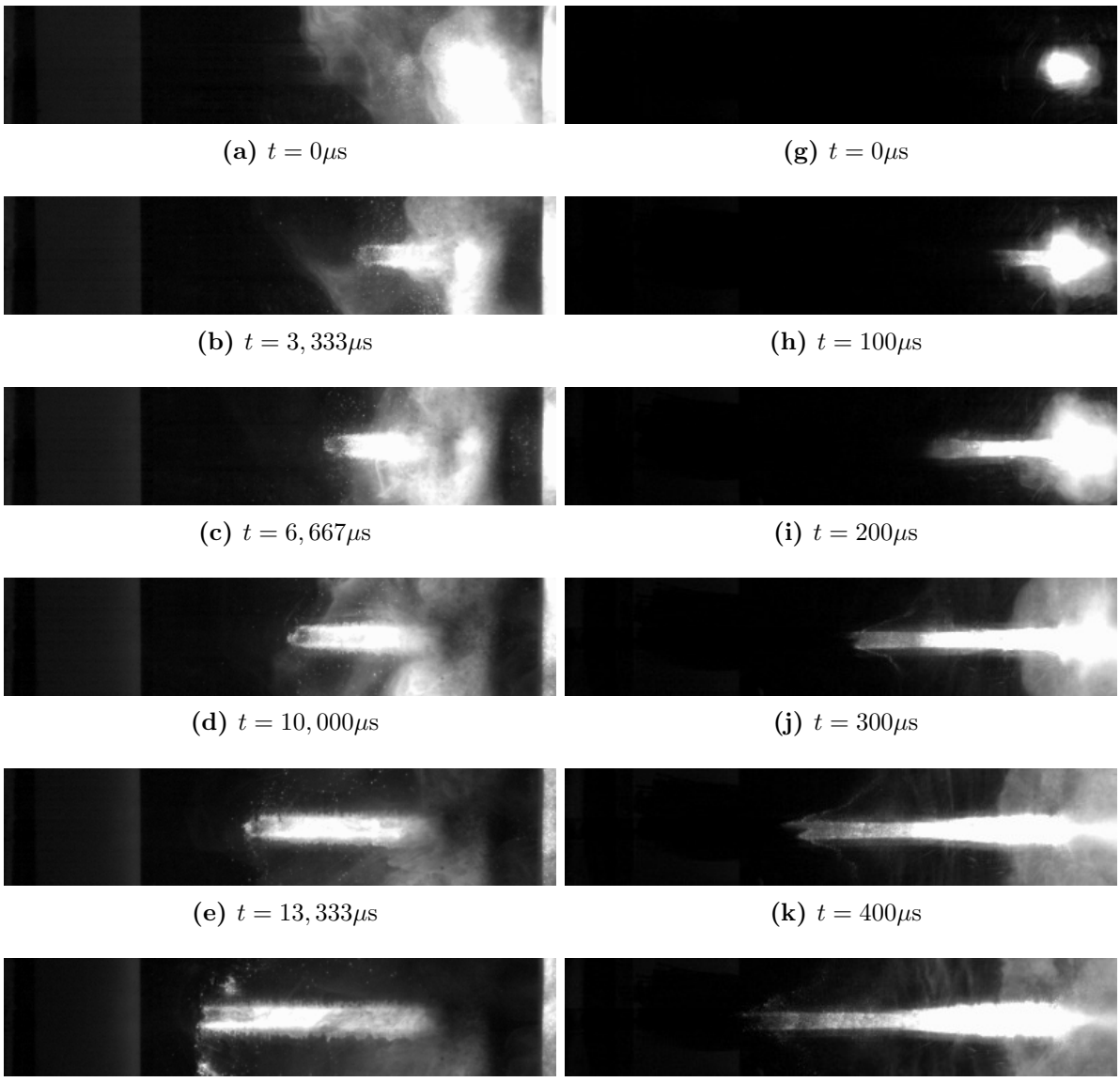

(a) $t = 0\mu$s **(g)** $t = 0\mu$s

(b) $t = 3,333\mu$s **(h)** $t = 100\mu$s

(c) $t = 6,667\mu$s **(i)** $t = 200\mu$s

(d) $t = 10,000\mu$s **(j)** $t = 300\mu$s

(e) $t = 13,333\mu$s **(k)** $t = 400\mu$s

(f) $t = 16,667\mu$s **(l)** $t = 500\mu$s

Figure 4.6: Reconstruction of typical flame propagation speed experiments for (a-f) unmilled and (g-l) mechanically alloyed (16 min) samples illustrating the evolution of the frame-front as a function of time (Table A.1, No. 18 and No. 11).

allowed for estimations of the flame propagation speed. The position-time graph for a typical experiment is shown in Fig. 4.7a. In this graph, it is shown that the flame propagates at a nearly constant rate and can be well-represented by a linear trend. For the presented case (Table A.1, No. 18), the flame was found to propagate at a speed of 2.29 m/s. Results for each experiment is presented in Table A.1. Averaged results for each of the prepared samples is provided in Fig. 4.7b and summarized in Table 4.1.

Results indicate that the mechanically alloyed sample corresponding to 16 minutes of refinement produced the highest flame propagation speeds. In fact, at a relative density of $26.4 \pm 1.9\%$ TMD a flame propagation speed of approximately 72 ± 27 m/s was observed for this mixture while unmilled mixtures resulted in a flame propagation speed of only 1.5 $\pm$ 1 m/s at a relative density of $28.2 \pm 3.5\%$ TMD. Furthermore, all mechanically alloyed mixtures were found to have higher flame propagation speeds compared with the unmilled mixture, however, a loss in the overall reactivity was observed for increased milling times beyond 16 minutes. This finding comes as a result of the higher concentration of reaction products in the mixture observed in the XRD patterns. Thus, it can be concluded that the mixture refined for 16 minutes produced both a desirable nano-structure as well as the highest flame propagation speed. For this reason, this mixture served as the basis for further comparisons.

As a comparison, Sullivan *et al.* (2010) reported on the combustion wave speeds for

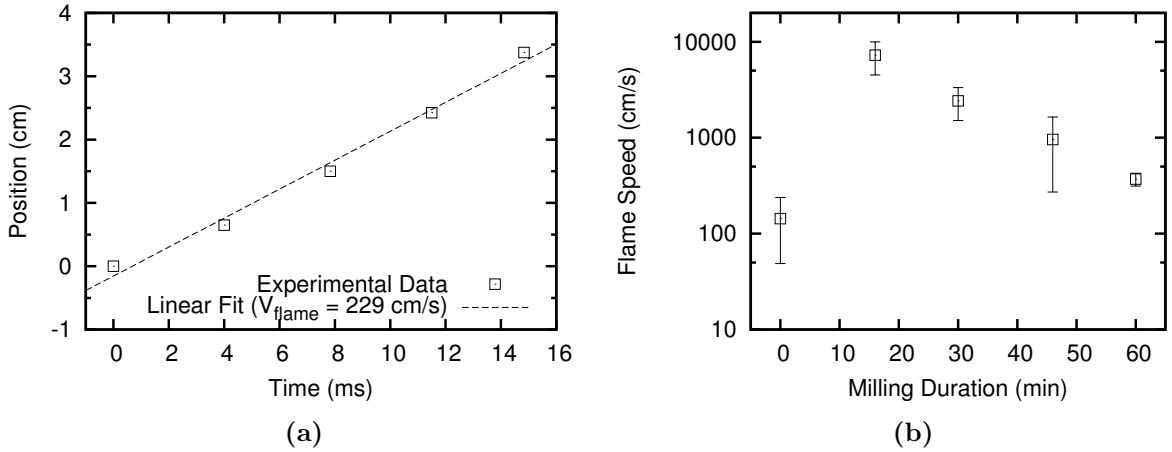

Figure 4.7: (a) Representative position versus time graph used in the estimation of the flame propagation speed (Table A.1, No. 18) and (b) average flame speeds for each of the prepared samples.

Table 4.1: Results of the open-channel flame speed measurements.

Property	Unmilled	Milling Time			
		16 min	30 min	46 min	60 min
Average Relative Density (% TMD)	28.2	26.4	23.3	22.4	18.4
Standard Deviation (% TMD)	3.5	1.9	3.6	4.4	0.8
Average Flame Speed, V_{flame} (cm/s)	144	7240	2420	960	370
Standard Deviation (cm/s)	95	2730	910	690	55

a conventional nano-scale Al-CuO thermite mixture in an open confinement. In their investigation, flame propagation speeds were determined for loosely packed quantities of material. For Al and CuO particle sizes of 80 nm and 45 nm, respectively, a flame propagation speed of approximately 340 m/s was measured. In another investigation by Apperson *et al.* (2007), the flame propagation speed for an Al-CuO mixtures consisting of CuO nanorods with spherical Al nanoparticles was measured. In their investigation, flame propagation speeds were determined using a cylindrical Lexan tube mounted with photodiodes and closed at one end. At a relative density of approximately 17% TMD, this mixture produced flame propagation speeds of nearly 600 m/s. This higher velocity compared with results by Sullivan *et al.* (2010) are likely attributed to the confinement of the tube, which strengthens the front-facing convection.

As a result, the present study thus demonstrate that mixtures prepared via mechanical alloying can successfully attain flame propagation speeds comparable to conventional nano-scale thermites. While the mechanism governing the reaction of these fully-dense mechanically alloyed samples may differ from those of conventional nano-scale thermites (Ermoline *et al.*, 2011, 2012), results indicate that similar reaction rates are present for the conditions investigated in this work.

4.3 Constant-volume pressure measurements

To further evaluate the difference in the combustion behaviours between the mechanically alloyed and micron-scale, unmilled mixture, pressure measurements were conducted in a constant-volume pressure cell. In order to identify the important combustion characteristics of the materials, relevant properties of the pressure signal were extracted for evaluation. These properties are shown schematically in Fig. 4.8. In all experiments, pressure increases rapidly, attains a maximum and slowly decreases with time. Since

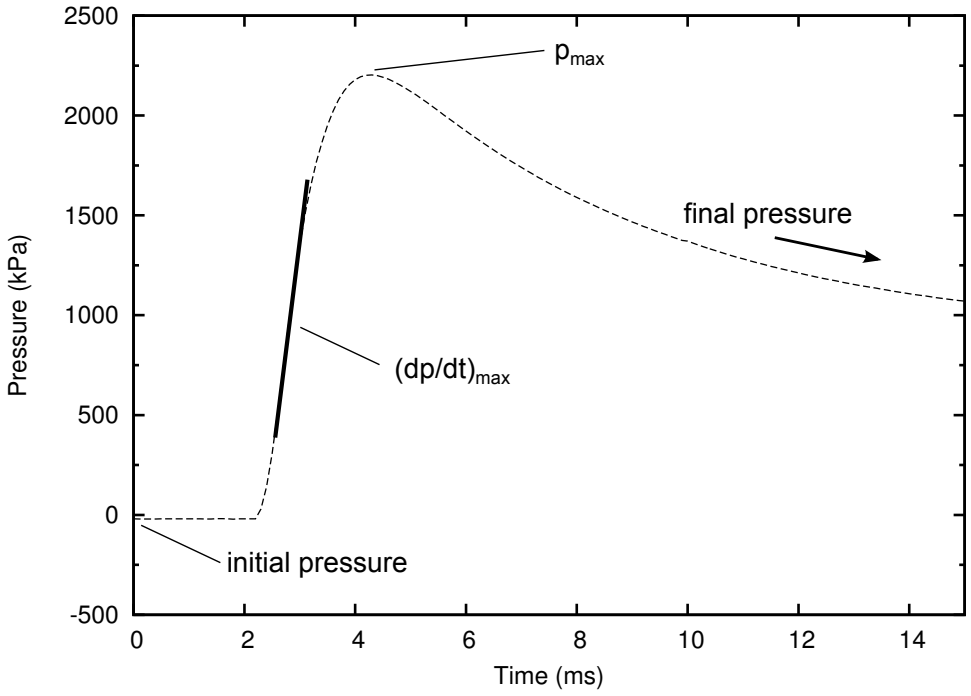

Figure 4.8: Relevant properties of a pressure signal produced in a constant-volume combustion experiment (Table B.1, No. 21).

the rate at which pressure decays is a function of the sensor itself, heat losses and condensation of product gases, the energetic reaction is considered to be complete once the pressure attains a maximum value. The two main parameters that were evaluated in the present study were the peak pressure, p_{max}, and the peak pressurization rate, $(dp/dt)_{max}$.

A comparison of the pressure-time histories obtained for the unmilled and milled samples are provided in Fig. 4.9 and 4.10, respectively. In each figure, pressure traces for four experiments are illustrated as a function of the relative density.

By inspection of these figures, it is found that the unmilled mixtures produce rise times on the order of 10 ms compare to less than 1 ms for the mechanically alloyed mixtures. This comes as a result of the significantly higher flame propagation speed inherent in the mechanically alloyed sample. In terms of relative densities, higher loads resulted in higher pressures in both mixtures. This occurs owing to the higher energy densities within the pressure cell for increased loadings. To further analyze this behaviour, the peak pressures as a function of the relative density were obtained.

Figure 4.11 shows the trend for increasing pressure as a function of relative density, reported as a percentage of TMD. Over a range from 0.5 to 5.5% TMD, a linear trend

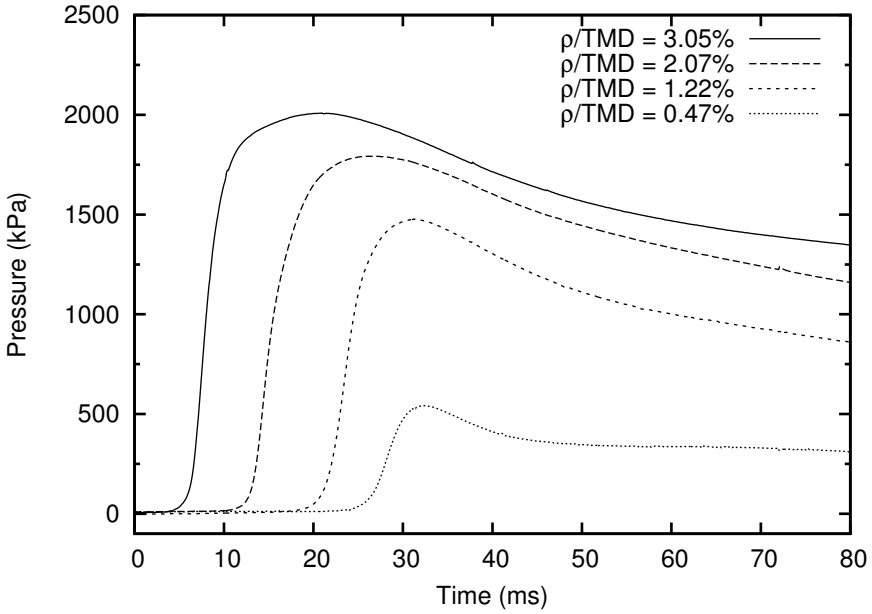

Figure 4.9: Comparison of the pressure profiles produced by unmilled 2Al-3CuO for decreasing relative density.

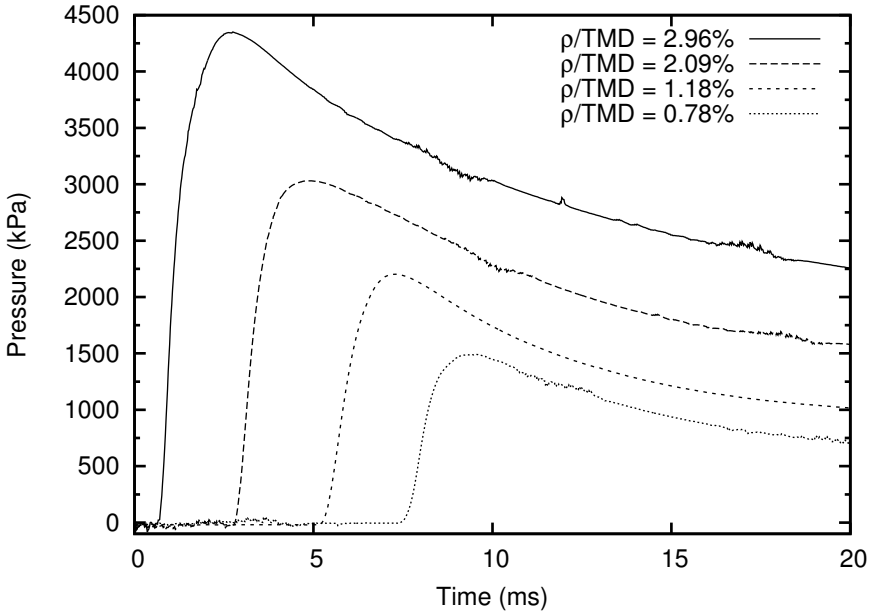

Figure 4.10: Comparison of the pressure profiles produced by mechanically alloyed 2Al-3CuO for decreasing relative density.

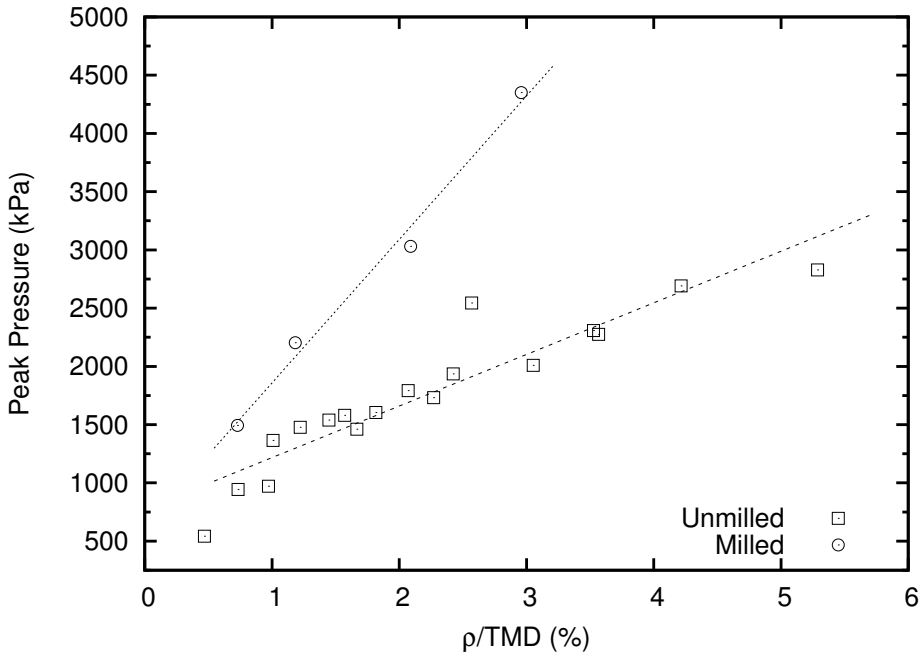

Figure 4.11: Peak pressures (p_{max}) for unmilled (⊡) and mechanically milled (⊙) 2Al-3CuO in a closed vessel as a function of the relative loading density (ρ/TMD).

in the peak pressure was observed for both mixtures. Peak pressures for the samples prepared via mechanical alloying were consistently higher than those for the unmilled mixture. In all cases, the peak pressure was approximately two times higher.

To quantify the difference in pressurization rates between the two mixtures, the extracted pressurization rates are shown as a function of the relative density in Fig. 4.12. Results indicate that the milled samples yield peak pressurization rates upwards of 10 times higher than those obtained by the unmilled mixture. This significantly higher rate is a result of both faster flame propagation speeds and the higher peak pressures. Similar to the trends in peak pressure, peak pressurization rates were found to be accurately represented by linear regressions over the range evaluated in this work. Interestingly, while reaction rates were found to be increased by approximately two orders of magnitude in terms of flame propagation speeds (Section 4.2), peak pressurization rates in a constant-volume reaction were found to increase by only one order of magnitude.

As a comparison, Sullivan *et al.* (2010) evaluated the pressurization rates of conventional nano-scale stoichiometric Al-CuO in a constant-volume reaction. In their investigation, 25 mg of powder was added to a 13 mL pressure cell corresponding to approximately 0.05% of TMD. The powder was initiated using resistive heating of a nichrome

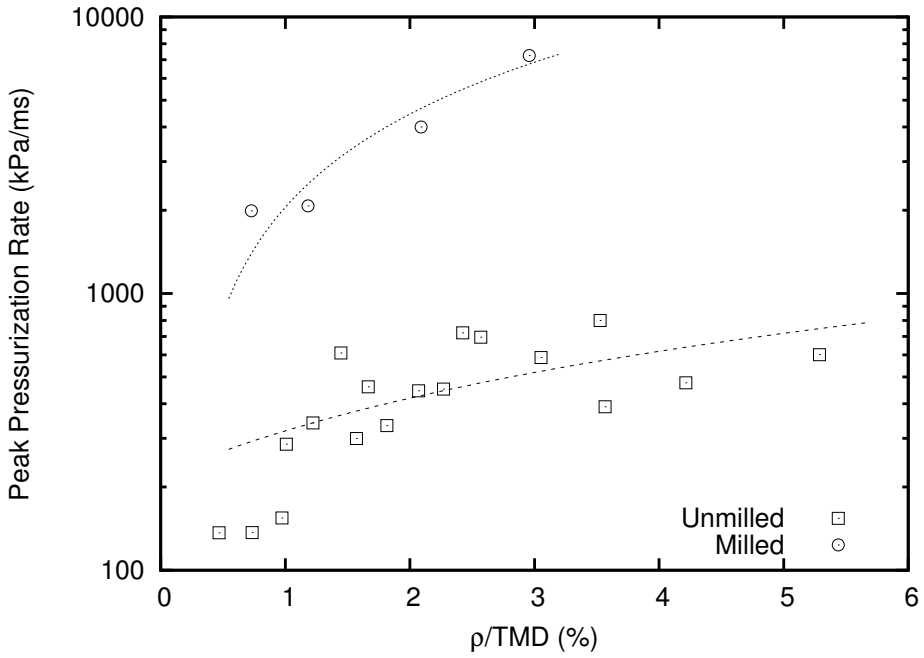

Figure 4.12: Maximum pressurization rates $[(dp/dt)_{max}]$ for unmilled (⊡) and mechanically alloyed (⊙) 2Al-3CuO in a closed vessel as a function of the relative loading density (ρ/TMD).

filament. It was determined that a maximum pressurization rate of approximately 62,000 kPa/ms was achieved. While the materials prepared in the current investigation show a significant improvement in the pressurization rate compared with micron-scale powders, these pressurization rates are found to be approximately one order of magnitude smaller than those produced by conventional nano-scale mixtures. This result is likely attributed to the slower flame propagation speed obtained by mechanically alloyed mixtures compared with conventional nano-scale mixtures, which is strongly correlated with the pressurization rate.

4.4 Underwater measurements

Figure 4.13 shows an example of the evolution of the pressure wave generated by the reaction of a thermite capsule in water. Each frame corresponds to a time interval of 10 μs. The first frame shows the moment immediately prior to the reaction of the capsule. In the second frame, a pressure wave formed by the reaction of the thermite mixture is

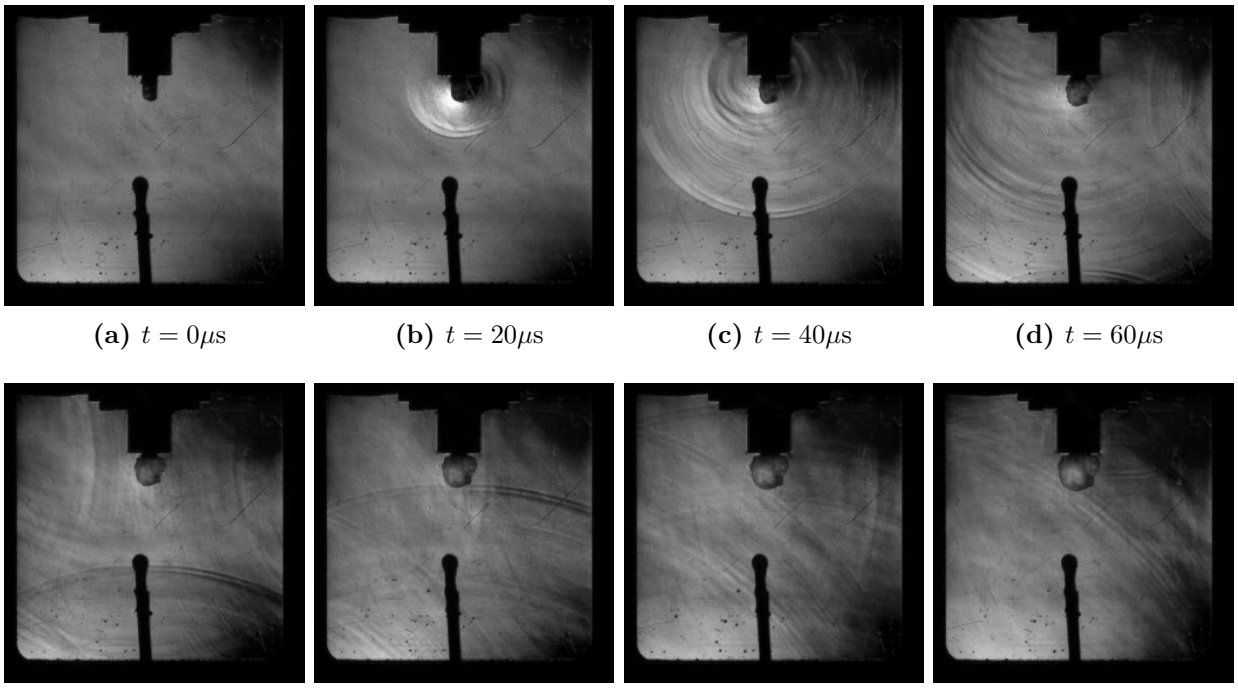

(a) $t = 0\mu$s **(b)** $t = 20\mu$s **(c)** $t = 40\mu$s **(d)** $t = 60\mu$s

(e) $t = 80\mu$s **(f)** $t = 100\mu$s **(g)** $t = 120\mu$s **(h)** $t = 140\mu$s

Figure 4.13: Schlieren photographs depicting the motion of the emitted pressure wave in an underwater reaction of 2Al-3CuO (Table C.2, No. 37).

shown surrounding the charge. Frames 3 through 8 show the propagation of this emitted wave, which travels radially from the center of the charge past the free-field sensor to the surrounding surfaces. The wave then reflects off each of the surrounding surfaces causing a complex wave pattern. Linear regressions of the position-time data for the pressure wave find that the pressure wave travels at approximately 1553 $\pm$ 91 m/s. This value corresponds to a wave traveling at the ambient sound speed in water suggesting that these pressure waves are acoustic waves.

Figure 4.14 shows the evolution of the high-pressure gas bubble resulting from the gaseous products formed by the thermite reaction. Each frame corresponds to a time interval of 100 μs. As a result, the high-pressure gas bubble is found expanding at a slower rate than the leading pressure wave. Again, the first frame shows the moment immediately prior to emitting a pressure wave. The second frame shows the size and location of the high-pressure gas bubble after 100 μs, corresponding to a time after the pressure wave has reflected off the surrounding surfaces. Frames 3 through 8 show the evolution of this gaseous sphere as a function of time in which the gas bubble is

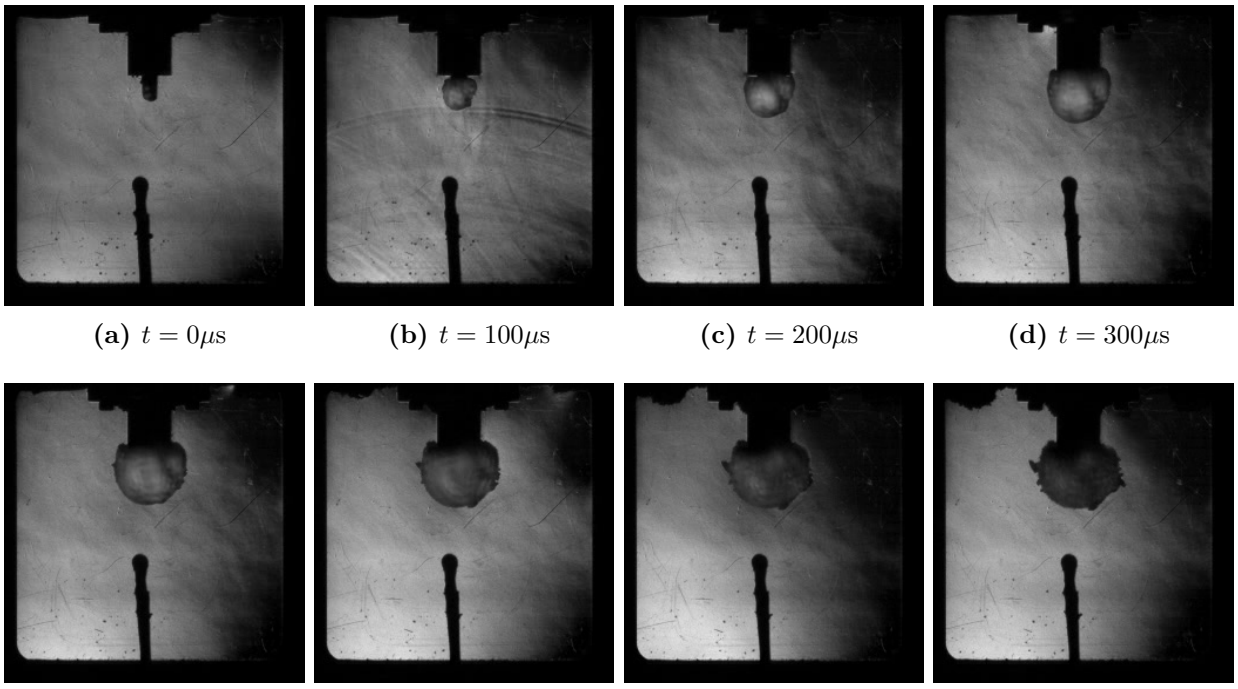

(a) $t = 0\mu$s **(b)** $t = 100\mu$s **(c)** $t = 200\mu$s **(d)** $t = 300\mu$s

(e) $t = 400\mu$s **(f)** $t = 500\mu$s **(g)** $t = 600\mu$s **(h)** $t = 700\mu$s

Figure 4.14: Schlieren photographs depicting the evolution of the high-pressure gas-bubble in an underwater reaction of 2Al-3CuO (Table C.2, No. 37).

shown expanding rapidly at early times. The bubble is then shown reaching its peak volume after approximately 600 μs followed by a contraction in the last frame whereby a small decrease in the bubble's volume is apparent. This contraction has previously been reported for free-field explosions in which the inertia of the outward traveling contact surface causes the product gases to over-expand forming a negative pressure within the gas sphere (Cole, 1948). This negative pressure then causes the sphere to contract, at which point the the contact surface travels inwards. The inertia of the contact surface causes an oscillation in the volume of the gas sphere, which sends pressure waves both outward and inward. Typically, these oscillations are rapidly damped due to viscous effects and only significantly contribute to the pressure for the first few oscillations (Keller & Kolodner, 1956).

Pressure-time signals acquired by the three sensors for a typical experiment are shown in Fig. 4.15. In this graph, $p_{wall,1}$ and $p_{wall,2}$ correspond to the pressure obtained from the wall-mounted sensors at the top and bottom, respectively, while $p_{free-field}$ corresponds to the pressure at the free-field sensor. The obtained signals can be broken into two main

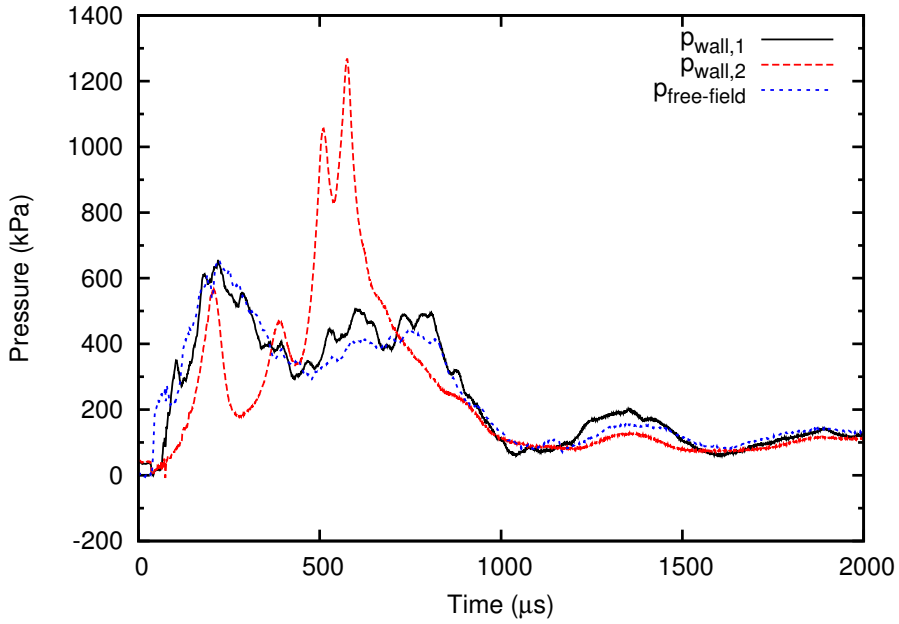

Figure 4.15: Typical form of the pressure signal produced in an underwater pressure experiment for the wall and free-field sensors (Table C.2, No. 36).

components. First, pressure fluctuations from the emitted acoustic waves are captured with reflections from surrounding surfaces, which creates complicated wave patterns. Second, low frequency pressure oscillations are found, likely owing to the oscillating nature of the gas bubble. In Fig. 4.15, the early dynamics of the pressure signal are captured within the first 1000 μs, while the first and second low frequency oscillations are shown occurring at approximately 1300 μs and 1900 μs.

To evaluate and compare the pressure profiles obtained from the reaction of both the unmilled and mechanically alloyed mixtures as well as the results obtained by Apperson *et al.* (2008), three parameters were extracted from the data captured by the free-field sensor. These parameters correspond to the peak pressure obtained from the leading pressure wave (p_{shock}), the maximum pressure recorded by the sensor (p_{max}) and the impulse from the pressure profile (I). Since the pressure recorded by the free-field sensor is affected by decay rate of the sensor at later times, impulses were calculated from the beginning of the pressure rise until the time at which the pressure fell below 50 kPa. This value was selected as it well-represented the time at which the significant portion of the pressure profile ended. These parameters, are identified in Fig. 4.16.

A comparison of the typical pressure profiles obtained for unmilled and mechanically

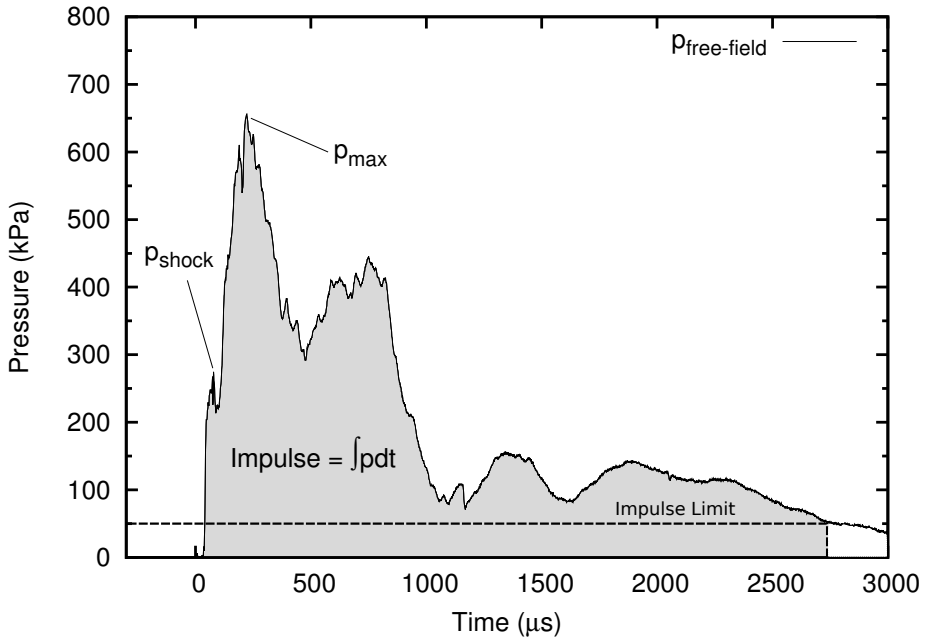

Figure 4.16: Relevant properties from a particular experiment (Table C.2, No. 36).

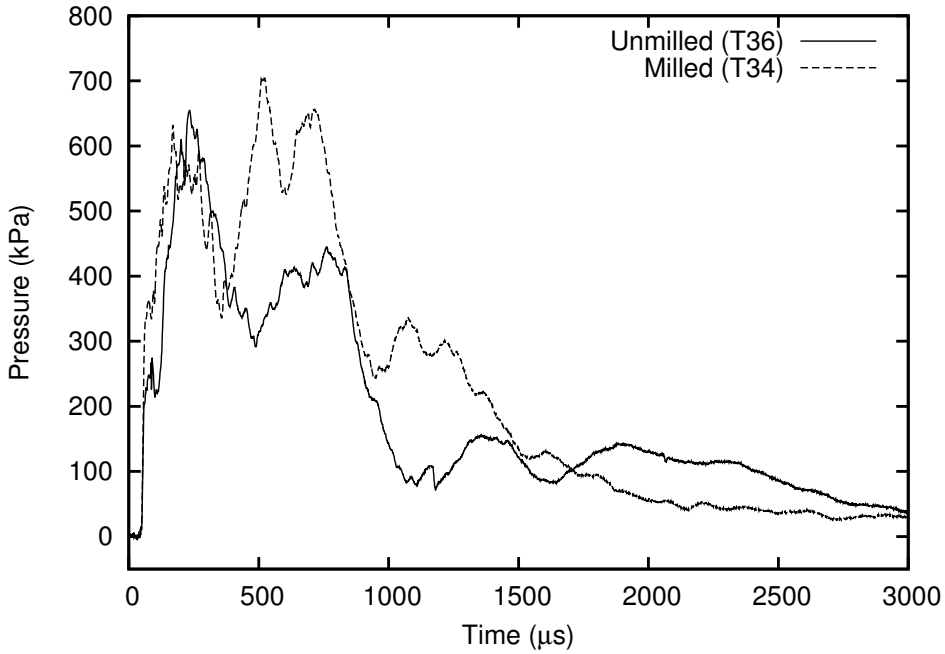

Figure 4.17: Comparison of the pressure profiles produced by mechanically alloyed and unmilled mixtures at the location of the free-field sensor.

alloyed mixtures is shown in Fig. 4.17. Preliminary inspection of these pressure profiles suggest that mixtures prepared via mechanical alloying result in both higher initial pressures and a more pronounced second peak compared to the unmilled mixture. In particular, the profile produced by mechanically alloyed samples are found to rise and drop to near-equilibrium pressures over shorter times. This is likely a property owing to the higher flame propagation speeds, which results in faster exhaustion of the reactant materials.

Figure 4.18 shows the difference in the pressures produced by the leading wave. Results indicate that mixtures produced via mechanical alloying yield higher pressures in the leading wave. More specifically, the micron-scale unmilled mixtures produced initial pressures on average of 270 $\pm$ 96 kPa while alloyed samples produced initial pressures of 450 $\pm$ 220 kPa. This finding suggests that mechanically alloyed samples produce approximately twice the pressure for the leading wave compared with unmilled samples. The likely reason for this observation is the previously observed higher flame propagation speeds, which produce a larger quantity of high pressure gaseous products over the same time-scale. This increased gas production rate likely leads to higher compressions in the surrounding material at earlier times, producing a higher pressurization rate for

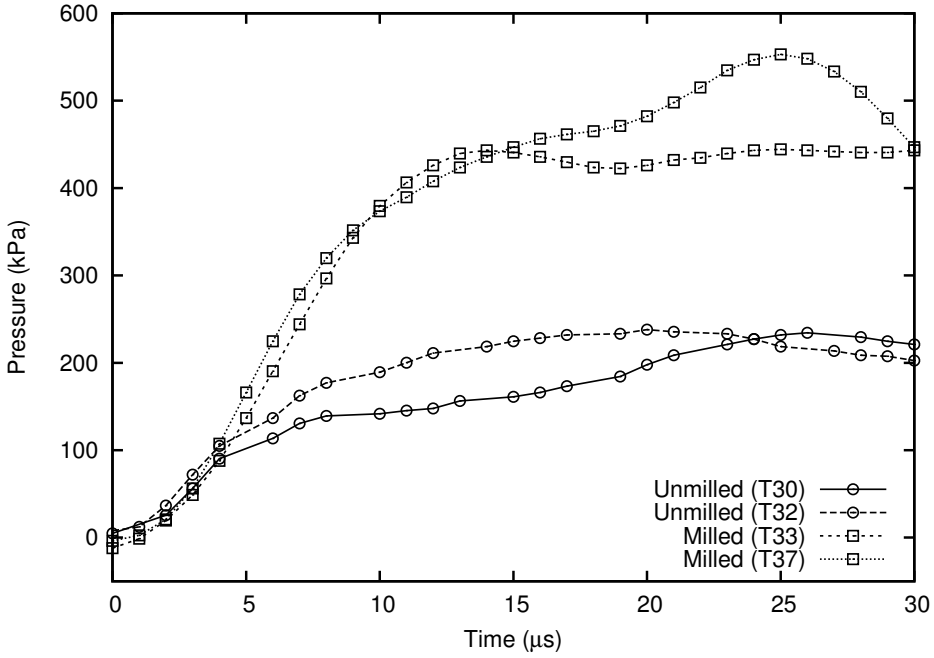

Figure 4.18: Comparison of the pressures induced by the leading wave produced from unmilled and mechanically alloyed mixtures.

the leading wave.

In terms of the maximum pressures for the entire waveform, unmilled samples produced pressures of 880 ± 290 kPa compared to mechanically alloyed samples, which were found to produced peak pressures of 965 ± 265 kPa. This finding suggests that the maximum pressure is not strongly correlated with the increased reaction rates for mechanically alloyed samples. Instead, this property appears to be more directly correlated by the energy density of the charge itself, namely the quantity of mixture used in the sample.

Finally, calculations for the impulse at the location of the shock sensor indicate that the profiles produced by mechanically alloyed mixtures yield smaller impulses. Unmilled and mechanically alloyed mixtures were found to produce impulses of 1.71 ± 1.71 kPa·s and 1.04 ± 0.66 kPa·s, respectively. Again, the likely reason for this observation is the reaction rates inherent in mechanically alloyed mixtures, which causes the reaction event to last for a shorter amount of time. The slower reaction progress for unmilled mixtures is found to extend the duration of the pressure fluctuations, resulting in elevated

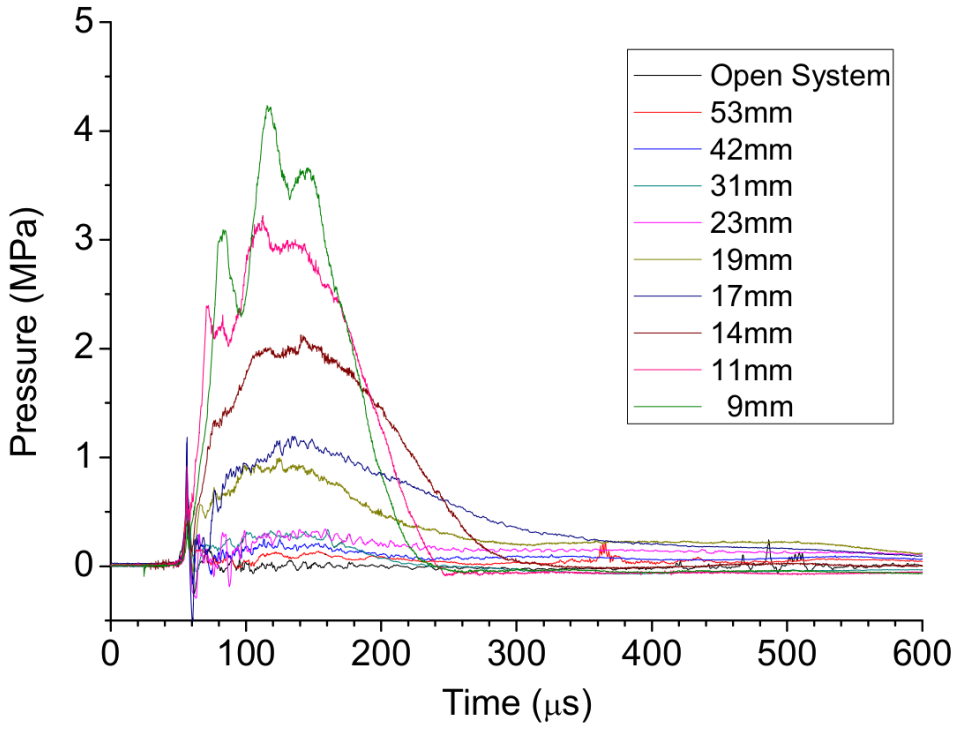

Figure 4.19: Pressure-time histories obtained by Apperson *et al.* (2008) for an Al-Bi_2O_3 thermite.

pressures lasting for longer times. As a result, the impulse, which is the area under the pressure-time curve, for the unmilled mixture is larger.

In the investigation by Apperson *et al.* (2008), the pressure signals obtained by a nano-scale Al-Bi_2O_3 thermite mixture were measured for varying confinement volumes. In their experiments, 3 mg of the thermite mixture was placed in a cylindrical chamber with a volume varied between 0.8 and 27.5 mL. A pressure sensor located 37.5 mm from the charge was used to evaluate the pressure signature produced by the reaction of the thermite mixture. The generated pressure profiles are shown in Fig. 4.19. In general, the pressure signals obtained for small confinement volumes are found to be qualitatively similar to those obtained for the mechanically alloyed mixtures in the present study. In both cases the pressure profile is composed of an early, rapid pressure rise followed by a strong second peak.

Figure 4.20 shows the results obtained by Apperson *et al.* (2008) for the peak pressure of the leading wave, the maximum pressure of the waveform, and the impulse of the waveform as a function of the confinement volume. Results indicated that the pressure obtained by the leading wave was not correlated to the volume of the confinement,

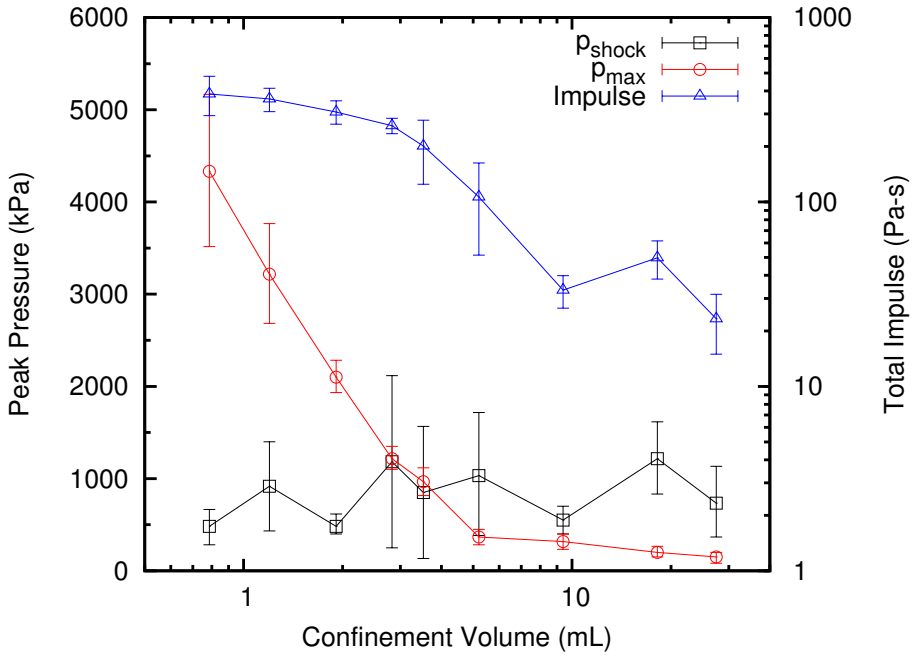

Figure 4.20: Results for the pressures and impulses recorded as a function of the confinement volume for a nano-scale Al-Bi_2O_3 thermite mixture, modified from Apperson *et al.* (2008).

Table 4.2: Comparison of peak pressures and impulses for the unmilled, milled and reference mixtures.

Property	Unmilled	Milled	Apperson *et al.* (2008)
p_{shock} (kPa)	270	450	$\sim$ 500-1000
p_{max} (kPa)	880	965	$\sim$ 4300
Impulse (kPa·s)	1.71	1.04	$\sim$ 0.4

yielding a value consistently within the range of 500-1000 kPa. In contrast, the maximum pressure and impulse generated by the reaction were found to be strongly related to the confinement volume. In both cases, a decreasing trend with increasing volume of the confinement was observed. In particular, values of the maximum pressure and impulse dropped from approximately 4300 to 100 kPa and 400 to 25 Pa·s, respectively. This is likely attributed to the fact that the maximum pressure and impulse are properties for which time scales longer than the acoustic time are important, while the pressure of the leading wave is not. Thus, for smaller volumes one would expect both an increase in the peak pressure and impulse for smaller volumes owing to faster time-scale for equilibration.

For the cellular transfection experiments, Apperson *et al.* (2008) utilized a system corresponding to the smallest confinement volume of 8 mL. As a result, the performance of the mechanically alloyed mixture in the present study for applications in cellular transfection can be evaluated. A comparison of the peak pressures and impulses for all three mixtures is provided in Table 4.2. While the trends for increasing peak pressures and decreasing impulses are observed, the performance of the mechanically alloyed mixture is found to fall short compared with the Al-Bi_2O_3 nano-scale mixture. Most notably, the Al-Bi_2O_3 system was found to produce much higher maximum pressures over a much shorter pulse duration. These differences, however, may likely be attributed to the significantly higher gas production (Fischer & Grubelich, 1996) and reaction rates (Wang *et al.*, 2011) inherent for the Al-Bi_2O_3 mixture compared with Al-CuO.

Chapter 5

Predictions of peak pressures from thermodynamic calculations

Thermodynamic equilibrium calculations can be used to predict the end states of many combustion processes from thermodynamic considerations alone. In particular, assumptions about the combustion processes allow for simplifications of the governing equations, reducing complex equations to a solvable form. In general, thermochemical equilibrium calculations are governed by an *equilibrium criterion*, which dictates the end solution. In the present study it is desirable to predict the peak pressures during the constant-volume reaction observed experimentally. Predictions for the combustion pressures provide the groundwork for future modeling of the combustion processes. This chapter presents a method for predicting these peak pressures from thermochemical equilibrium criteria.

5.1 Formulation of the problem

5.1.1 Simplifications of the combustion processes

Constant volume adiabatic combustion

Consider the reaction of a thermite mixture in a closed and insulated vessel of fixed volume. For an insulated vessel with a fixed volume the heat loss/addition (Q) and work done (W) by the system are both assumed to be zero. Applying these simplifications to the conservation of energy given by,

$$dE = dQ - dW \tag{5.1}$$

one obtains the result that the internal energy (E) is invariant, *i.e.*,

$$E_{reactants} = E_{products} \tag{5.2}$$

For a multi-component system, the internal energy is the summation of all internal energies of the relevant species, *i.e.*,

$$E = \sum_{i=1}^{n} E_i = me = \sum_{i=1}^{n} m_i e_i = N\bar{e} = \sum_{i=1}^{n} N_i \bar{e}_i \tag{5.3}$$

where the i^{th} component's specific and molar internal energy are

$$e_i = e_i^0 + \int_{T^0}^{T} C_{V,i} dT \tag{5.4}$$

$$\bar{e}_i = \bar{e}_i^0 + \int_{T^0}^{T} \bar{c}_{V,i} dT \tag{5.5}$$

In this equation, the reference internal energies ($e_i^0, \bar{e}_i^0$) are evaluated at the reference temperature (T^0), taken as 298.15 K. The substitution of Equation (5.4) and (5.3) into Equation (5.2) results in the balance of internal energies for the system

$$\sum_{i=1}^{n_{reactants}} m_i \left(e_i^0 + \int_{T^0}^{T} C_{V,i} dT \right) = \sum_{i=1}^{n_{products}} m_i \left(e_i^0 + \int_{T^0}^{T} C_{V,i} dT \right) \tag{5.6}$$

This equation is further constrained by the fact that the volume (V) of the confinement is assumed to be constant and closed with no mass transfer ($\dot{m} = 0$), producing the result that the density (ρ) within the vessel is also constant

$$\rho_{reactants} = \rho_{products} \tag{5.7}$$

Constant pressure adiabatic combustion

Another important combustion process is the reaction at constant pressure. Consider a slow flame propagating through a combustible mixture. If this flame propagates at a relatively slow speed compared to the local sound speed, one can assume that the pressure is constant across the flame, *i.e.*,

$$p_{reactants} = p_{products} \tag{5.8}$$

Further assuming that the process is steady state and adiabatic with negligible changes of kinetic energy owing to the slow flame speed, conservation of energy yields an invariance in the enthalpy, *i.e.*,

$$h_{reactants} = h_{products} \tag{5.9}$$

This results in an expression similar to Equation (5.6) for the enthalpy given by

$$\sum_{i=1}^{n_{reactants}} m_i \left(h_i^0 + \int_{T^0}^{T} C_{p,i} dT \right) = \sum_{i=1}^{n_{products}} m_i \left(h_i^0 + \int_{T^0}^{T} C_{p,i} dT \right) \tag{5.10}$$

These two constraints provide the additional conditions required to calculate the equilibrium state.

5.1.2 Equilibrium criterion

In order to determine the state at which the system is in chemical equilibrium, the simplifications above are subject to the equilibrium criterion. The condition for chemical equilibrium corresponds to the the minimization of free energy, typically, the Gibbs free energy defined as

$$G = E + pV - TS \tag{5.11}$$

The minimization of free energy corresponds to a state for which the derivative of the Gibbs free energy is zero, *i.e.*,

$$(dG)_{p,T} = 0 \tag{5.12}$$

or in terms of the individual species

$$\sum_{i=1}^{n} \bar{g}_i dN_i = 0 \tag{5.13}$$

where $\bar{g}$ is the molar Gibbs free energy. Equations (5.6), (5.7) and (5.13) comprise the three necessary constraints from which the equilibrium state and composition can be obtained. These calculations can be performed by hand, however, for systems containing a large quantity of species they become difficult. Instead, numerical tools have been developed to solve the resulting system of non-linear algebraic equations. In the present study, NASA's Chemical Equilibrium with Applications (CEA) package (McBride & Gordon, 2002) has been used to perform these calculations.

5.2 NASA's Chemical Equilibrium with Applications (CEA) package

NASA's Chemical Equilibrium with Applications (CEA) package is primarily used in determining chemical equilibrium compositions and properties of complex mixtures. The use of this software extends to assigned thermodynamic states, rocket performance, Chapman-Jouguet detonations, and shock-tube parameters for incident and reflected shocks. The included thermodynamic database consists of over 1900 species, both gaseous and condensed. Product states are obtained by minimization of Gibbs free energy through variation in the system temperature and composition. In the present study, the use of this package has been limited to calculations involving assigned thermodynamic states.

Within the equilibrium code, certain assumptions have been made to simplify the calculations that require addressing. In particular, the volume of the condensed species in the product state are neglected, which may contribute to differences between the predicted and experimental values. To ensure that the current package accurately captures the equilibrium state of the condensed reactants, some preliminary calculations were performed.

5.2.1 Treatment of condensed species

To determine the effect of negligible volumes for condensed species in the product state, calculations were performed to investigate this effect on the equilibrium pressure for stoichiometric Al-CuO at various loadings. In these calculations, it was assumed that the volume of condensed species in the products was equal to that of the reactants. This was achieved by adjustment of the loading density via

$$\rho_{actual} = \frac{m_{reactants}}{V_{actual}} = \frac{m_{reactants}}{V_{container} - V_{reactants}} \tag{5.14}$$

where the volume of reactants was dynamically adjusted based on the mass of reactants by

$$V_{reactants} = \frac{m_{reactants}}{TMD} \tag{5.15}$$

Thus the loading density was solely a function of the mass of thermite in the mixture, given by

$$\rho_{actual} = \frac{m_{reactants}}{V_{container} - \frac{m_{reactants}}{TMD}} \tag{5.16}$$

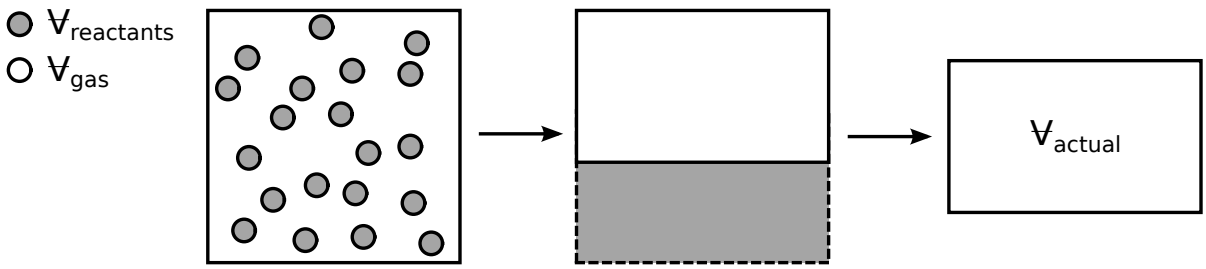

Figure 5.1: Representation of the adjusted volume used in the calculations on the effect of reactant volume.

Dividing through by the volume of the container ($V_{container}$), this is reduced to a function of the pre-volume considerations density (ρ) by

$$\rho_{actual} = \frac{\rho}{1 - \frac{\rho}{TMD}} \tag{5.17}$$

The effect of this treatment is shown in Fig. 5.1. This calculation thus provides an adequate estimate since not all of the products of the reaction are condensed phase species, though some of the condensed products may be less dense than the reactants. Calculations were carried out for loadings of less than 50% TMD, as any higher would result in values of ρ_{actual} exceeding the theoretical maximum density. The results of this calculation are shown in Fig. 5.2.

It is evident that the calculations with volume considerations result in higher pressures owing to the loss in volume. Furthermore, this effect becomes more important at higher loadings owing to higher gas-generation in smaller volumes. To further evaluate this effect, the pressure difference between the two scenarios is shown on the right axis, whereby the highest pressure difference is found to be approximately 1000 kPa. This constitutes an error of less than 10% for calculations without volume considerations.

For the purposes of the present study, the results of this investigation suggest that computational errors from volume considerations are less than approximately 5% owing to the fact that calculations were performed for relative density ratios between approximately 1 and 5%.

5.2.2 Comparison with other chemical equilibrium packages

To further evaluate the validity of the results obtained from NASA's CEA package for condensed phase reactants, calculations for the constant-pressure reaction of an Al-MoO_3 thermite mixture were performed and compared with results from Dutro *et al.* (2009).

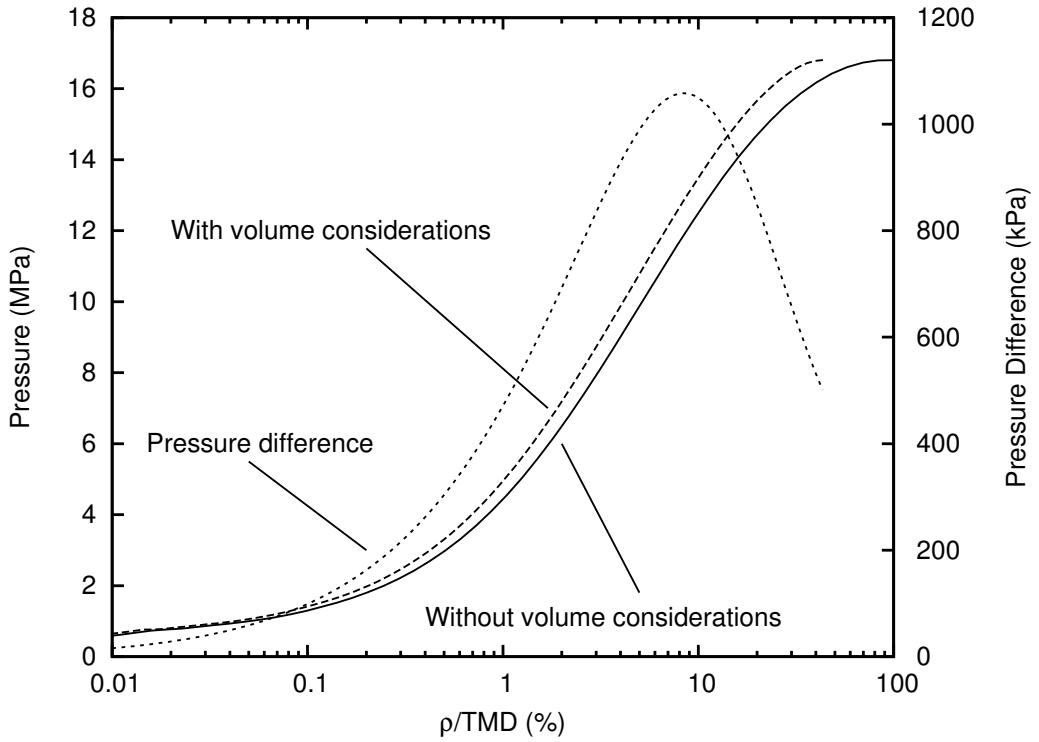

Figure 5.2: Comparison of equilibrium pressures for constant-volume calculations with and without volume considerations for the condensed species.

In their calculations, CHEETAH 4.0, a thermochemical equilibrium code developed by Lawrence Livermore National Laboratories (Fried *et al.*, 2004), was used with a modified version of the JCSZ product library (Hobbs *et al.*, 1999). A constant one atmopshere pressure problem was considered with a relative loading density of 6% TMD. Air was included to occupy the remaining volume fraction not occupied by the thermite mixture. Nano-scale aluminium powders were assumed to consist of 81% Al and 19% Al_2O_3. Calculations for the adiabatic temperature and species concentrations were performed as a function of the equivalence ratio (Φ) defined as

$$\Phi = \frac{\left(\frac{N_{fuel}}{N_{oxid}}\right)_{actual}}{\left(\frac{N_{fuel}}{N_{oxid}}\right)_{stoich}} \tag{5.18}$$

where the stoichiometric fuel-oxidizer ratio is 2:1. These calculations were repeated using NASA's CEA package. The python script implemented for these calculations is shown in Appendix F.1. The results of both series of calculations are shown in Fig. 5.3 where the adiabatic temperature is shown on the left axis and the total gas products are shown

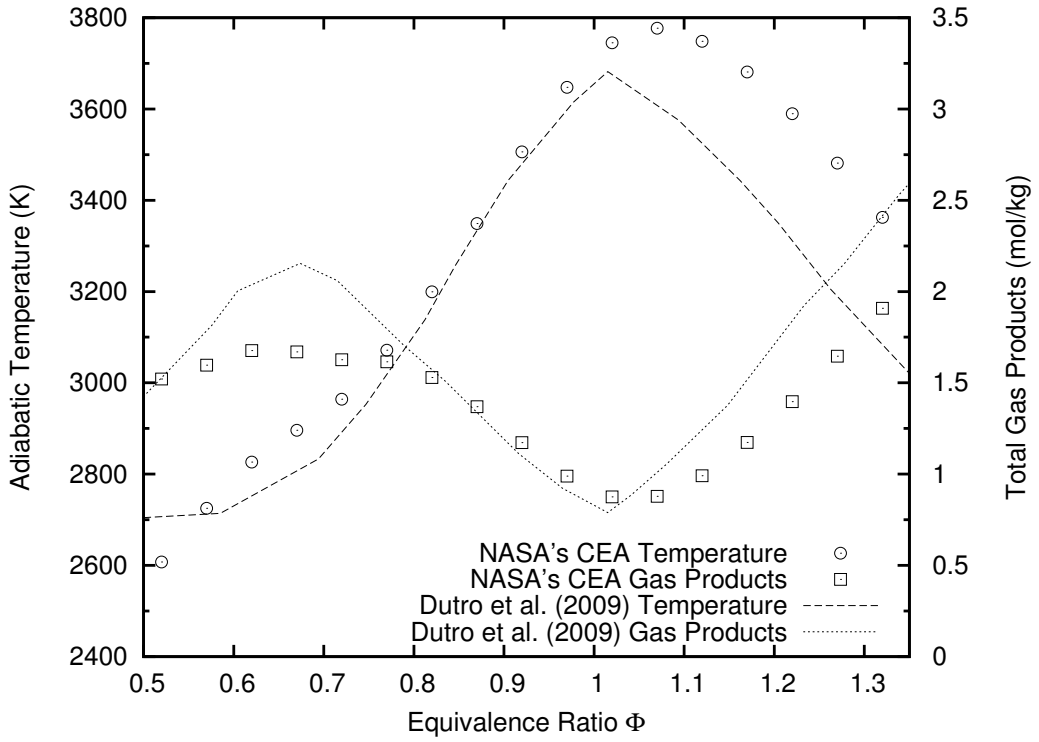

Figure 5.3: Comparison of adiabatic temperature and the total gas products produced by Al-MoO_3 as a function of the equivalence ratio, compared with results from Dutro *et al.* (2009).

on the right.

It is found that CEA is able to accurately capture the results obtained by Dutro *et al.* (2009). Values for the adiabatic temperature are consistently within 100 K of the reference values for fuel-lean mixtures and approximately 200 K for fuel-rich mixtures. Similarly, the total amount of gas products is also found to be well-represented by CEA, which follows closely the curves produced by Dutro *et al.*. In particular, values obtained at stoichiometric conditions ($\Phi = 1$) are found to agree very well with reference data.

5.3 Implementation and results

In the present study, calculations were performed to compare with experimental results of the constant-volume pressure measurements present in Section 4.3. To replicate these experiments, a stoichiometric mixture of Al-CuO was reacted at constant-volume for relative densities between 0.01 and 100% TMD.

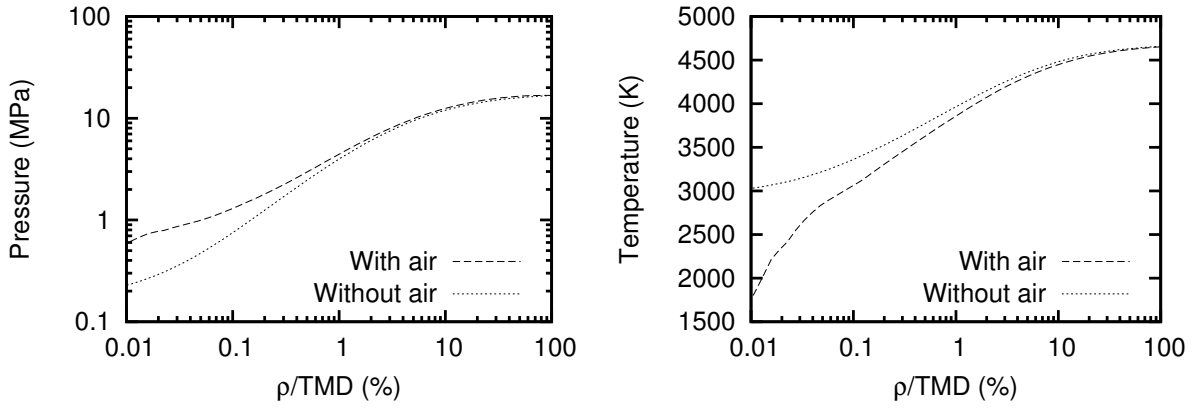

(a) Pressure **(b)** Temperature

Figure 5.4: Results for the equilibrum (a) pressure and (b) temperature for stoichiometric Al-CuO as a function of increasing relative density.

To determine whether or not the presence of air significantly affected the equilibrium pressure and temperature, two cases were evaluated. In one case, air was added at atmospheric pressure in quantities representative of the volume unoccupied by the condensed species. In the other case, only the condensed species were considered. The python script implemented for these calculations is shown in Appendix F.2. Results for the pressure and adiabatic temperature are shown in Figs. 5.4a and 5.4b, respectively.

It was determined that the presence of air only becomes significant for relative densities below approximately 1% TMD in terms of both pressure and temperature. This result suggests that at high relative densities any reactions between the condensed species and the air are not significantly affecting the performance of the thermite. However, at low relative densities, the small amount of gaseous products being formed by the reaction of the thermite mixture results in the air having a significant effect on the reaction products.

This effect can be identified by inspection of the product species for both cases, as shown in Fig. 5.5 and 5.6. For reactions in the presence of air, the main reaction products are gaseous NO_2, liquid Cu, liquid Al_2O_3 and gaseous Cu. At low relative densities, NO_2 from the reaction between the thermite mixture and air is the most prominent in the products. However, between 0.1 and 1% TMD the product species shift nearly entirely to liquid Cu, liquid Al_2O_3 and gaseous Cu, which are the main products from the thermite reaction. This result is confirmed by inspection of the product species when air is not

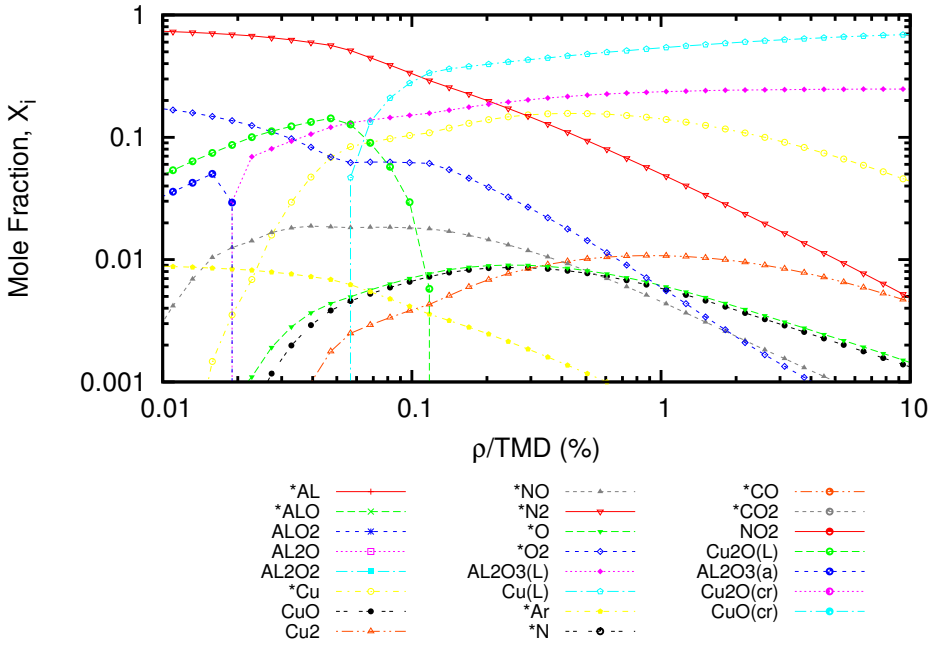

Figure 5.5: Mole fractions of product species for stoichiometric Al-CuO in the presence of air as a function of increasing relative density.

included, which results predominantly in the formation of liquid Cu, liquid Al_2O_3 and gaseous Cu.

Comparison between the equilibrium pressures predicted by CEA with experimental results from the current investigation and reference material (Sullivan *et al.*, 2010; Malchi *et al.*, 2008; Weismiller *et al.*, 2011) is presented in Fig. 5.7. Experiments indicate that the values predicted without considerations for air provide the best approximation for low relative densities. For higher densities, both curves reasonably predict the peak pressure for constant-volume measurements. Experiments conducted in the current investigation were found to result in lower peak pressures than the values predicted by NASA's CEA, with an average deviation of approximately 60%. This effect is most prominent for the results obtained from micron-scale mixtures, a finding consistent with results obtained by Weismiller *et al.* (2011). In general,the predicted values correspond fairly well with the experimentally observed pressures. As a result, numerical calculations performed by NASA's CEA were shown to successfully predict the performance of micro- and nano-scale energetics.

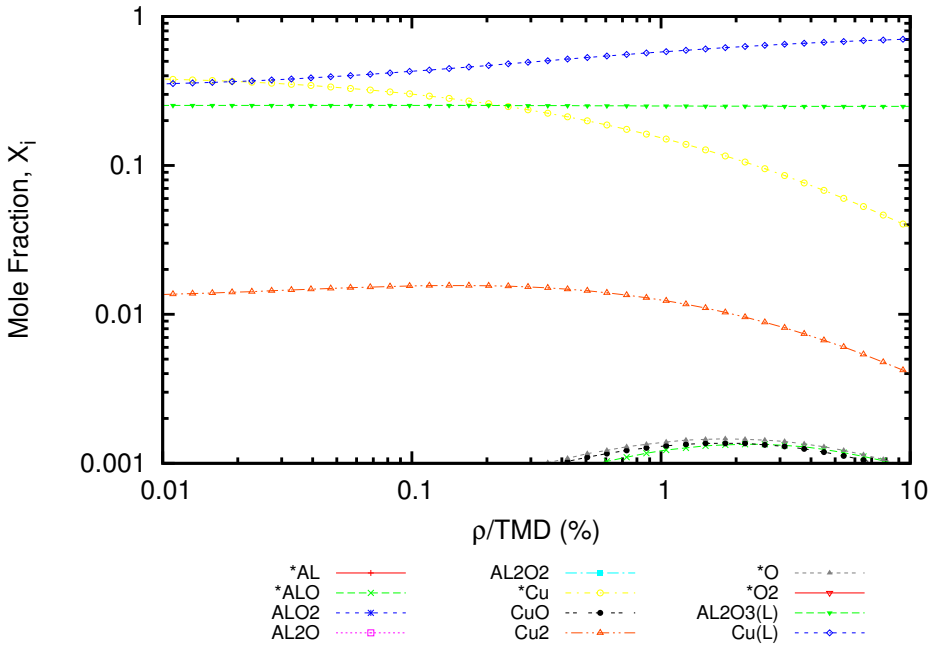

Figure 5.6: Mole fractions of product species for stoichiometric Al-CuO in the absence of air as a function of increasing relative density.

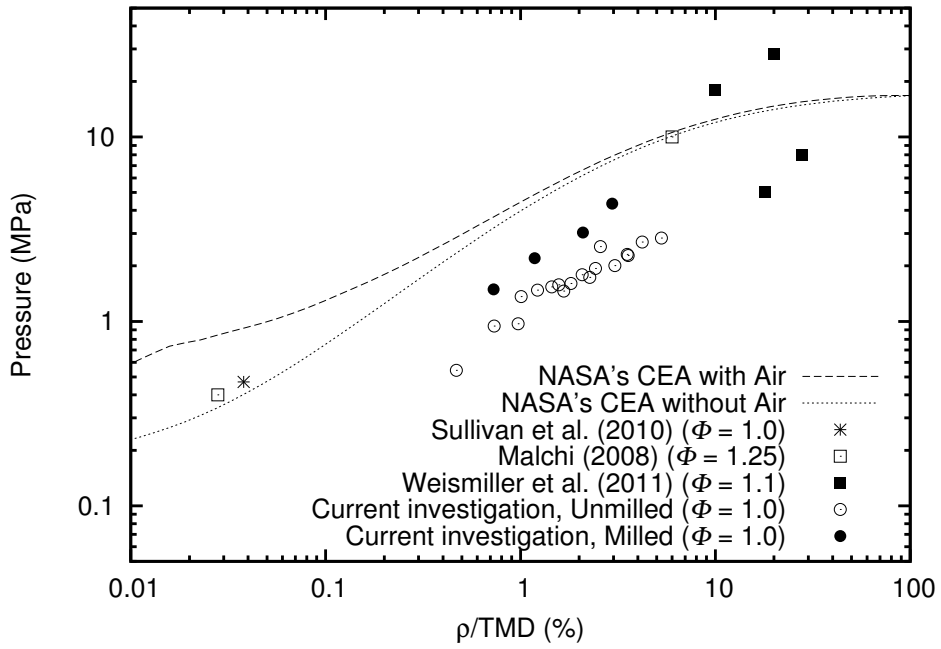

Figure 5.7: Comparison of thermochemical equilibrium pressure with experimental data from the current investigation and various sources.

Chapter 6

Predictions of the pressure signature in water

During an underwater explosion, it has been shown that there exist two distinct phenomena occurring over vastly different time scales. These phenomena are shown schematically in Fig. 6.1. Initially, a pressure wave is emitted from the reacting charge, which travels radially outward at a constant speed, reflecting off the surrounding surfaces as illustrated by Fig. 6.1a. This is followed by the expansion of the hot gaseous products into the surrounding medium as shown by Fig. 6.1b.

In the framework of the present study, it is desirable to predict the shape of the

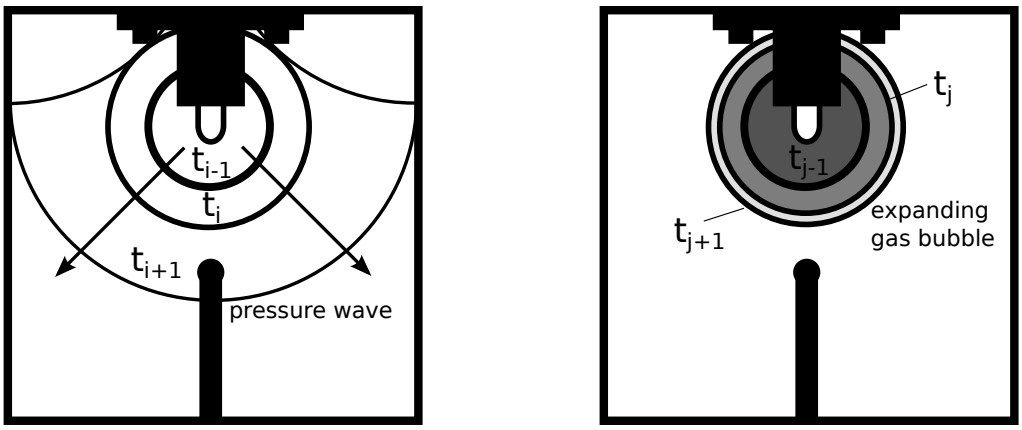

(a) **(b)**

Figure 6.1: Schematic representation of (a) the generated pressure wave transmitting through the surrounding medium, and (b) the evolution of the high-pressure gas bubble.

pressure waves emit from the reaction of the thermite mixture by evaluation of the dynamics of the gas bubble. Predictions for the pressures obtained by the constant-volume reaction can then be linked to the motion of the hot gas bubble, which would provide estimates of the resulting pressure signatures. This chapter attempts to make predictions of these pressure signatures based on the motion of the gas sphere.

6.1 Methods for modeling underwater explosions

To date, several methods for modeling the pressure wave emitted by an underwater explosion have been developed. The simplest, Taylor (1946), is a calculation of the acoustic wave emitted by an expanding sphere with the assumption that only small changes in the medium's density occur. In this analysis, the pressure and velocity functions for a sphere expanding at a prescribed rate can be obtained by solution of the one-dimensional, irrotational wave equation. However, by assuming small changes in density, this theory is thus a linear calculation that does not capture non-linearities within the flow-field.

While Taylor (1946) was able to model waves of small amplitude, a more refined analytical approach to the propagation of waves of finite amplitude was developed by Kirkwood & Bethe (1942). In their analysis, the solution to the hydrodynamic relations is presented under the assumption that the propagation of a spherical pressure wave can be described in terms of a kinetic enthalpy in which differences in entropy are negligible. This treatment provides an approximate solution to the equations of motion in a form whereby the boundary conditions at the gas sphere can be practically applied. Numerical estimates by Kirkwood on the error associated with these approximations lead to the conclusion that this model over-predicts pressures by as much as 20%.

To avoid the complications associated with simplifications of the governing equations, hydrodynamic simulations of underwater explosions can be used to numerically solve the equations of motion. In particular, a wide variety of hydrodynamical simulations of underwater explosions have been evaluated to determine both the motion of the high-pressure gas bubble and the emitted pressure wave. These methods vary from simple, one-dimensional interpretations of the governing equations (Wardlaw & Mair, 1998) to multi-dimensional, multi-phase investigations (Farhat *et al.*, 2008; Kitagawa *et al.*, 2012; Miller *et al.*, 2013). In addition, many numerical models have investigated the dynamics of underwater explosions near free surfaces and solid bodies in an effort to quantify potential submarine and ship damage (Krieger & Chahine, 2005; Kan *et al.*, 2005). While these methods have shown good agreement with experimental results for the bubble

motion and the pressures of the emitted wave, the governing equations and their solutions are complex.

However, for the purposes of the present study, the first strategy is adopted in which a simple solution in closed form is obtained. While this method lacks the ability to capture the geometry of the problem as well as non-linearities in the flow-field, it provides a simple, linear approximation of the pressure profile with easily identifiable scaling parameters. This model is used as a first approximation, and its validity will be discussed in the following sections.

6.2 Derivation of the model

Following the early work of Taylor (1946) and Strehlow (1979), the pressure and velocity fields produced by an expanding sphere in an infinite medium can be obtained. By use of this model, it is assumed that there exists a spherically symmetric high-pressure gas bubble expanding outward into the surrounding medium, which expands at a velocity much smaller than the local sound speed. For a one-dimensional, irrotational flow with a spherically symmetric geometry, the solution to the wave equation has the form

$$\phi = \frac{f(r-ct)}{r} + \frac{g(r+ct)}{r} \tag{6.1}$$

where f and g are arbitrary functions describing outward and inward traveling waves, and ϕ is the velocity potential. For any physical solution compatible with the initially quiescent conditions and the boundary condition of an expanding sphere, the inward traveling wave is non-existent and thus the function $g(r+ct) = 0$ for all t. The velocity potential is related to velocity and pressure disturbances by

$$V = \frac{\partial \phi}{\partial r} = \frac{f'(r-ct)}{r} - \frac{f(r-ct)}{r^2} \tag{6.2}$$

$$p = -\rho \frac{\partial \phi}{\partial t} = \rho c \frac{f'(r-ct)}{r} \tag{6.3}$$

By formulating an expression for the velocity potential, the velocity and pressure in the far-field region can be obtained. In order to do so, the change in volume of the radially expanding sphere can be modeled as a source of mass. A source of mass is characterized by its density, assumed to be constant, and the change of volume as a function of time

$$\frac{dm}{dt} = \rho \frac{dV}{dt} \tag{6.4}$$

The change in volume can also be expressed in terms of the velocity flux across the surface of the mass source of infinitely small size

$$\frac{dm}{dt} = \rho \lim_{r\to 0} \left(4\pi r^2 V\right) = \rho Z(t) \tag{6.5}$$

where the volume flux of fluid is $Z(t) = \frac{dV}{dt} = \lim_{r\to 0}(4\pi r^2 V)$. Using this volume flux equation, one can obtain an expression for the waveform function f. This is done by substitution of Equation (6.2) into the expression for $Z(t)$

$$\begin{aligned} Z(t) &= \lim_{r\to 0}\left(4\pi r^2 \frac{\partial \phi}{\partial r}\right) \\ &= \lim_{r\to 0}\left[4\pi r^2\left(\frac{f'(r-ct)}{r} - \frac{f(r-ct)}{r^2}\right)\right] \\ &= \lim_{r\to 0}\left[4\pi r f'(r-ct) - 4\pi f(r-ct)\right] \\ &= -4\pi f(-ct) \end{aligned} \tag{6.6}$$

Setting a dummy variable $\xi = -ct$, an expression is obtained for the waveform function f in terms of the volume flux as

$$f(\xi) = -\frac{1}{4\pi} Z\left(-\frac{\xi}{c}\right) \tag{6.7}$$

from which the velocity potential can be simplified from Equation (6.1) as

$$\begin{aligned} \phi &= \frac{f(r-ct)}{r} \\ &= -\frac{1}{4\pi r} Z\left(-\frac{r-ct}{c}\right) \\ &= -\frac{1}{4\pi r} Z\left(t - \frac{r}{c}\right) \end{aligned} \tag{6.8}$$

Substitution of this equation into Equations (6.2) and (6.3) yields the velocity and pressure fields in the far-field region as

$$V(r,t) = \frac{\partial \phi}{\partial r} = \frac{1}{4\pi c r^2}\left[r\frac{dZ}{dt}\left(t - \frac{r}{c}\right) + cZ\left(t - \frac{r}{c}\right)\right] \tag{6.9}$$

$$p(r,t) = -\rho\frac{\partial \phi}{\partial t} = \frac{\rho}{4\pi r}\frac{dZ}{dt}\left(t - \frac{r}{c}\right) \tag{6.10}$$

It is important to note that the velocity and pressure are both functions of the derivative of the volume flux, *i.e.*, the acceleration of the volume as a function of time. Thus, with the known trajectory of the bubble radius, one can calculate the acceleration of the bubble volume and re-construct the pressure and velocity profiles resulting from the bubble's expansion.

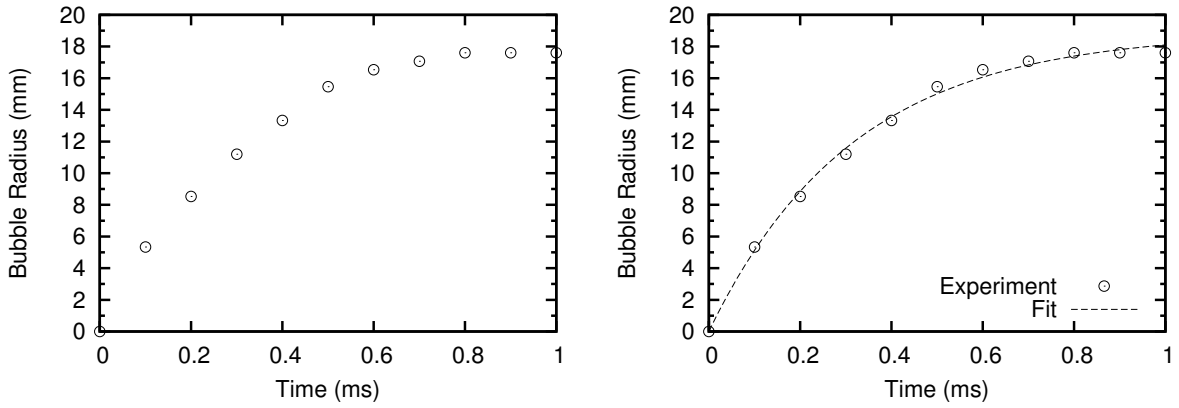

Figure 6.2: (a) Experimental measurements of the bubble radius as a function of time and (b) results of the fit produced by Equation (6.11) (Table C.2, No. 36).

6.3 Formulation of the problem

To estimate the pressures by the motion of the high-pressure gas bubble, the trajectory of the bubble radius was obtained as a function of time by use of the sequential frames acquired by the high-speed camera. ImageJ was used to measure the radius of the bubble from the photographs. Figure 6.2a shows the trajectory of the gas bubble as a function of time for a typical experiment. The trajectory of the bubble path is found to be well approximated by an inverse exponential function of the form

$$R(t) = A\left(1 - e^{-\frac{t}{\tau}}\right) \tag{6.11}$$

where A and τ are fit parameters corresponding to the amplitude of the curve and the time-scale for reaching an equilibrium position, respectively. Values for these parameters were obtained using a least-squares fit of the experimental data. Comparison of the resulting fit equation and experimental data is shown in Fig. 6.2b.

By use of this procedure, it has been assumed that there exists a spherically-symmetric high-pressure bubble expanding outward into the surrounding medium. Furthermore, this bubble expands at a velocity much smaller than the local sound speed as mentioned in Chapter 4.

6.4 Implementation and results

With the assumption of a spherically symmetric gas bubble, the volume of the disturbance is obtained from the previously measured bubble radius, Equation (6.11), via

$$V(t) = \frac{4}{3}\pi R(t)^3 \tag{6.12}$$

Moreover, the volumetric acceleration of the bubble ($\frac{dZ}{dt}$) can be obtained by the

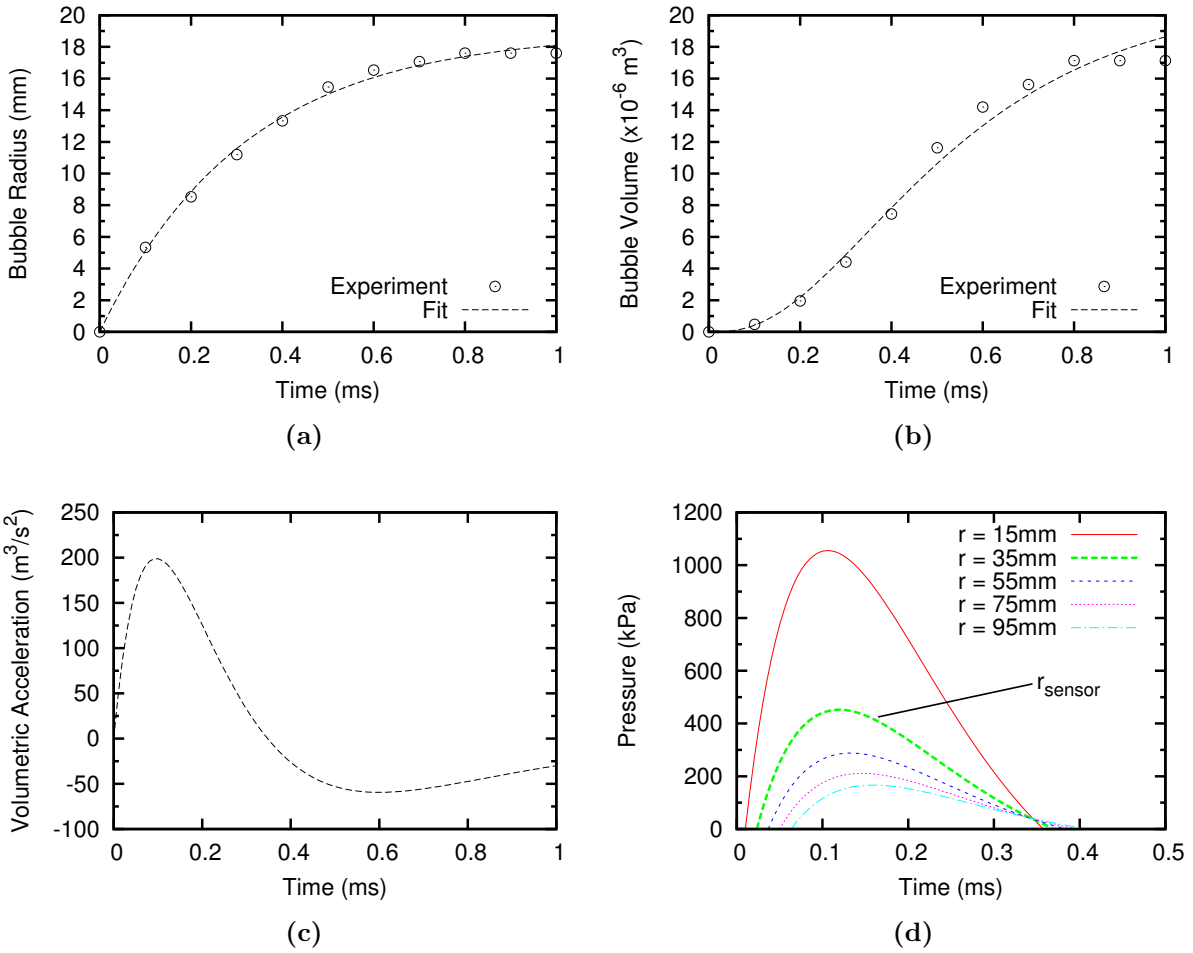

Figure 6.3: Results of the acoustic model for (a) representing the bubble radius as a function of time, (b) volumetric expansion of the bubble, (c) acceleration of the bubble volume, and (d) pressure signals at varying locations from the charge (Table C.2, No. 36).

second-order differentiation of Equation (6.12), yielding

$$\frac{dZ(t)}{dt} = -\frac{4\pi A^3}{\tau^2} e^{-\frac{3t}{\tau}} \left(e^{\frac{t}{\tau}} - 3\right)\left(e^{\frac{t}{\tau}} - 1\right) \tag{6.13}$$

Finally, substitution of Equation (6.13) into Equation (6.10) yields a solvable expression for the pressure history as

$$p(r,t) = -\frac{\rho A^3}{r\tau^2} e^{-\frac{3(t-\frac{r}{c})}{\tau}} \left[e^{\frac{(t-\frac{r}{c})}{\tau}} - 3\right]\left[e^{\frac{(t-\frac{r}{c})}{\tau}} - 1\right] \tag{6.14}$$

Values of the density (ρ) and sound speed (c) of 1000 kg/m^3 and 1500 m/s, respectively, were used to represent the water.

Figure 6.3 shows the results of the presented model. In particular, the bubble's trajectory, volume, volumetric acceleration and the far-field pressure field produced by its expansion are shown.

Data for the bubble radius and volume are found to be well-represented by Equation (6.11). Initially, the bubble grows rapidly followed by a deceleration until a steady volume is reached. This behaviour is further identified by the volumetric acceleration of the gas bubble, whereby the volume rapidly accelerates over the first 100 μs followed by a slow deceleration. This rapid acceleration of the bubble volume leads to compressions in the surrounding medium forming a series of acoustic pressure waves. The behaviour of this pressure wave, as represented by Equation (6.14), is shown for varying locations from the center of the charge in Fig. 6.3d.

To compare the predicted pressure signatures with those obtained experimentally, a sensor location (r) of 35 mm was used. Figure 6.4 shows a comparison of the predicted pressure and the experimental pressure over both short and long time scales. Figure 6.4a shows that the the predicted signature over-estimates the amplitude and time-scale of the pressure wave for the presented experiment. Furthermore, it is found that the rate at which the pressure rises is slightly lower than experiment. After approximately 120 μs, wave reflections from surrounding surfaces are found to complicate the shape of the pressure profile.

6.5 Discussion and recommendations

Results of this model indicate that the predicted pressure is comparable to the experimental data in terms of both magnitude and wave shape for early times, prior to any reflections. However, in all cases the predicted pressure signature is found to have a lower

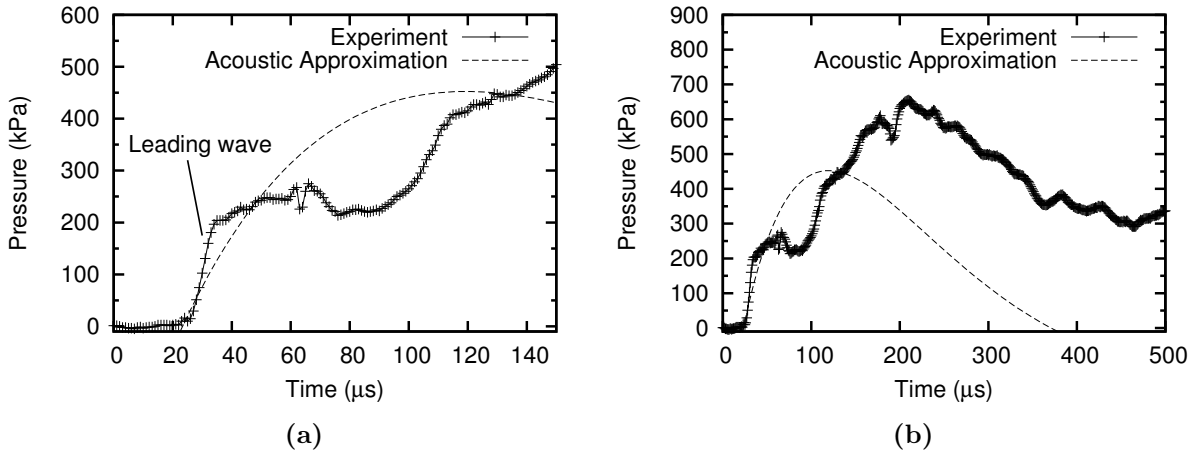

Figure 6.4: Comparison of the estimated pressure with experimental data over (a) short and (b) long time scales (Table C.2, No. 36).

pressurization rate than the experiment. This is likely a result of certain assumptions in the formulation of the model. In particular, the presented model is a first-order treatment of the pressures waves emitted by a spherical disturbance, which does not capture non-linearities in the flow-field. These non-linearities are well-known to cause a steepening of the pressure wave by the accumulation of pressure waves, which would lead to the higher pressurization rates observed experimentally. In an effort to accurately represent this behaviour, future work should consider the approximations by Kirkwood & Bethe (1942) who reported on the pressure wave produced in an underwater explosion. In their treatment, the pressure waves are assumed to propagate as a function of the local, pressure dependent velocity. This assumption permits for resolving the nonlinear wave propagation resulting from the pressure dependence of the sound speed.

Chapter 7

Conclusions

The performance of a fully-dense nano-scale mixture of stoichiometric Al-CuO prepared by mechanical alloying for applications in cellular transfection and drug delivery was evaluated experimentally and compared with conventional nano-scale mixtures previously reported by Apperson *et al.* (2008). Preliminary investigations on the reactive characteristics of the mechanically alloyed mixtures compared with both conventional nano-scale and micron-scale mixtures were conducted experimentally. In particular, the flame propagation speed and pressure dynamics in a constant-volume reactor were evaluated.

Results indicated that mechanically alloyed mixtures result in an increase in flame propagation speeds by as much as two orders of magnitude compared with micron-scale mixtures, which was found to be smaller but comparable to those previously obtained for conventional nano-scale mixtures. This increased reactivity was attributed to the newly-formed nano-scale mixing between the reactants, which reduces the time scale for diffusion between particles. In constant-volume experiments, mechanically alloyed mixtures were found to result in both higher peak pressures and pressurization rates compared with micron-scale mixtures. In particular, mechanically alloyed mixtures produced pressurization rates approximately one order of magnitude higher than micron-scale thermites, which were, however, found to be approximately one order of magnitude lower than conventional nano-scale thermites. Although a significant improvement was observed relative to micron-scale mixtures, the lower pressurization rates compared with nano-scale mixtures is likely attributed to the significant dependence of pressurization rate on the flame propagation speed. Furthermore, the pressures observed experimentally were compared with values predicted by thermochemical equilibrium calculations

performed using NASA'S CEA. Experimental data was found to agree fairly well with the predicted values.

Results of the underwater measurements indicated that mechanically alloyed samples result in higher pressures of the leading wave and shorter impulses compared with the micron-scale mixture. Compared with conventional nano-scale mixtures, the wave-shapes obtained by mechanically alloyed mixtures were found to be similar in shape to those observed by Apperson *et al.* (2008) for a nano-scale mixture of Al-Bi_2O_3. While values of the maximum pressure and impulse were higher for the Al-Bi_2O_3 system, these differences may be attributed to differences in the reactivity of the two mixtures. As a result, the mixtures produced by mechanical alloying appear to produce wave shapes that may be conducive to cellular transfection, though further work with actual cells is required.

In an effort to predict the pressures generated by the leading wave in underwater experiments, simple acoustic theory was found to provide a reasonable estimation, however, pressurization rates were under-predicted. This under-prediction was attributed to the simplifying linear assumption inherent to the model. In order to improve these predictions, a model that takes into account differences in the local sound speed may result in a better representation of the experiments.

Bibliography

Akbarnejad, H. 2013 Influence of porosity on the flame speed in gasless bimetallic reactive systems. Master's thesis, University of Ottawa.

Aly, Y., Schoenitz, M. & Dreizin, E. L. 2013 Ignition and combustion of mechanically alloyed Al–Mg powders with customized particle sizes. *Combustion and Flame* **160**, 835–842.

Apperson, S., Shende, R. V., Subramanian, S., Tappmeyer, D. & Gangopadhyay, S. 2007 Generation of fast propagating combustion and shock waves with copper oxide/aluminum nanothermite composites. *Applied Physics Letters* **91**, 243109.

Apperson, S., Thiruvengadathan, R., Bezmelnitsyn, A., Gangopadhyay, K., Gangopadhyay, S. & Polo-Parada, L. 2008 Nanothermite-based microsystem for drug delivery and cell transfection. *Tech. Rep.*. Defense Technical Information Center (DTIC) Document.

Bacciochini, A., Radulescu, M. I., Yandouzi, M., Maines, G., Lee, J. J. & Jodoin, B. 2013 Reactive structural materials consolidated by cold spray: Al–CuO thermite. *Surface & Coatings Technology* **226**, 60–67.

Bellard, F. 2000 FFmpeg: An open-source command-driven multimedia conversion software. Accessed June, 2013.

Campbell, T., Kalia, R. K., Nakano, A., Vashishta, P., Ogata, S. & Rodgers, S. 1999 Dynamics of oxidation of aluminum nanoclusters using variable charge molecular-dynamics simulations on parallel computers. *Physical Review Letters* **82** (24), 4866–4869.

Cole, R. H. 1948 *Underwater explosions*. Princeton, Princeton Univ. Press.

Dutro, G. M., Yetter, R. A., Risha, G. A. & Son, S. F. 2009 The effect of stoichiometry on the combustion behavior of a nanoscale Al/MoO_3 thermite. *Proceedings of the Combustion Institute* **32** (2), 19211928.

Ermoline, A., Schoenitz, M. & Dreizin, E. L. 2011 Reactions leading to ignition in fully dense nanocomposite Al-oxide systems. *Combustion and Flame* **158** (6), 1076–1083.

Ermoline, A., Stamatis, D. & Dreizin, E. L. 2012 Low-temperature exothermic reactions in fully dense Al-CuO nanocomposite powders. *Thermochimica Acta* **527**, 52–58.

Farhat, C., Rallu, A. & Shankaran, S. 2008 A higher-order generalized ghost fluid method for the poor for the three-dimensional two-phase flow computation of underwater implosions. *Journal of Computational Physics* **227**, 7674–7700.

Fischer, S. H. & Grubelich, M. C. 1996 *A survey of combustible metals, thermites, and intermetallics for pyrotechnic applications*. Defense Technical Information Center (DTIC) Document.

Fried, L. E., Glaesemann, K. R., Howard, W. M., Souers, P. C. & Vitello, P. A. 2004 CHEETAH 4.0. Lawrence Livermore National Laboratory.

Granier, J. J., Plantier, K. B. & Pantoya, M. L. 2004 The role of the Al2O3 passivation shell surrounding nano-al particles in the combustion synthesis of NiAl. *Journal of materials science* **39** (21), 6421–6431.

Hobbs, M. L., Baer, M. R. & McGee, B. C. 1999 JCZS: an intermolecular potential database for performing accurate detonation and expansion calculations. *Propellants, Explosives, Pyrotechnics* **24** (5), 269–279.

Hunt, E. M. & Pantoya, M. L. 2005 Ignition dynamics and activation energies of metallic thermites: From nano-to micron-scale particulate composites. *Journal of Applied Physics* **98** (3), 034909–034909.

Kan, K., Stuhmiller, J. H. & Chan, P. C. 2005 Simulation of the collapse of an underwater explosion bubble under a circular plate. *Shock and Vibration* **12** (3), 217–225.

Keller, J. B. & Kolodner, I. I. 1956 Damping of underwater explosion bubble oscillations. *Journal of Applied Physics* **27** (10), 1152–1161.

Kendall, M. A. F 2002 The delivery of particulate vaccines and drugs to human skin with a practical, hand-held shock tube-based system. *Shock Waves* **12**, 23–30.

Kirkwood, J. G. & Bethe, H. A. 1942 Progress report on the pressure wave produced by an underwater explosion. *Tech. Rep.*. OSRD report No. 4814.

Kitagawa, K., Ishiguro, F., Abe, A. & Tanaka, Y. 2012 Underwater shock wave induced bubble explosions in water and silicone oil. *Science and Technology of Energetic Materials* **73** (4), 93–97.

Kodama, T., Doukas, A. G. & R., Hamblin M. 2002 Shock wave-mediated molecular delivery into cells. *Biochimica et Biophysica Acta* **1542**, 186–194.

Kodama, T., Doukas, A. G. & R., Hamblin M. 2003 Delivery of ribosome-inactivating protein toxin into cancer cells with shock waves. *Cancer Letters* **189**, 69–75.

Kodama, T., R., Hamblin M. & Doukas, A. G. 2000 Cytoplasmic molecular delivery with shock waves: Importance of impulse. *Biophysical Journal* **79**, 1821–1832.

Koshiyama, K., Kodama, T., Yano, T. & S., Fujikawa 2006 Structural change in lipid bilayers and water penetration induced by shock waves: Molecular dynamics simulations. *Biophysical Journal* **91**, 2198–2205.

Krieger, J. R. & Chahine, G. L. 2005 Acoustic signals of underwater explosions near surfaces. *Journal of the Acoustical Society of America* **118** (5), 2961–2974.

Lee, S., McAuliffe, D. J., Kodama, T. & Doukas, A. G. 2000 In vivo transdermal delivery using a shock tube. *Shock Waves* **10**, 307–311.

Malchi, J. Y., Yetter, R. A., Foley, T. J. & Son, S. F. 2008 The effect of added Al2O3 on the propagation behavior of an Al/CuO nanoscale thermite. *Combustion Science and Technology* **180** (7), 1278–1294.

McBride, B. J. & Gordon, S. 2002 NASA Chemical Equilibrium with Applications (CEA).

McWhirter, J. D., Crawford, M. E. & Klein, D. E. 1997 Wall region porosity distributions for packed beds of uniform spheres with modified and unmodified walls. *Transport in Porous Media* **27**, 99–118.

Miller, S. T., Jasak, H., Boger, D. A., Paterson, E. G. & Nedungadi, A. 2013 A pressure-based, compressible, two-phase flow finite volume method for underwater explosions. *Computers & Fluids* **87**, 132–143.

Rasband, W. 1997 ImageJ: A java-based image-processing program. National Institutes of Health (NIH), Accessed June, 2013.

Schoenitz, M., Umbrajkar, S. & Dreizin, E. L. 2007 Kinetic analysis of thermite reactions in Al-MoO_3 nanocomposites. *Joutnal of Propulsion and Power* **23** (4), 683–687.

Schoenitz, M., Ward, T. & Dreizin, E. L. 2004 Preparation of energetic metastable nano-composite materials by arrested reactive milling. *Materials Research Society Symposium Proceedings* **800**.

Schoenitz, M., Ward, T. S. & Dreizin, E. L. 2005 Fully dense nano-composite energetic powders prepared by arrested reactive milling. *Proceedings of the Combustion Institute* **30** (2), 2071–2078.

Settles, G. S. 2001 *Schlieren and Shadowgraph Techniques: Visualizing Phenomena in Transparent Media*. Springer.

Shende, R., Subramanian, S., Hasan, S., Apperson, S., Thiruvengadathan, R., Gangopadhyay, K. & Gangopadhyay, S. 2008 Nanoenergetic composites of CuO nanorods, nanowires, and Al-nanoparticles. *Propellants, Explosives, Pyrotechnics* **33** (2), 122–130.

Stamatis, D., Jiang, Z., Hoffmann, V. K., Schoenitz, M. & Dreizin, E. L. 2008 Fully dense, aluminum-rich al-CuO nanocomposite powders for energetic formulations. *Combustion Science and Technology* **181** (1), 97–116.

Stamatis, D., Zhu, X., Schoenitz, M., Dreizin, E. L. & Redner, P. 2011 Consolidation and mechanical properties of reactive nanocomposite powders. *Powder Technology* **208** (3), 637–642.

Strehlow, R. A. 1979 The blast wave from deflagrative explosions, an acoustic approach. *Tech. Rep.*. Defense Technical Information Center (DTIC) Document.

Sullivan, K. T., Piekiel, N. W., Chowdhury, S., Wu, C., Zachariah, M. R. & Johnson, C. E. 2010 Ignition and combustion characteristics of nanoscale Al/AgIO3: a potential energetic biocidal system. *Combustion Science and Technology* **183** (3), 285–302.

Suryanarayana, C. 2001 Fully dense nano-composite energetic powders prepared by arrested reactive milling. *Progress in Materials Science* **46**, 1–184.

Taylor, G. I. 1946 The air wave surrounding an expanding sphere. *Proceedings of the Royal Society of London A* **186**, 273–292.

Umbrajkar, S., Seshadri, S., Schoenitz, M., K., Hoffmann V. & Dreizin, E. L. 2008 Aluminum-rich Al-MoO_3 nanocomposite powders prepared by arrested reactive milling. *Journal of Propulsion and Power* **24** (2), 192–198.

Umbrajkar, S., Trunov, M. A., Schoenitz, M., Dreizin, E. L. & Broad, R. 2007 Arrested reactive milling synthesis and characterization of sodium-nitrate based reactive composites. *Propellants, Explosives, Pyrotechnics* **32** (1), 32–41.

Umbrajkar, S. M., Schoenitz, M. & Dreizin, E. L. 2006*a* Control of structural refinement and composition in al-moo3 nanocomposites prepared by arrested reactive milling. *Propellants, Explosives, Pyrotechnics* **31** (5), 382–389.

Umbrajkar, S. M., Schoenitz, M. & Dreizin, E. L. 2006*b* Exothermic reactions in Al-CuO nanocomposites. *Thermochimica Acta* **451**, 34–43.

Wang, L., Luss, D. & Martirosyan, K. S. 2011 The behavior of nanothermite reaction based on Bi2O3/Al. *Journal of Applied Physics* **110** (7), 074311–074311.

Wardlaw, A. B. & Mair, H. U. 1998 Spherical solutions of an underwater explosion bubble. *Shock and Vibration* **5**, 89–102.

Weismiller, M. R., Malchi, J. Y., Lee, J. G., Yetter, R. A. & Foley, T. J. 2011 Effects of fuel and oxidizer particle dimensions on the propagation of aluminum containing thermites. *Proceedings of the Combustion Institute* **33** (2), 1989–1996.

Williams, R. A., Patel, J. V., Ermoline, A., Schoenitz, M. & Dreizin, E. L. 2013 Correlation of optical emission and pressure generated upon ignition of fully-dense nanocomposite thermite powders. *Combustion and Flame* **160**, 734–741.

Appendix A

Runlist: Open-channel flame speed experiments

The following table provides the results of individual experiments for the flame propagation speed measurements. Included in the table is the test number, the date the experiment was performed, the mixture stoichiometry, the duration for which the mixture was milled, the mass of the sample, the theoretical maximum density of the sample, the relative density of the sample reported as % TMD, the measured flame propagation speed, the resolution of the camera, the exposure time of the camera, the capture speed of the camera, whether or not the experiment was successful, and any associated comments.

No	Date	Mixture	Mill Time [min]	m_{sample} [mg]	TMD [kg/m^3]	$\frac{\rho}{TMD}$ [%]	V_{flame} [cm/s]	Resolution	t_{exp} [μs]	Speed [fps]	Go	No-Go	Comments
1	06/19/13	2Al-3CuO	0	509	5061.9	25.5	49.1	512×320	1.0	12,003	X		
2	06/19/13	2Al-3CuO	16	484	5061.9	24.2	3676.7	512×320	1.0	12,003	X		
3	06/19/13	2Al-3CuO	16	483	5061.9	24.2	8692.7	512×320	0.8	12,003	X		
4	06/19/13	2Al-3CuO	30	532	5061.9	26.6	3182.3	512×320	1.0	12,003	X		
5	06/19/13	2Al-3CuO	30	539	5061.9	27.0	1625.6	512×320	1.0	20,000	X		
6	06/20/13	2Al-3CuO	0	473	5061.9	23.7	125.9	512×320	1.0	12,003	X		
7	06/20/13	2Al-3CuO	16	387	5061.9	19.4	892.5	512×320	1.0	20,000		X	Difficult tracking
8	06/21/13	2Al-3CuO	16	564	5061.9	28.2	10767.3	512×320	1.0	20,000	X		
9	06/21/13	2Al-3CuO	16	534	5061.9	26.7	7229.0	512×320	1.0	20,000	X		
10	06/24/13	2Al-3CuO	16	570	5061.9	28.5	8674.0	512×320	1.0	20,000	X		
11	06/24/13	2Al-3CuO	16	527	5061.9	26.4	4425.2	512×320	1.0	20,000	X		
12	06/24/13	2Al-3CuO	30	487	5061.9	24.4	1582.2	512×320	1.0	12,003	X		
13	06/24/13	2Al-3CuO	30	487	5061.9	24.4	1843.2	512×320	1.0	12,003	X		
14	06/24/13	2Al-3CuO	46	483	5061.9	24.2	1751.1	512×320	7.0	6,000	X		
15	06/24/13	2Al-3CuO	46	565	5061.9	28.3	189.2	512×320	6.0	6,000	X		
16	06/24/13	2Al-3CuO	46	487	5061.9	24.4	1669.6	512×320	6.0	6,000	X		
17	06/24/13	2Al-3CuO	60	493	5061.9	24.7	1012.8	512×320	10.0	6,000		X	Difficult tracking
18	06/25/13	2Al-3CuO	0	637	5061.9	31.9	228.6	512×320	1.0	6,000	X		
19	06/25/13	2Al-3CuO	0	599	5061.9	30.0	59.5	512×320	1.0	6,000	X		
20	06/25/13	2Al-3CuO	0	600	5061.9	30.0	254.9	512×320	1.0	6,000	X		
21	06/25/13	2Al-3CuO	60	378	5061.9	18.9	328.8	512×320	10.0	6,000	X		
22	06/25/13	2Al-3CuO	60	358	5061.9	17.9	313.6	512×320	10.0	6,000	X		
23	06/25/13	2Al-3CuO	60	383	5061.9	19.1	416.6	512×320	8.0	6,000	X		
24	06/25/13	2Al-3CuO	60	350	5061.9	17.5	421.3	512×320	7.0	6,000	X		
25	06/25/13	2Al-3CuO	46	367	5061.9	18.4	506.5	512×320	6.0	6,000	X		
26	06/25/13	2Al-3CuO	46	323	5061.9	16.2	1260.0	512×320	5.0	6,000	X		
27	06/25/13	2Al-3CuO	46	459	5061.9	23.0	375.2	512×320	5.0	6,000	X		
28	06/25/13	2Al-3CuO	30	327	5061.9	16.4	4017.0	512×320	1.0	12,003	X		
29	06/25/13	2Al-3CuO	30	432	5061.9	21.6	1761.9	512×320	1.0	12,003	X		
30	06/25/13	2Al-3CuO	30	450	5061.9	22.5	1874.9	512×320	1.0	12,003	X		

Table A.1: Runlist for open-channel flame speed experiments.

Appendix B

Runlist: Constant-volume pressure experiments

The following table provides the results of individual experiments for the constant-volume pressure measurements. Included in the table is the test number, the date the experiment was performed, the mixture stoichiometry, the duration for which the mixture was milled, the mass of the sample, the theoretical maximum density of the sample, the relative density of the sample reported as % TMD, the measured peak pressure, the measured peak pressurization rate, the sampling rate of the DAQ, whether or not the experiment was successful, and any associated comments.

No	Date	Mixture	Mill Time [min]	m_{sample} [mg]	TMD [kg/m^3]	$\frac{\rho}{TMD}$ [%]	p_{max} [kPa]	$\left(\frac{dp}{dt}\right)_{max}$ [MPa/s]	Rate [kHz]	Go	No-Go	Comments
1	08/06/13	2Al-3CuO	0	205	5061.9	1.023	1697.7	307.5	10		X	Adhesive tape
2	08/06/13	2Al-3CuO	0	367	5061.9	1.831	2488.8	396.6	10		X	Adhesive tape
3	08/08/13	2Al-3CuO	0	195	5061.9	0.973	971.1	154.4	10	X		
4	08/08/13	2Al-3CuO	0	245	5061.9	1.222	1478.0	341.0	10	X		
5	08/08/13	2Al-3CuO	0	94	5061.9	0.469	542.3	136.5	10	X		
6	08/08/13	2Al-3CuO	0	290	5061.9	1.447	1538.5	610.4	10	X		
7	08/08/13	2Al-3CuO	0	147	5061.9	0.733	943.7	136.8	10	X		
8	08/09/13	2Al-3CuO	0	202	5061.9	1.008	1364.6	285.6	10	X		
9	08/09/13	2Al-3CuO	0	515	5061.9	2.569	2544.3	696.0	10	X		
10	08/09/13	2Al-3CuO	0	334	5061.9	1.666	1460.8	460.1	10	X		
11	08/09/13	2Al-3CuO	0	415	5061.9	2.070	1792.2	445.1	10	X		
12	08/09/13	2Al-3CuO	0	315	5061.9	1.571	1579.2	299.5	10	X		
13	08/09/13	2Al-3CuO	0	364	5061.9	1.816	1605.1	333.4	10	X		
14	08/12/13	2Al-3CuO	0	455	5061.9	2.270	1731.3	451.7	10	X		
15	08/12/13	2Al-3CuO	0	715	5061.9	3.567	2274.4	389.5	10	X		
16	08/12/13	2Al-3CuO	0	845	5061.9	4.215	2690.5	476.2	10	X		
17	08/12/13	2Al-3CuO	0	435	5061.9	2.170	6466.3	458.0	10		X	Paper sleeve
18	08/13/13	2Al-3CuO	0	384	5061.9	2.231	1063.1	258.5	10		X	Steel sleeve
19	08/13/13	2Al-3CuO	0	486	5061.9	2.425	1934.9	721.8	10	X		
20	08/13/13	2Al-3CuO	0	612	5061.9	3.053	2008.2	587.6	10	X		
21	08/13/13	2Al-3CuO	16	237	5061.9	1.182	2202.9	2074.0	10	X		
22	08/28/13	2Al-3CuO	0	707	5061.9	3.527	2308.1	799.2	20	X		
23	08/28/13	2Al-3CuO	0	1060	5061.9	5.288	2828.1	601.0	20	X		
24	08/28/13	2Al-3CuO	16	419	5061.9	2.090	3030.9	3998.4	50	X		
25	08/28/13	2Al-3CuO	16	146	5061.9	0.782	1493.1	1992.2	50	X		
26	08/28/13	2Al-3CuO	16	95	5061.9	0.474	1077.0	1696.7	50		X	Noise
27	08/28/13	2Al-3CuO	16	593	5061.9	2.958	4350.3	7255.7	50	X		

Table B.1: Runlist for constant-volume pressure experiments.

Appendix C

Runlist: Underwater pressure experiments

The following tables provide the results of individual experiments for the underwater measurements. Included in each table is the test number, the date the experiment was performed, the mixture stoichiometry, the duration for which the mixture was milled, the type of light bulb used (1 - cylindrical, 2 - nearly-spherical, gel - gel-capsule), the mass of the sample, the theoretical maximum density of the sample, the relative density of the sample reported as % TMD, the sampling rate of the DAQ, the resolution of the camera, the exposure time of the camera, the capture speed of the camera, the measured pressure of the leading wave, the measured maximum pressure of the wave, the calculated impulse, whether or not the experiment was successful, and any associated comments.

No	Date	Mixture	Mill Time [min]	Bulb	m_{sample} [mg]	TMD [kg/m^3]	$\frac{\rho}{TMD}$ [%]	Rate [kHz]	Resolution	t_{exp} [μs]	Speed [fps]	p_{shock} [kPa]	p_{max} [kpa]	Impulse [kPa-s]	Go	No-Go	Comments
1	06/27/13	2Al-3CuO	0	1	273	5061.9	27.0	50	256×256	0.460	100,000	234.4	990.0	5.07	X		No video
2	06/27/13	2Al-3CuO	0	1	247	5061.9	24.4	50	256×256	0.460	100,000	163.6	820.3	5.94	X		
3	06/27/13	2Al-3CuO	16	1	176	5061.9	17.4	50	256×256	0.460	100,000	430.9	1243.9	1.14	X		
4	06/27/13	2Al-3CuO	0	1	248	5061.9	24.5	50	256×256	0.460	100,000	361.3	954.6	1.47	X		
5	06/27/13	2Al-3CuO	16	1	198	5061.9	19.6	200	256×256	0.460	100,000	571.3	1264.4	2.01	X		
6	06/27/13	2Al-3CuO	0	1	269	5061.9	26.6	200	256×256	0.460	100,000	321.0	1120.6	2.90	X		
7	06/28/13	2Al-3CuO	0	1	278	5061.9	27.5	200	256×256	0.460	100,000	159.9	636.0	0.97	X		
8	06/28/13	2Al-3CuO	0	1	254	5061.9	25.1	200	256×256	0.460	100,000	347.9	1464.8	1.32	X		
9	06/28/13	2Al-3CuO	0	1	261	5061.9	25.8	200	256×256	0.460	100,000	179.4	1601.6	3.45		X	Tape-wrap
10	06/28/13	2Al-3CuO	0	1	99	5061.9	N/A	200	256×256	0.460	100,000	805.7	1116.9	0.63		X	Half bulb, no video
11	06/28/13	2Al-3CuO	0	1	265	5061.9	26.2	200	256×256	0.460	100,000	322.3	817.9	1.51	X		
12	07/03/13	2Al-3CuO	16	1	173	5061.9	17.1	500	256×256	0.460	100,000	N/A	N/A	N/A	X		No pressure, slow
13	07/03/13	2Al-3CuO	16	1	141	5061.9	13.9	500	256×256	0.460	100,000	566.4	784.9	0.68	X		
14	07/03/13	2Al-3CuO	0	1	258	5061.9	25.5	500	256×256	0.460	100,000	346.7	1328.1	2.30	X		
15	07/03/13	2Al-3CuO	0	1	287	5061.9	28.3	500	256×256	0.460	100,000	252.7	1217.0	2.66	X		
16	07/03/13	2Al-3CuO	16	1	166	5061.9	16.4	500	256×256	0.460	100,000	643.3	1071.8	0.82	X		
17	07/03/13	2Al-3CuO	16	1	155	5061.9	15.3	500	256×256	0.460	100,000	478.5	1027.8	0.56	X		
18	07/03/13	2Al-3CuO	0	1	304	5061.9	30.0	500	256×256	0.460	100,000	105.0	852.1	2.37		X	Slow break
19	07/03/13	2Al-3CuO	16	1	172	5061.9	17.0	500	256×256	0.460	100,000	203.9	972.9	1.02		X	Slow break
20	07/05/13	2Al-3CuO	0	1	157	5061.9	15.5	500	256×256	0.460	100,000	185.5	726.3	0.57	X		

Table C.1: Runlist for underwater pressure experiments, part 1. (continued...)

No	Date	Mixture	Mill	Bulb	m_{sample} [mg]	TMD [kg/m^3]	$\frac{\rho}{TMD}$ [%]	Rate [kHz]	Resolution	t_{exp} [μs]	Speed [fps]	p_{shock} [kPa]	p_{max} [kPa]	Impulse [kPa-s]	Go	No-Go	Comments
21	07/05/13	2Al-3CuO	16	1	180	5061.9	17.8	500	256×256	0.460	100,000	761.7	1005.9	0.68	X		
22	09/20/13	2Al-3CuO	0	gel	75	5061.9	N/A	500	256×256	0.460	100,000	N/A	N/A	N/A		X	Bad sample
23	09/20/13	2Al-3CuO	0	gel	61	5061.9	N/A	500	256×256	0.460	100,000	100.1	260.0	0.04		X	Bad sample
24	09/20/13	2Al-3CuO	0	2	109	5061.9	21.5	500	256×256	0.460	100,000	N/A	N/A	N/A	X		No pressure
25	10/08/13	2Al-3CuO	0	2	111	5061.9	21.9	750	256×256	0.468	100,000	N/A	N/A	N/A		X	Faulty wire
26	10/08/13	2Al-3CuO	0	2	131	5061.9	25.9	750	256×256	0.468	100,000	N/A	N/A	N/A		X	PSU error
27	10/08/13	2Al-3CuO	0	2	120	5061.9	23.7	750	256×256	0.468	100,000	285.6	922.9	0.45	X		
28	10/08/13	2Al-3CuO	16	2	128	5061.9	25.3	750	256×256	0.468	100,000	253.9	867.9	0.89	X		
29	10/08/13	2Al-3CuO	16	2	92	5061.9	18.2	750	256×256	0.468	100,000	137.9	621.3	0.80	X		No video
30	10/08/13	2Al-3CuO	0	2	126	5061.9	24.9	750	256×256	0.468	100,000	234.4	637.2	0.25	X		
31	10/08/13	2Al-3CuO	0	2	137	5061.9	27.1	750	256×256	0.468	100,000	227.1	723.9	0.55	X		
32	10/08/13	2Al-3CuO	0	2	109	5061.9	21.5	750	256×256	0.468	100,000	238.0	727.5	0.45	X		
33	10/08/13	2Al-3CuO	16	2	107	5061.9	21.1	1000	256×256	0.468	100,000	443.1	654.3	0.35	X		
34	10/08/13	2Al-3CuO	16	2	119	5061.9	23.5	1000	256×256	0.468	100,000	332.0	704.3	0.64	X		
35	10/08/13	2Al-3CuO	0	2	141	5061.9	27.9	1000	256×256	0.468	100,000	153.8	351.6	0.35	X		
36	10/08/13	2Al-3CuO	0	2	131	5061.9	25.9	1000	256×256	0.468	100,000	229.5	655.5	0.55	X		
37	10/10/13	2Al-3CuO	16	2	145	5061.9	28.6	1000	256×256	0.468	100,000	553.0	944.8	0.59	X		
38	10/10/13	2Al-3CuO	16	2	142	5061.9	28.1	1000	256×256	0.468	100,000	191.7	1464.8	2.58	X		
39	10/10/13	2Al-3CuO	16	2	148	5061.9	29.2	1000	256×256	0.468	100,000	151.4	1193.8	1.93	X		
40	10/10/13	2Al-3CuO	16	2	154	5061.9	30.4	1000	256×256	0.468	100,000	152.6	647.0	0.88	X		

Table C.2: Runlist for underwater pressure experiments, part 2.

Appendix D

Design drawings of the 3.96 mL miniature pressure cell

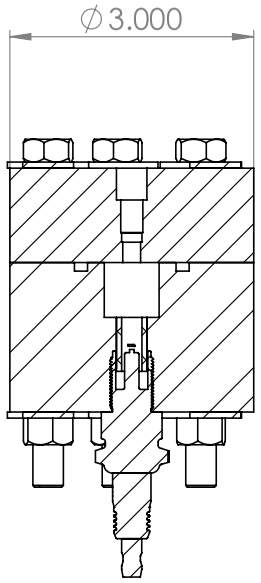

SECTION A-A

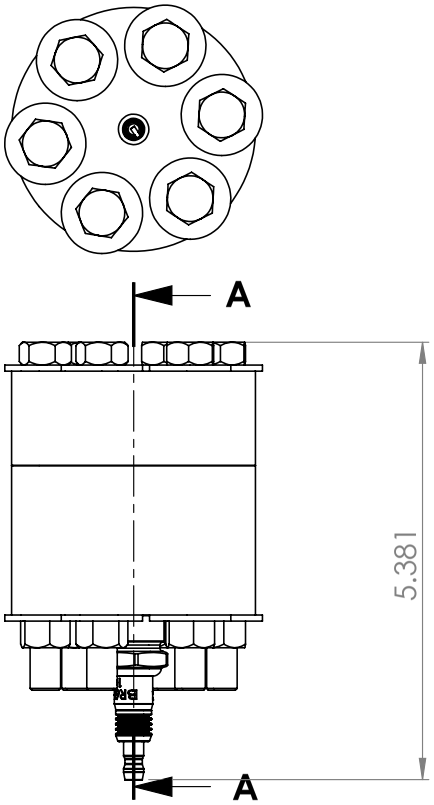

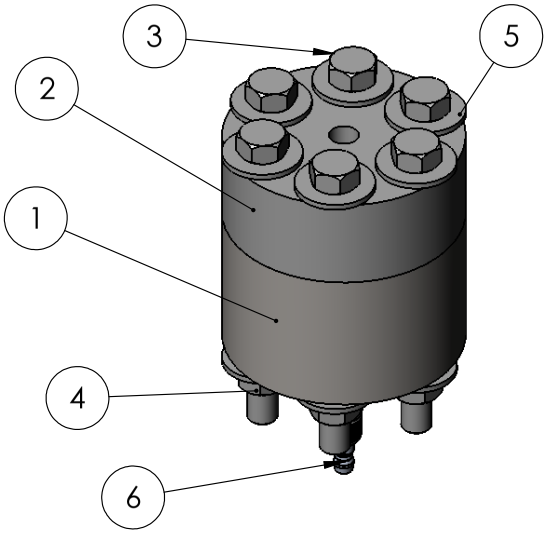

ITEM NO.	PART NUMBER	QTY.
1	Main Body	1
2	Head	1
3	3/8" x 5" Bolt	6
4	3/8" Nut	6
5	Washer	12
6	Spark Plug	1
7	Plastic Rod	1

UNLESS OTHERWISE SPECIFIED:

DIMENSIONS ARE IN INCHES
TOLERANCES:
FRACTIONAL ± 1/64
ANGULAR: MACH ± BEND ±
ONE PLACE DECIMAL ± 0.010
TWO PLACE DECIMAL ± 0.005
THREE PLACE DECIMAL ± 0.002

REVISION

DEBUR AND BREAK SHARP EDGES

	NAME	SIGNATURE	DATE
DRAWN	G. Maines		27/08/12
CHK'D			
APPV'D			
MFG			
Q.A			

DO NOT SCALE DRAWING

MATERIAL: ALUMINUM Alloy 6061-T6

WEIGHT:

University of Ottawa
Faculty of Engineering

TITLE:

Miniature Pressure Cell

DWG NO. PC100

A4

SCALE:1:2

SHEET 1 OF 4

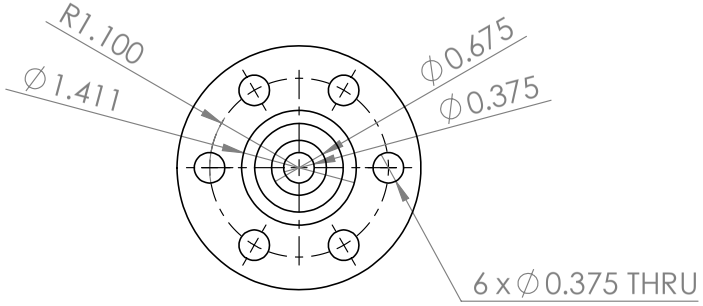

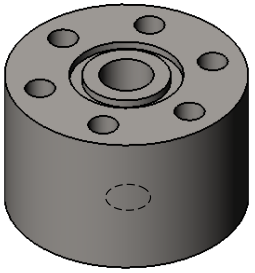

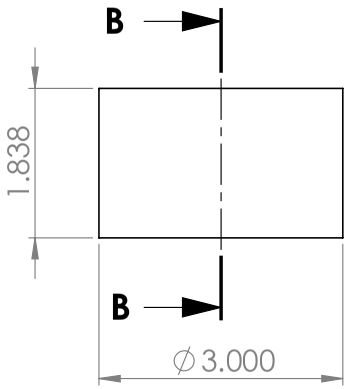

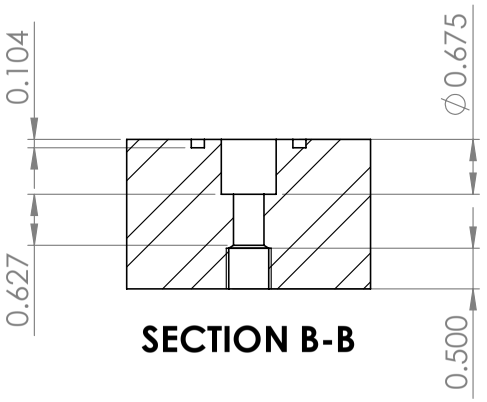

SECTION B-B

Quantity Required: 1

UNLESS OTHERWISE SPECIFIED: DIMENSIONS ARE IN INCHES TOLERANCES: FRACTIONAL ± 1/64 ANGULAR: MACH ± BEND ± ONE PLACE DECIMAL ± 0.010 TWO PLACE DECIMAL ± 0.005 THREE PLACE DECIMAL ± 0.002			REVISION			DEBUR AND BREAK SHARP EDGES
	NAME	SIGNATURE	DATE			
DRAWN	G. Maines		27/08/12			
CHK'D			DO NOT SCALE DRAWING			
APPV'D			MATERIAL: ALUMINUM Alloy 6061-T6			
MFG						
Q.A						
			WEIGHT:			

University of Ottawa
Faculty of Engineering

TITLE:

Body

DWG NO. PC101

A4

SCALE:1:2

SHEET 2 OF 4

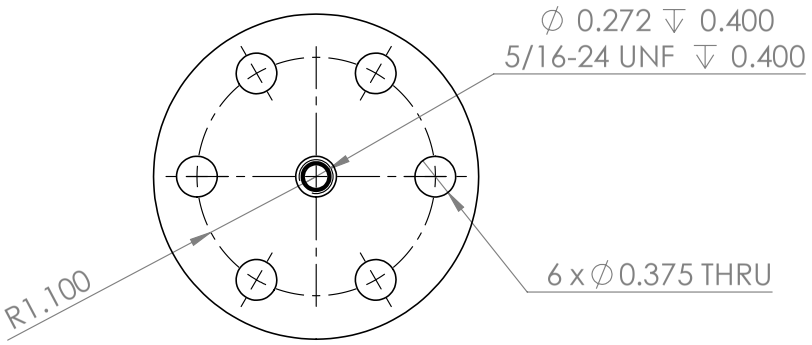

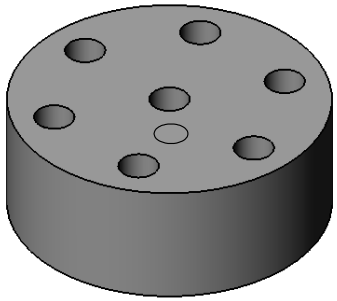

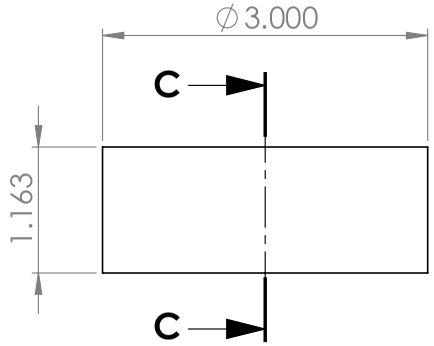

SECTION C-C

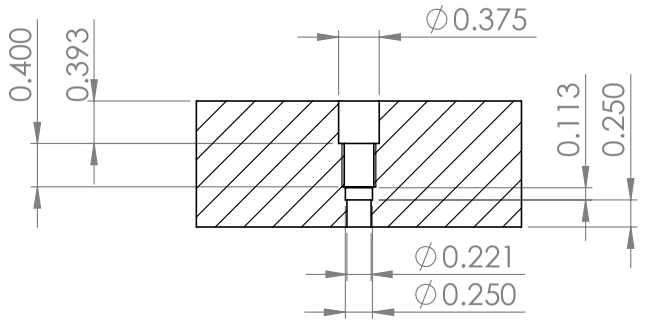

Quantity Required: 1

UNLESS OTHERWISE SPECIFIED: DIMENSIONS ARE IN INCHES TOLERANCES: FRACTIONAL ± 1/64 ANGULAR: MACH ± BEND ± ONE PLACE DECIMAL ± 0.010 TWO PLACE DECIMAL ± 0.005 THREE PLACE DECIMAL ± 0.002			REVISION			DEBUR AND BREAK SHARP EDGES
	NAME	SIGNATURE	DATE			
DRAWN	G. Maines		27/08/12			
CHK'D			DO NOT SCALE DRAWING			
APPV'D			MATERIAL: ALUMINUM Alloy 6061-T6			
MFG						
Q.A						
			WEIGHT:			

University of Ottawa
Faculty of Engineering

TITLE:

Head

DWG NO. PC102

A4

SCALE:2:3

SHEET 3 OF 4

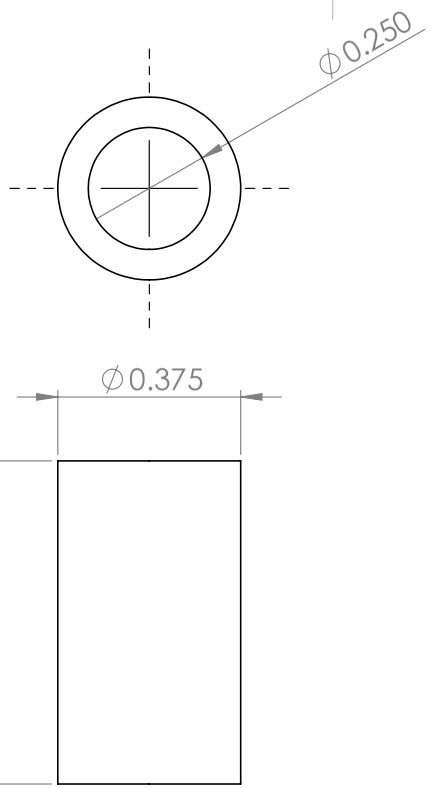

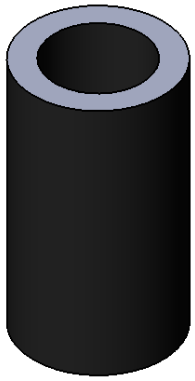

Quantity Required: 1

UNLESS OTHERWISE SPECIFIED: DIMENSIONS ARE IN INCHES TOLERANCES: FRACTIONAL ± 1/64 ANGULAR: MACH ± BEND ± ONE PLACE DECIMAL ± 0.010 TWO PLACE DECIMAL ± 0.005 THREE PLACE DECIMAL ± 0.002			REVISION			DEBUR AND BREAK SHARP EDGES
	NAME	SIGNATURE	DATE			
DRAWN	G. Maines		27/08/12			
CHK'D			DO NOT SCALE DRAWING			
APPV'D			MATERIAL: ALUMINUM Alloy 6061-T6			
MFG						
Q.A						
			WEIGHT:			

University of Ottawa
Faculty of Engineering

TITLE:

Sleeve

DWG NO. PC103

A4

SCALE:3:1

SHEET 4 OF 4

Appendix E

Design drawings for the 1.06 L combustion chamber

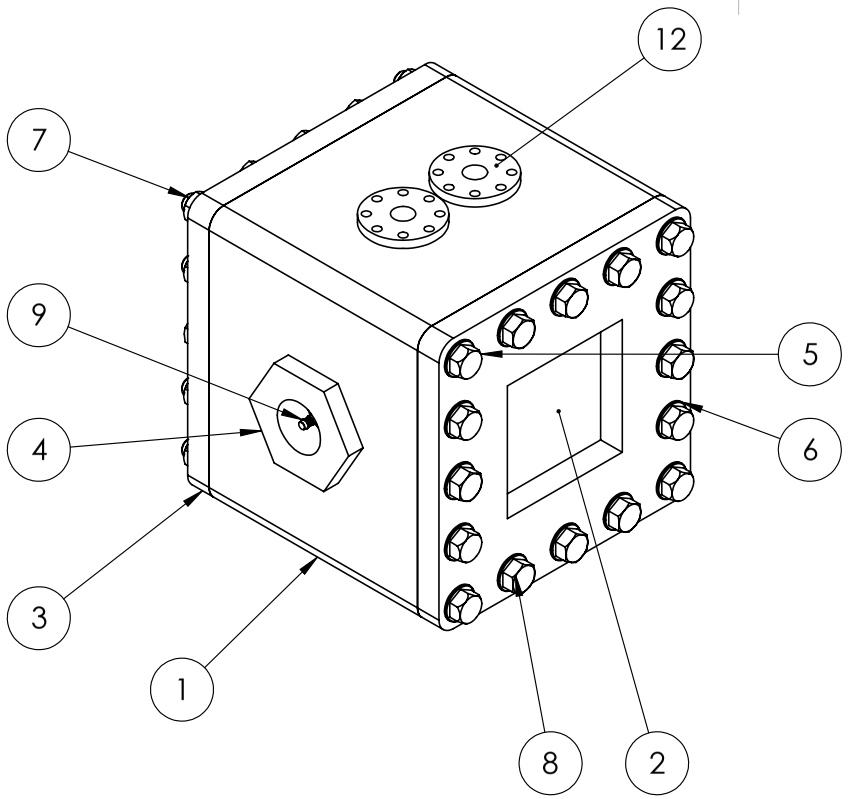

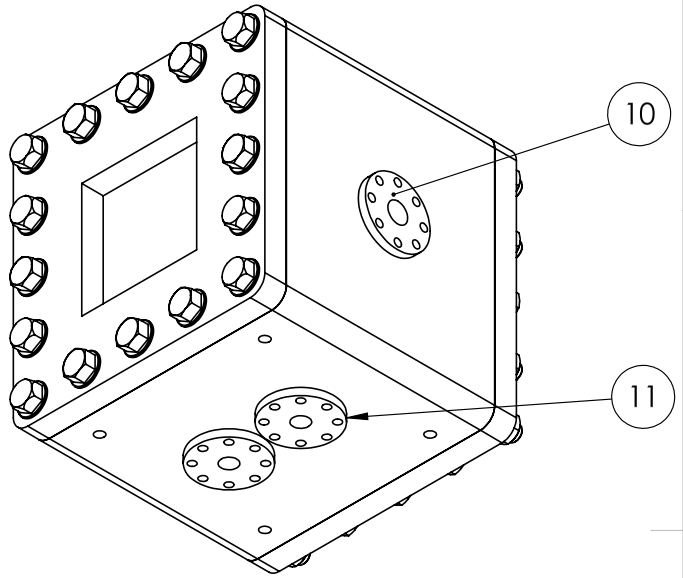

ITEM NO.	PART NUMBER	QTY.
1	MainBody	1
2	Al6061_Window	2
3	EndPlate	2
4	IgniterPlug	1
5	HBOLT 0.5000-20x9.5x9.5-N	8
6	Washer	32
7	HNUT 0.5000-20-D-C	8
8	HBOLT 0.5000-20x2.5x2.5-N	16
9	SparkPlug	1
10	NeptunePlug2	1
11	PCBPlug_Solid	2
12	PCBPlug	2

Contact: Geoff Maines
Department: MCG
Office: CBY B210 Desk 21
E-mail: gmaines@uottawa.ca
Tel.: 613-709-5398 (cell)

UNLESS OTHERWISE SPECIFIED:
DIMENSIONS ARE IN INCHES
TOLERANCES:
FRACTIONAL ± 1/64
ANGULAR: MACH ± BEND ±
ONE PLACE DECIMAL ± 0.010
TWO PLACE DECIMAL ± 0.005
THREE PLACE DECIMAL ± 0.002

REVISION

DEBUR AND BREAK SHARP EDGES

	NAME	SIGNATURE	DATE
DRAWN	G. Maines		27/08/12
CHK'D			
APPV'D			
MFG			
Q.A			

DO NOT SCALE DRAWING

MATERIAL: ALUMINUM Alloy 6061-T6

WEIGHT:

University of Ottawa
Faculty of Engineering

TITLE:

Blast Chamber Assembly

DWG NO. BC100

A4

SCALE:1:4

SHEET 1 OF 13

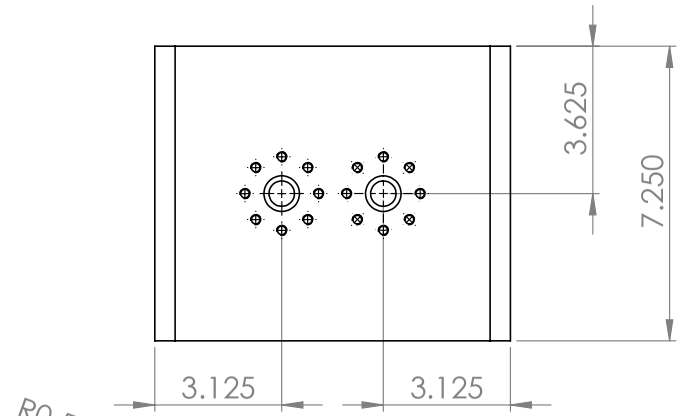

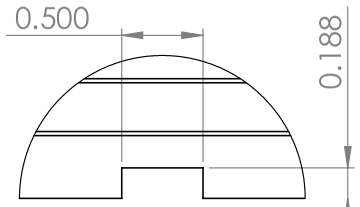

DETAIL A
SCALE 1 : 1

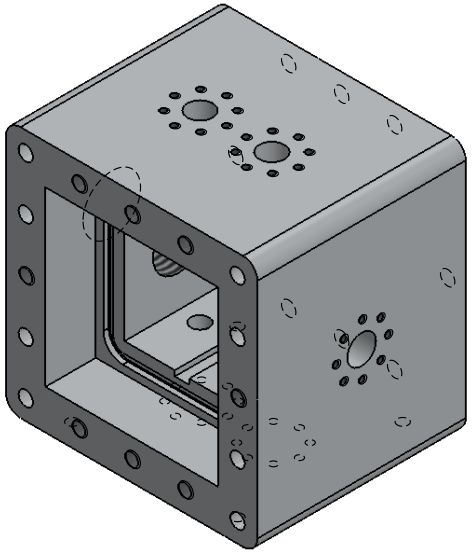

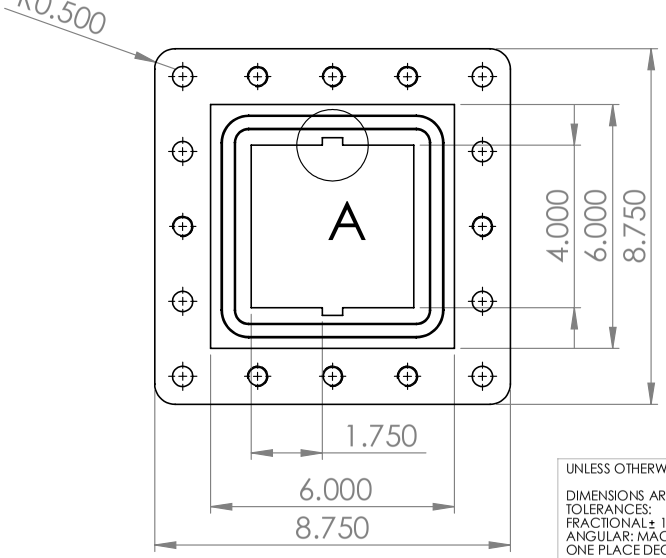

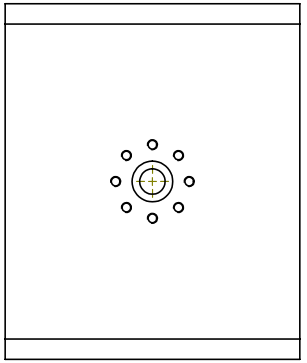

Quantity Required: 1

UNLESS OTHERWISE SPECIFIED: DIMENSIONS ARE IN INCHES TOLERANCES: FRACTIONAL ± 1/64 ANGULAR: MACH ± BEND ± ONE PLACE DECIMAL ± 0.010 TWO PLACE DECIMAL ± 0.005 THREE PLACE DECIMAL ± 0.002		REVISION		DEBUR AND BREAK SHARP EDGES	**University of Ottawa** Faculty of Engineering
	NAME	SIGNATURE	DATE		TITLE: Main Body (Overall Dimensions)
DRAWN	G. Maines		27/08/12		
CHK'D			DO NOT SCALE DRAWING		
APPV'D			MATERIAL: ALUMINUM Alloy 6061-T6		DWG NO. BC101-1 A4
MFG					
Q.A			WEIGHT:	SCALE:1:4	SHEET 2 OF 13

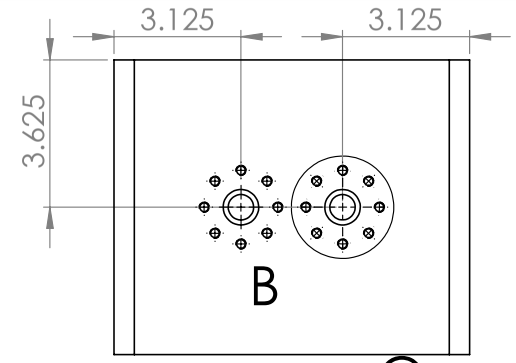

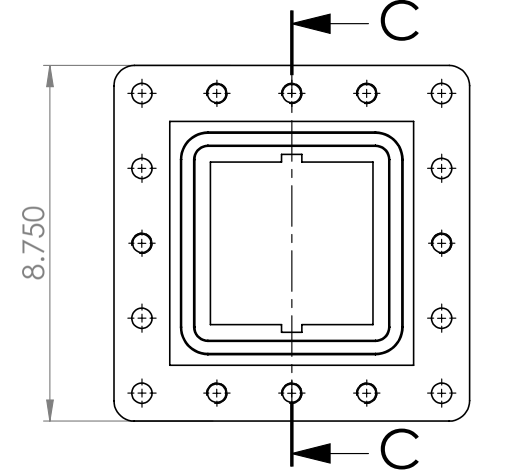

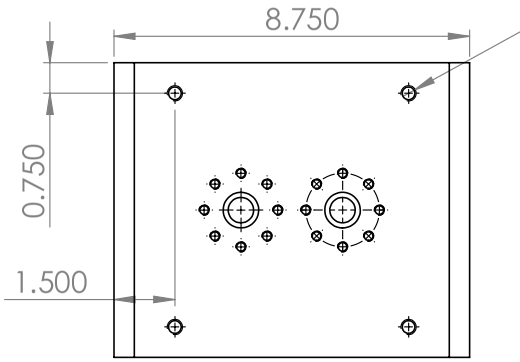

4 x ∅ 0.313 ↧ 0.940
3/8-16 UNC - 1B ↧ 0.750

DETAIL B
SCALE 1 : 2

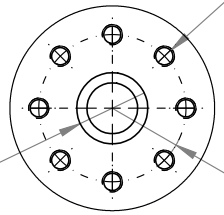

8 x ∅ 0.213 ↧ 0.860
1/4-28 UNF - 1B ↧ 0.750

∅0.625 THRU
H7 +0.001
⌴ ∅0.875 0.000↧1.063

R0.905

SECTION C-C

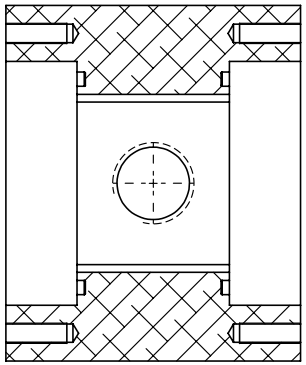

UNLESS OTHERWISE SPECIFIED: DIMENSIONS ARE IN INCHES TOLERANCES: FRACTIONAL± 1/64 ANGULAR: MACH± BEND ± ONE PLACE DECIMAL ± 0.010 TWO PLACE DECIMAL ± 0.005 THREE PLACE DECIMAL ± 0.002			REVISION			DEBUR AND BREAK SHARP EDGES
	NAME	SIGNATURE	DATE			
DRAWN	G. Maines		27/08/12			
CHK'D			DO NOT SCALE DRAWING			
APPV'D			MATERIAL: ALUMINUM Alloy 6061-T6			
MFG						
Q.A						
			WEIGHT:			

University of Ottawa
Faculty of Engineering

TITLE:

Main Body (Top/Bottom)

DWG NO. BC101-2

A4

SCALE:1:4 SHEET 3 OF 13

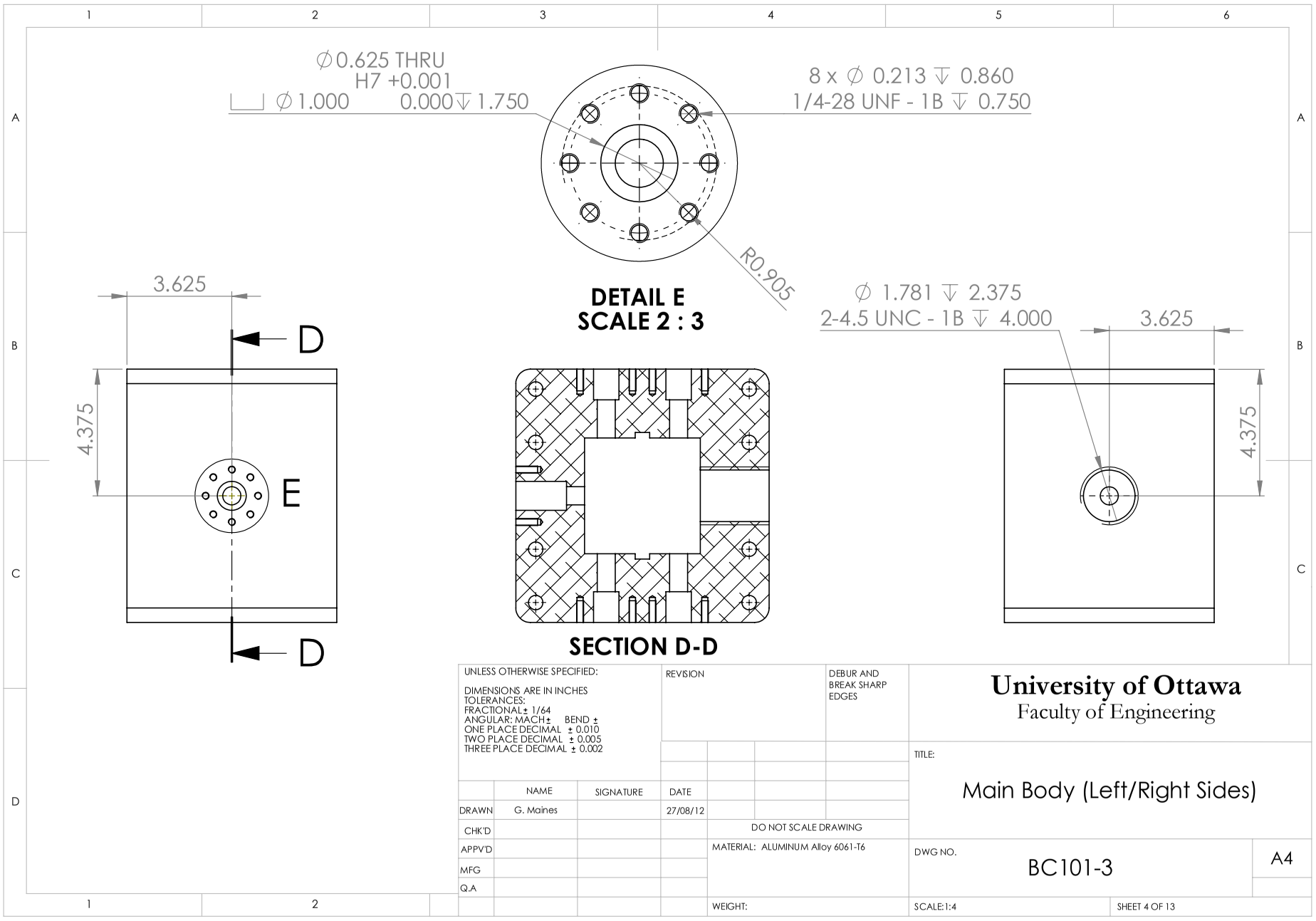

UNLESS OTHERWISE SPECIFIED: DIMENSIONS ARE IN INCHES TOLERANCES: FRACTIONAL± 1/64 ANGULAR: MACH± BEND ± ONE PLACE DECIMAL ± 0.010 TWO PLACE DECIMAL ± 0.005 THREE PLACE DECIMAL ± 0.002			REVISION		DEBUR AND BREAK SHARP EDGES	**University of Ottawa** Faculty of Engineering
						TITLE: Main Body (Left/Right Sides)
	NAME	SIGNATURE	DATE			
DRAWN	G. Maines		27/08/12			
CHK'D			DO NOT SCALE DRAWING			
APPV'D			MATERIAL: ALUMINUM Alloy 6061-T6			DWG NO. BC101-3 A4
MFG						
Q.A						
			WEIGHT:			SCALE:1:4 SHEET 4 OF 13

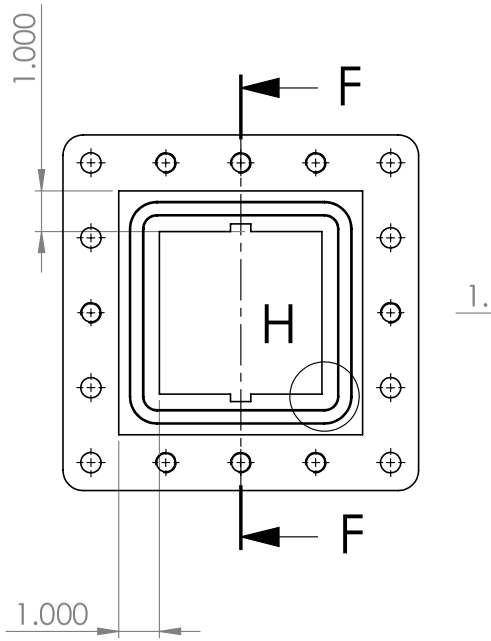

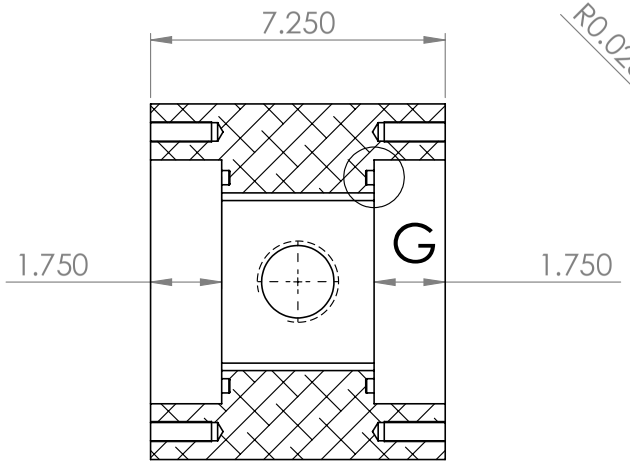

SECTION F-F

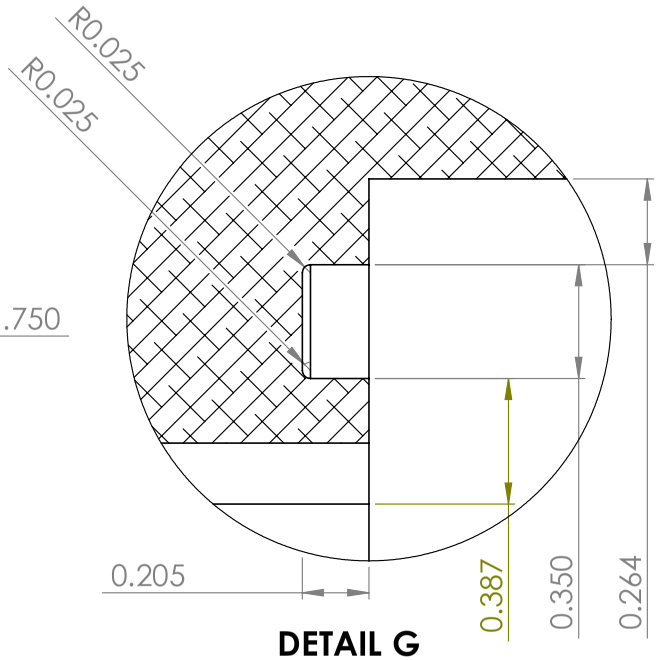

DETAIL G
SCALE 2 : 1
(O-Ring Gland)

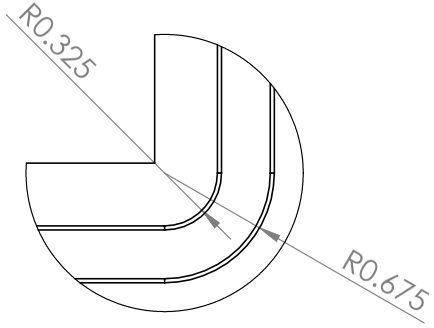

DETAIL H
SCALE 1 : 1
(O-Ring Gland)

UNLESS OTHERWISE SPECIFIED:

DIMENSIONS ARE IN INCHES
TOLERANCES:
FRACTIONAL ± 1/64
ANGULAR: MACH ± BEND ±
ONE PLACE DECIMAL ± 0.010
TWO PLACE DECIMAL ± 0.005
THREE PLACE DECIMAL ± 0.002

REVISION

DEBUR AND BREAK SHARP EDGES

	NAME	SIGNATURE	DATE
DRAWN	G. Maines		27/08/12
CHK'D			
APPV'D			
MFG			
Q.A			

DO NOT SCALE DRAWING

MATERIAL: ALUMINUM Alloy 6061-T6

WEIGHT:

University of Ottawa
Faculty of Engineering

TITLE:

Main Body
(Window Slot and O-Ring Gland)

DWG NO. BC101-4

A4

SCALE:1:4

SHEET 5 OF 13

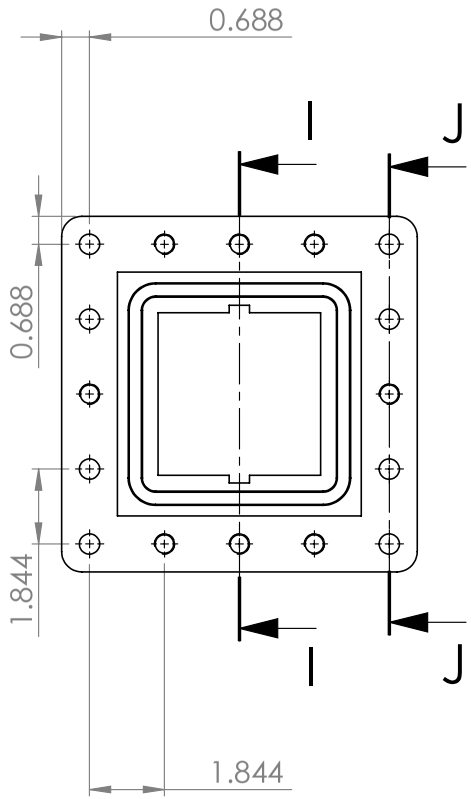

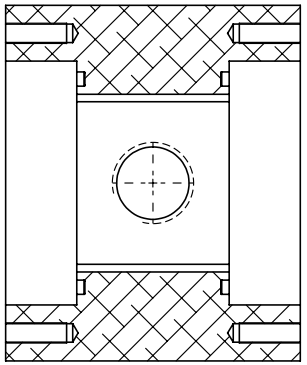

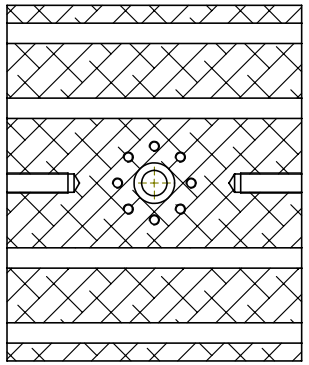

SECTION I-I **SECTION J-J**

Thread Callout

UNLESS OTHERWISE SPECIFIED:

DIMENSIONS ARE IN INCHES
TOLERANCES:
FRACTIONAL ± 1/64
ANGULAR: MACH ± BEND ±
ONE PLACE DECIMAL ± 0.010
TWO PLACE DECIMAL ± 0.005
THREE PLACE DECIMAL ± 0.002

REVISION

DEBUR AND BREAK SHARP EDGES

	NAME	SIGNATURE	DATE
DRAWN	G. Maines		27/08/12
CHK'D			
APPV'D			
MFG			
Q.A			

DO NOT SCALE DRAWING

MATERIAL: ALUMINUM Alloy 6061-T6

WEIGHT:

University of Ottawa
Faculty of Engineering

TITLE:

Main Body (Main Screws/Bolts)

DWG NO. BC101-5

A4

SCALE:1:4

SHEET 6 OF 13

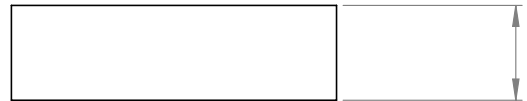

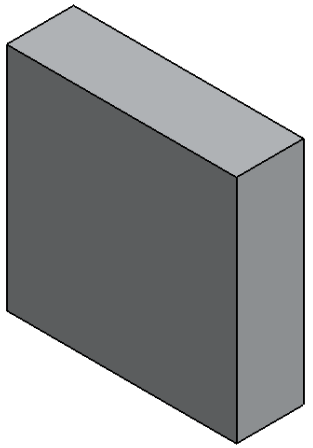

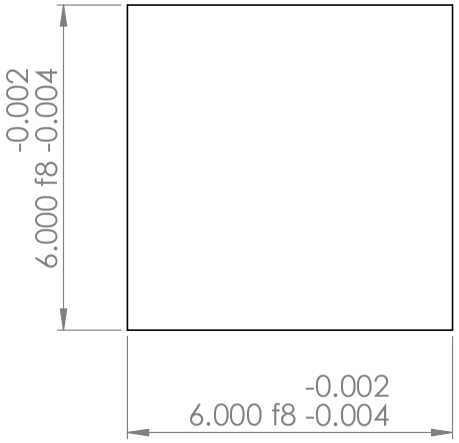

Quantity Required: 2

UNLESS OTHERWISE SPECIFIED: DIMENSIONS ARE IN INCHES TOLERANCES: FRACTIONAL ± 1/64 ANGULAR: MACH ± BEND ± ONE PLACE DECIMAL ± 0.010 TWO PLACE DECIMAL ± 0.005 THREE PLACE DECIMAL ± 0.002			REVISION			DEBUR AND BREAK SHARP EDGES
	NAME	SIGNATURE	DATE			
DRAWN	G. Maines		27/08/12			
CHK'D			DO NOT SCALE DRAWING			
APPV'D			MATERIAL: ALUMINUM Alloy 6061-T6			
MFG						
Q.A						
			WEIGHT:			

University of Ottawa
Faculty of Engineering

TITLE:

Window

DWG NO. BC102

A4

SCALE:1:3

SHEET 7 OF 13

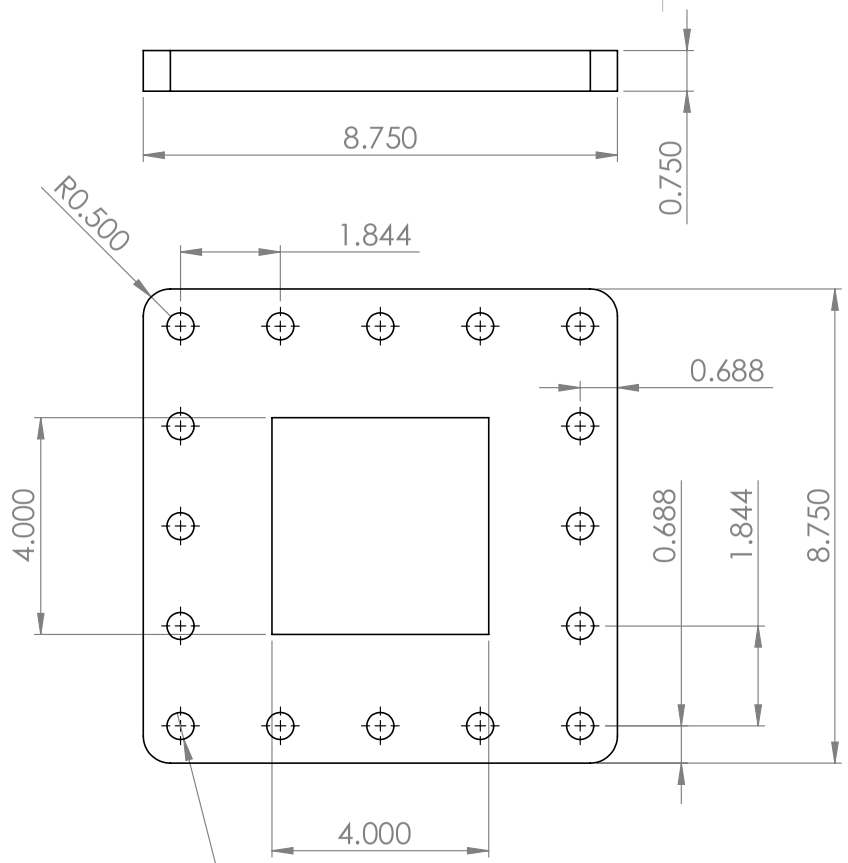

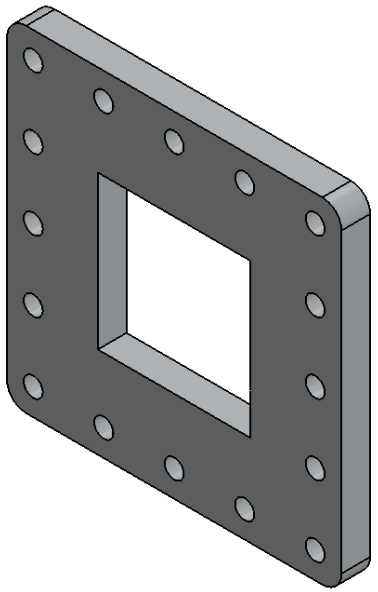

16 x ⌀0.500 H8 +0.001 0.000 THRU

Quantity Required: 2

UNLESS OTHERWISE SPECIFIED: DIMENSIONS ARE IN INCHES TOLERANCES: FRACTIONAL ± 1/64 ANGULAR: MACH ± BEND ± ONE PLACE DECIMAL ± 0.010 TWO PLACE DECIMAL ± 0.005 THREE PLACE DECIMAL ± 0.002			REVISION			DEBUR AND BREAK SHARP EDGES
	NAME	SIGNATURE	DATE			
DRAWN	G. Maines		27/08/12			
CHK'D			DO NOT SCALE DRAWING			
APPV'D			MATERIAL: ALUMINUM Alloy 6061-T6			
MFG						
Q.A						
			WEIGHT:			

University of Ottawa
Faculty of Engineering

TITLE:

Window Frame

DWG NO. BC103

A4

SCALE:1:3 SHEET 8 OF 13

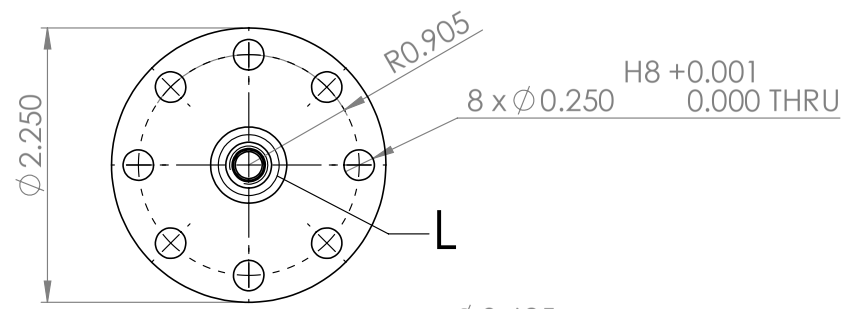

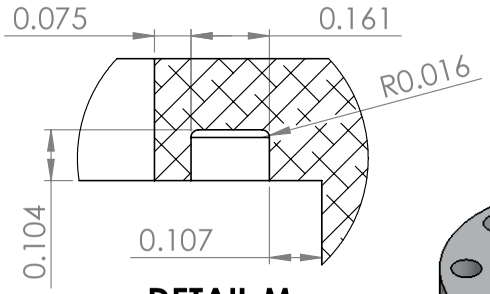

DETAIL M
SCALE 3 : 1
(O-Ring Gland)

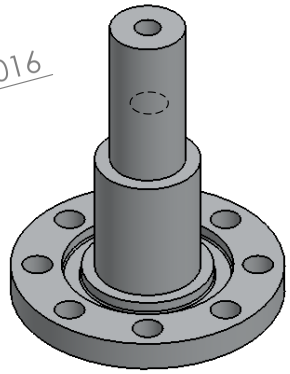

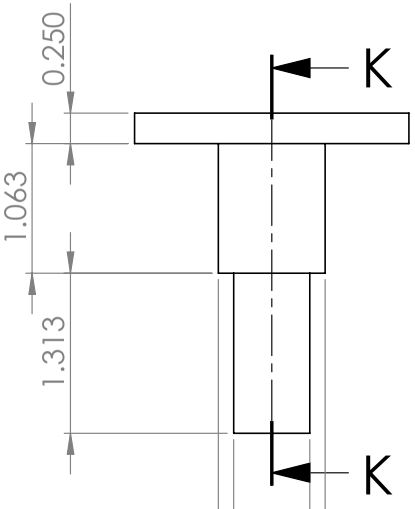

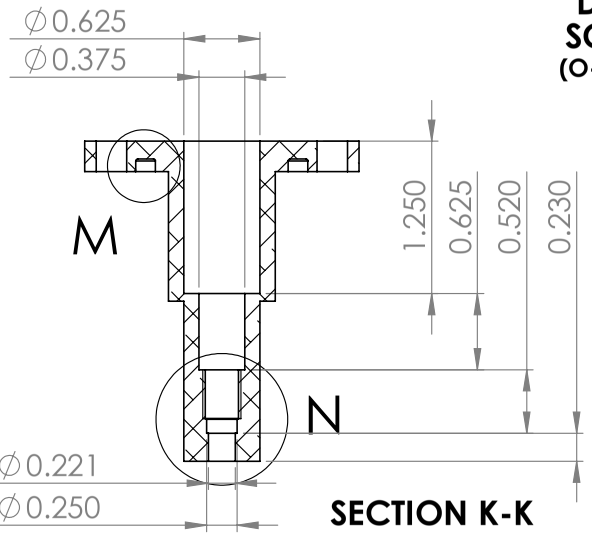

SECTION K-K

∅ 0.272 ↧ 0.400
5/16-24 UNF - 1B ↧ 0.400

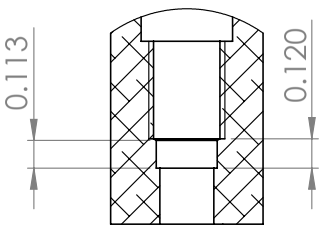

DETAIL N
SCALE 6 : 4

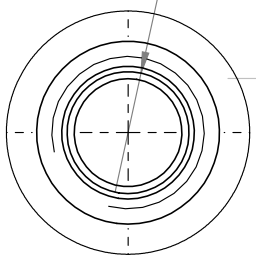

DETAIL L
SCALE 3 : 1

-0.000
∅0.625 g6 -0.001

-0.000
∅0.875 g6 -0.001

Quantity Required: 2

UNLESS OTHERWISE SPECIFIED:

DIMENSIONS ARE IN INCHES
TOLERANCES:
FRACTIONAL ± 1/64
ANGULAR: MACH ± BEND ±
ONE PLACE DECIMAL ± 0.010
TWO PLACE DECIMAL ± 0.005
THREE PLACE DECIMAL ± 0.002

REVISION

DEBUR AND BREAK SHARP EDGES

	NAME	SIGNATURE	DATE
DRAWN	G. Maines		27/08/12
CHK'D			
APPV'D			
MFG			
Q.A			

DO NOT SCALE DRAWING

MATERIAL: ALUMINUM Alloy 6061-T6

WEIGHT:

University of Ottawa
Faculty of Engineering

TITLE:

PCB Plug

DWG NO. BC104

A4

SCALE:3:4

SHEET 9 OF 13

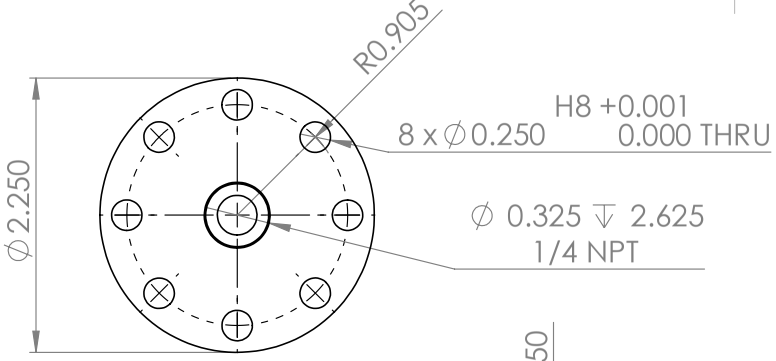

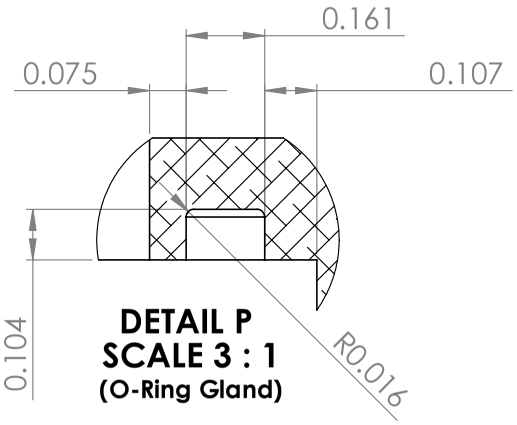

DETAIL P
SCALE 3 : 1
(O-Ring Gland)

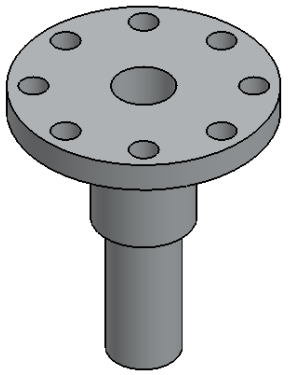

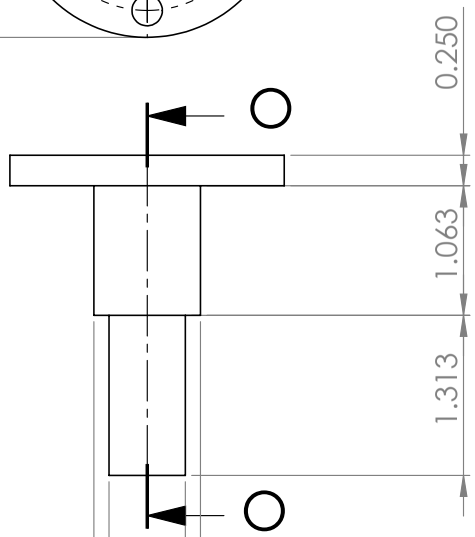

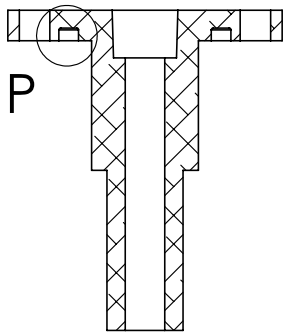

SECTION O-O

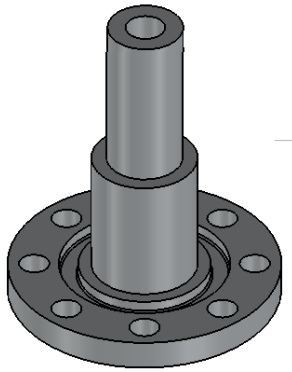

-0.000
⌀0.625 g6 -0.001

-0.000
⌀0.875 g6 -0.001

Quantity Required: 2

UNLESS OTHERWISE SPECIFIED:			REVISION		DEBUR AND BREAK SHARP EDGES
DIMENSIONS ARE IN INCHES TOLERANCES: FRACTIONAL± 1/64 ANGULAR: MACH± BEND ± ONE PLACE DECIMAL ± 0.010 TWO PLACE DECIMAL ± 0.005 THREE PLACE DECIMAL ± 0.002					
	NAME	SIGNATURE	DATE		
DRAWN	G. Maines		27/08/12		
CHK'D			DO NOT SCALE DRAWING		
APPV'D			MATERIAL: ALUMINUM Alloy 6061-T6		
MFG					
Q.A					
			WEIGHT:		

University of Ottawa
Faculty of Engineering

TITLE:

PCB Plug (Solid Version)

DWG NO. BC105

A4

SCALE:3:4 SHEET 10 OF 13

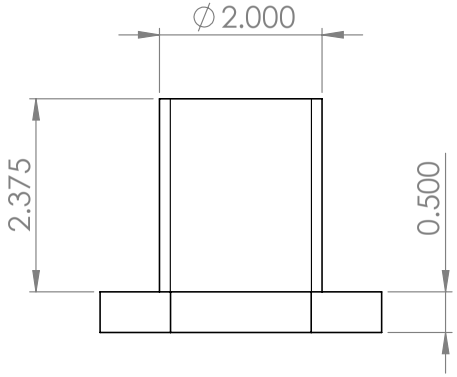

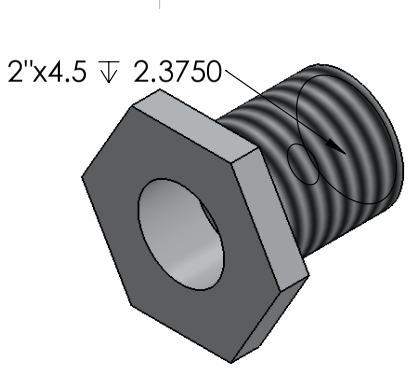

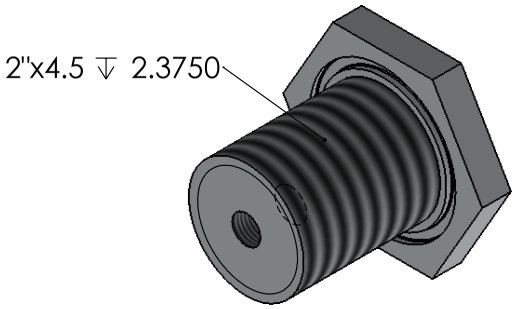

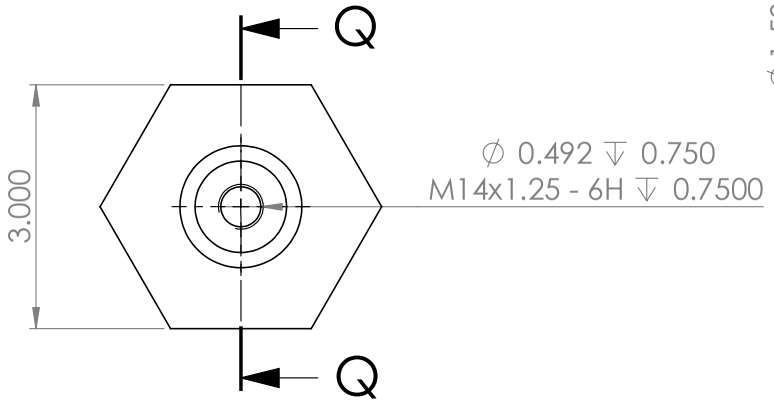

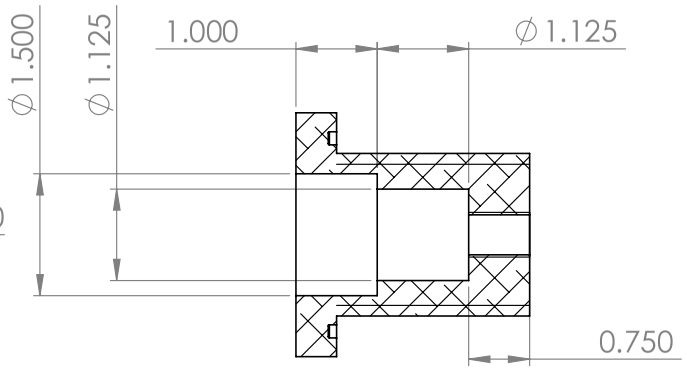

SECTION Q-Q

Quantity Required: 1

UNLESS OTHERWISE SPECIFIED: DIMENSIONS ARE IN INCHES TOLERANCES: FRACTIONAL± 1/64 ANGULAR: MACH± BEND ± ONE PLACE DECIMAL ± 0.010 TWO PLACE DECIMAL ± 0.005 THREE PLACE DECIMAL ± 0.002			REVISION			DEBUR AND BREAK SHARP EDGES
	NAME	SIGNATURE	DATE			
DRAWN	G. Maines		27/08/12			
CHK'D			DO NOT SCALE DRAWING			
APPV'D			MATERIAL: ALUMINUM Alloy 6061-T6			
MFG						
Q.A						
			WEIGHT:			

University of Ottawa
Faculty of Engineering

TITLE:

Igniter Plug

DWG NO. BC106

A4

SCALE:1:2

SHEET 11 OF 13

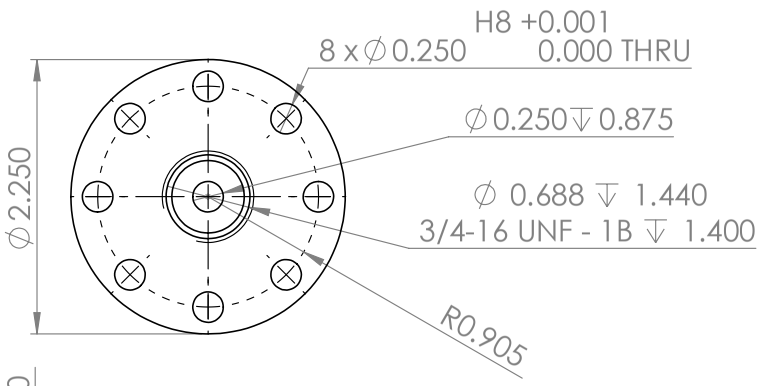

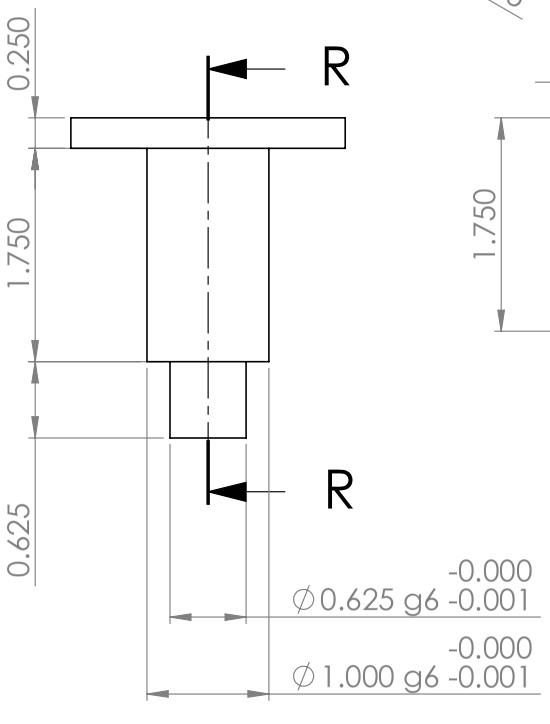

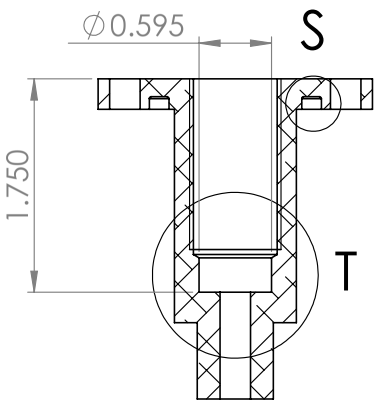

SECTION R-R

DETAIL S
SCALE 3 : 1
(O-Ring Gland)

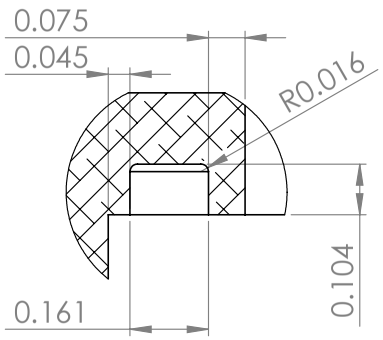

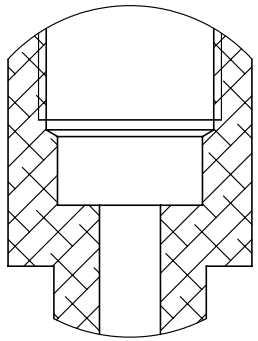

DETAIL T
SCALE 6 : 4

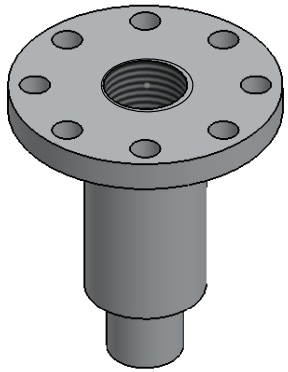

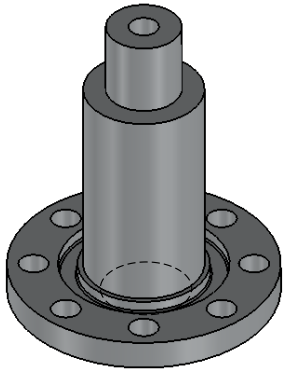

-0.000
∅0.625 g6 -0.001
-0.000
∅1.000 g6 -0.001

Quantity Required: 1

UNLESS OTHERWISE SPECIFIED:
DIMENSIONS ARE IN INCHES
TOLERANCES:
FRACTIONAL± 1/64
ANGULAR: MACH± BEND ±
ONE PLACE DECIMAL ± 0.010
TWO PLACE DECIMAL ± 0.005
THREE PLACE DECIMAL ± 0.002

REVISION

DEBUR AND BREAK SHARP EDGES

	NAME	SIGNATURE	DATE
DRAWN	G. Maines		27/08/12
CHK'D			
APPV'D			
MFG			
Q.A			

DO NOT SCALE DRAWING

MATERIAL: ALUMINUM Alloy 6061-T6

WEIGHT:

University of Ottawa
Faculty of Engineering

TITLE:

Neptune Plug

DWG NO. BC107

A4

SCALE:3:4

SHEET 12 OF 13

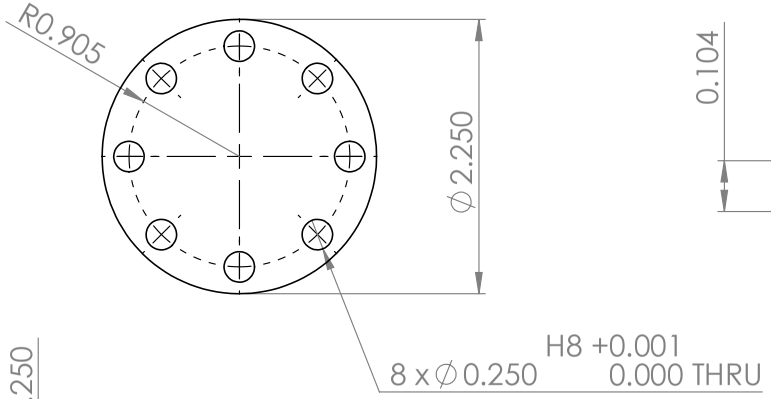

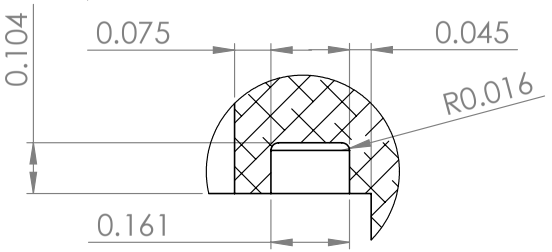

DETAIL V
SCALE 3 : 1
(O-Ring Gland)

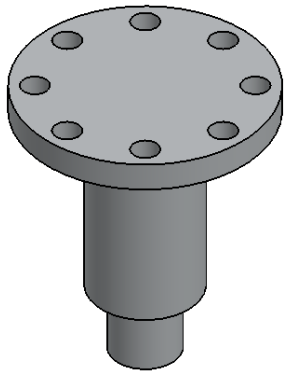

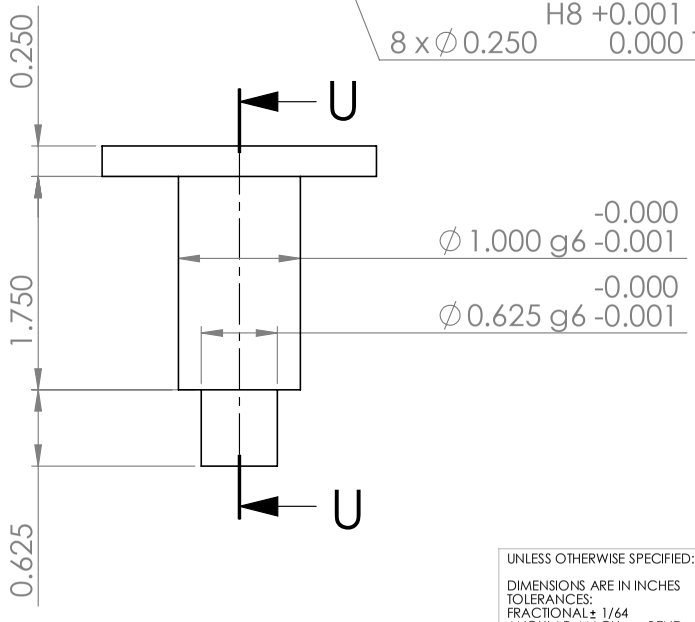

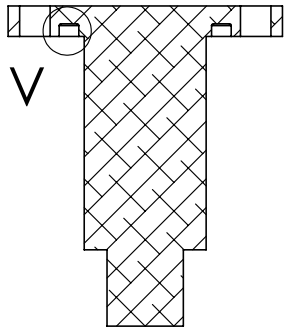

SECTION U-U

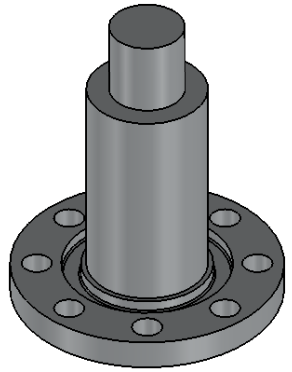

Quantity Required: 1

UNLESS OTHERWISE SPECIFIED: DIMENSIONS ARE IN INCHES TOLERANCES: FRACTIONAL± 1/64 ANGULAR: MACH± BEND ± ONE PLACE DECIMAL ± 0.010 TWO PLACE DECIMAL ± 0.005 THREE PLACE DECIMAL ± 0.002			REVISION		DEBUR AND BREAK SHARP EDGES
	NAME	SIGNATURE	DATE		
DRAWN	G. Maines		27/08/12		
CHK'D			DO NOT SCALE DRAWING		
APPV'D			MATERIAL: ALUMINUM Alloy 6061-T6		
MFG					
Q.A					
			WEIGHT:	SCALE:3:4	SHEET 13 OF 13

University of Ottawa
Faculty of Engineering

TITLE:

Neptune Plug (Solid Version)

DWG NO. BC108

A4

Appendix F

Python scripts

F.1 CEA Calculations: Al-MoO_3 constant-pressure

```
#############################################################################
# Script to calculate, run and tabulate constant-pressure calculations
# for Al-MoO3 using NASA's CEA
# G. Maines , 2013

import os
def inList(a, x):                          # List-check Function
    for item in a:
        if x==item:
            return True
    return False

data = open('./data.csv', 'w') # Thermodynamic and Species Data
ceainp = open('./ceafile.inp', 'w') # CEA Input File

#~~~~~~~~~~~~~~~~~~~~ Material parameters ~~~~~~~~~~~~~~~~~~~~#
rAl=2700.0 # Density of Aluminum (kg/m^3)
rMoO3=4690.0 # Density of MoO3 (kg/m^3)
rAir=1.2 # Density of Air (kg/m^3)
WAl=26.98 # Molar Mass of Aluminum (g/mol)
WMoO3=143.94 # Molar Mass of MoO3 (g/mol)
WAir=28.97 # Molar Mass of Air (g/mol)
WAL2O3=101.96 # Molar Mass of AL2O3 (g/mol)

#~~~~~~~~~~~~~~~~~~~~~~~ Stoichiometry ~~~~~~~~~~~~~~~~~~~~~~~#
NMoO3=1
phi=0.42

#~~~~~~~~~~~~~~~~~~~~~~~ Set up array ~~~~~~~~~~~~~~~~~~~~~~~#
experiment=[]
experiment.append(['phi','P','T','R','GAMMAs'])

#~~~~~~~~~~~~~~~~~~~ TMD loop calculations ~~~~~~~~~~~~~~~~~~~#
while phi<1.42:
    experiment.append([])
    NAl=(2.0/1.0)*phi*NMoO3 # Calculate moles of Al based on equivalence ratio

    #~~~~~~~~~~~~ Calculations based on stoichiometry ~~~~~~~~~~~~#
    cAl=(NAl*WAl)/(NAl*WAl+NMoO3*WMoO3) # Mass fraction of Al
    cMoO3=(NMoO3*WMoO3)/(NAl*WAl+NMoO3*WMoO3) # Mass fraction of MoO3
    rTMD=1.0/(cAl/rAl+cMoO3/rMoO3) # Theoretical Max. Density (TMD, kg/m3)
    TMD=6 # Set TMD for all experiments

    #~~~~~~~~~~~~~~~ Calculations based on TMD ~~~~~~~~~~~~~~~#
    rmix=(TMD/100.0)*rTMD    # Mixture density
    NAir=(rAir/WAir)*((NAl*WAl+NMoO3*WMoO3)/(rmix)-(NAl*WAl/(rAl))-(NMoO3*WMoO3/(rMoO3))
        ) # Number of moles of air (mol)
    reff=rmix + rAir*(100.0-TMD)/100.0 # Effective total mixture density, including air
        (kg/m^3)

    # Fix NAl and NAL2O3 (based on Dutro 2009 paper)
```

```
50      NAL2O3=NAl/(1+(0.81/0.19)*(WAL2O3/WAl))
51      NAl=NAl-NAL2O3
52
53      #~~~~~~~~~~~~~~~~~ Write CEA input file ~~~~~~~~~~~~~~~~~#
54      ceainp.write('reac name AL(cr) moles='+str(NAl)+' t(k)=298.15' + '\n' \
55      '      name MoO3(cr) moles='+str(NMoO3)+' t(k)=298.15' + '\n' \
56      '      name AL2O3(a) moles='+str(NAL2O3)+' t(k)=298.15' + '\n' \
57      '      name Air moles='+str(NAir)+' t(k)=298.15' + '\n\n' \
58      'prob case=phi'+str(phi)+' hp rho,kg/m^3='+str(reff) + '\n' \
59      'insert AL2O3(a)' + '\n' \
60      'output siunits' + '\n' \
61      'end' + '\n\n')
62
63      experiment[len(experiment)-1].append(phi)
64      phi=phi + 0.05
65  ceainp.close()
66
67  #~~~~~~~~~~~~~~~~~~~~~ Run CEA script ~~~~~~~~~~~~~~~~~~~~~~#
68  os.system('echo ceafile | ./CEA.out')
69
70  #~~~~~~~~~~~~~~~~~~ Open CEA output file ~~~~~~~~~~~~~~~~~~~#
71  ceaout = open('ceafile.out', 'r')
72
73  #~~~~~~~~~~~~~~~~~~~~~ Search for data ~~~~~~~~~~~~~~~~~~~~~#
74  doc=ceaout.readlines()
75  linecount=1
76  for i in range(0,len(doc)):
77      line=doc[i]
78      # Look for and add pressures to experiment array in rows
79      if 'P, BAR' in line:
80          for c in line:
81              if c in ['0','1','2','3','4','5','6','7','8','9']:
82                  experiment[linecount].append(float(line[line.index(c):len(line)])/10) #
                        Divide by 10 to convert to MPa
83                  break
84      # Look for and add temperatures to experiment array in rows
85      if 'T, K' in line:
86          for c in line:
87              if c in ['0','1','2','3','4','5','6','7','8','9']:
88                  experiment[linecount].append(float(line[line.index(c):len(line)]))
89                  break
90      # Look for and add densities to experiment array in rows
91      if 'RHO, KG/CU M' in line:
92          for c in line:
93              if c in ['0','1','2','3','4','5','6','7','8','9']:
94                  experiment[linecount].append(line[line.index(c):len(line)-1])
95                  break
96      # Look for and add isentropic exponents to new data file
97      if 'GAMMAs' in line:
98          for c in line:
99              if c in ['0','1','2','3','4','5','6','7','8','9']:
100                 experiment[linecount].append(line[line.index(c):len(line)-1])
101                 break
```

```
102     # Look for mole fractions, and add the name of each species to row 0, if it does not
            yet exist to experiment array
103     if 'MOLE FRACTIONS' in line and len(line) < 20:
104         j=2
105         newline=doc[i+j]
106         while True:
107             if len(newline)==1:
108                 break
109             newline=doc[i+j]
110             for c in newline:
111                 if c in ['0','1','2','3','4','5','6','7','8','9'] and newline[newline.
                        index(c)-1] == ' ':
112                     if not inList(experiment[0],newline[0:newline.index(c)].strip()):
113                         experiment[0].append(newline[0:newline.index(c)].strip())
114             j +=1
115         linecount +=1
116
117 #~~~~~~~~~~~~~~~~~ Append zeroes everywhere ~~~~~~~~~~~~~~~~~~#
118 for k in range(1,len(experiment)):
119     while len(experiment[k])<len(experiment[0]):
120         experiment[k].append('0')
121
122 #~~~ Add mole fractions to appropriate column for each phi ~~~#
123 linecount=1
124 for i in range(0,len(doc)):
125     line = doc[i]
126     if 'MOLE FRACTIONS' in line and len(line) < 20:
127         j=2
128         newline=doc[i+j]
129         while True:
130             if len(newline) == 1:
131                 break
132             newline=doc[i+j]
133             for c in newline:
134                 if c in ['0','1','2','3','4','5','6','7','8','9'] and newline[newline.
                        index(c)-1] == ' ':
135                     ind=experiment[0].index(newline[0:newline.index(c)].strip())
136                     experiment[linecount][ind] = float(newline[newline.index(c):len(
                            newline)])
137             j +=1
138         linecount +=1
139 ceaout.close()
140
141 #~~~~~~~~~~~~ Write experiment array to data file ~~~~~~~~~~~~#
142 for line in experiment:
143     for item in line:
144         data.write(str(item)+', ')
145     data.write('\n')
146 data.close()
147
148 #~~~~~~~~~~~~~~~~~~~ Write gnuplot script ~~~~~~~~~~~~~~~~~~~#
149 gnuplot = open('./gnuplot.plt', 'w')
150
```

```
151 gnuplot.write('reset \nset term postscript enhanced eps \nset output "./density.eps" \
      nset xlabel "Equivalence Ratio {/Symbol F}" \nset xrange[0.4:1.35] \nset ylabel "
      Density (kg/m^3)" \nset key bot right \nset datafile separator "," \nset size 0.7 \
      nplot "./data.csv" using 1:4 with lp notitle \nreset \nset term postscript enhanced
      eps \nset output "./temperature.eps" \nset xlabel "Equivalence Ratio {/Symbol F}" \
      nset xrange[0.4:1.35] \nset ylabel "Temperature (K)" \nset key bot right \nset key
      spacing 1.25 \nset datafile separator "," \nset size 0.7 \nplot "./data.csv" using
      1:3 with lp notitle \nreset \nset term postscript enhanced eps color \nset output
      "./species.eps" \nset xlabel "Equivalence Ratio {/Symbol F}" \nset xrange[0.4:1.35]
      \nset ylabel "Mole Fraction, X_i" \nset key below \nset key spacing 1.25 \nset
      logscale y \nset pointsize 0.5 \nset yrange[0.001:1] \nset datafile separator "," \
      nplot "./data.csv" using 1:6 with lp title "'+str(experiment[0][5])+'" ,\\\n')
152 for i in range(7,len(experiment[0])):
153     gnuplot.write('     "./data.csv" using 1:'+str(i)+' with lp title "'+str(experiment
          [0][i-1])+'"'+' ,\\\n')
154 gnuplot.write('     "./data.csv" using 1:'+str(len(experiment[0]))+' with lp title "'+
      str(experiment[0][len(experiment[0])-1])+'"')
155 gnuplot.write('\nreset \nset term postscript enhanced eps \nset output "./gamma.eps" \
      nset xlabel "Equivalence Ratio {/Symbol F}" \nset xrange[0.4:1.35] \n\
156 set ylabel "Isentropic Exponent ({/Symbol g})" \nset key bot right \nset key spacing
      1.25 \nset datafile separator "," \n\
157 set size 0.65 \nplot "./data.csv" using 1:5 with lp notitle')
158
159 gnuplot.close()
160
161 #~~~~~~~~~~~~~~~~~~~~ Run gnuplot script ~~~~~~~~~~~~~~~~~~~~#
162 os.system('gnuplot gnuplot.plt')
```

F.2 CEA Calculations: Al-CuO constant-volume

```
#############################################################################
# Script to calculate, run and tabulate constant-volume calculations
# for Al-CuO using NASA's CEA
# G. Maines, 2013

import os
def inList(a, x): # List-check function
    for item in a:
        if x==item:
            return True
    return False

data = open('./data.csv', 'w') # Thermodynamic and species data w/ air
data2 = open('./data2.csv', 'w') # Thermodynamic and species data w/o air
ceainp = open('./ceafile.inp', 'w') # CEA input file w/ air
ceainp2 = open('./ceafile2.inp', 'w') # CEA input file w/o air

#~~~~~~~~~~~~~~~~~~~~ Material parameters ~~~~~~~~~~~~~~~~~~~~#
rAl=2700.0 # Density of Al (kg/m^3)
rCuO=6310.0 # Density of CuO (kg/m^3)
rAir=1.2 # Density of air (kg/m^3)
WAl=26.98 # Molar mass of Al (g/mol)
WCuO=79.55 # Molar mass of CuO (g/mol)
WAir=28.97 # Molar mass of air (g/mol)

#~~~~~~~~~~~~~~~~~~~~~~~~ Stoichiometry ~~~~~~~~~~~~~~~~~~~~~~~~#
NAl=2 # Number of moles of Al (mol)
NCuO=3 # Number of moles of CuO (mol)

#~~~~~~~~~~~~ Calculations based on stoichiometry ~~~~~~~~~~~~#
cAl=(NAl*WAl)/(NAl*WAl+NCuO*WCuO) # Mass fraction of Al
cCuO=(NCuO*WCuO)/(NAl*WAl+NCuO*WCuO) # Mass fraction of CuO
rTMD=1.0/(cAl/rAl+cCuO/rCuO) # Theoretical Max. Density (TMD, kg/m3)

#~~~~~~~~~~~~~~~~~~~~~~~~ Set up array ~~~~~~~~~~~~~~~~~~~~~~~~#
experiment=[]
experiment2=[]
experiment.append(['TMD','P','T','R','GAMMAs'])
experiment2.append(['TMD','P','T','R','GAMMAs'])

#~~~~~~~~~~~~~~~~~~~~ TMD loop calculations ~~~~~~~~~~~~~~~~~~~~#
TMD=100
while TMD > 0.00001:
    experiment.append([])
    experiment2.append([])
    rmix=(TMD/100.0)*rTMD # Mixture Density
    NAir=(rAir/WAir)*((NAl*WAl+NCuO*WCuO)/(rmix)-(NAl*WAl/(rAl))-(NCuO*WCuO/(rCuO))) #
        Number of moles of air (mol)
    reff=rmix+rAir*(100.0-TMD)/100.0 # Effective total mixture density, including air (
        kg/m^3)

```

```
50      #~~~~~~~~~~~~~~~~~ Write CEA input file ~~~~~~~~~~~~~~~~~#
51      ceainp.write('reac name AL(cr) moles = '+str(NAl)+' t(k)=298.15' + '\n' \
52      '      name CuO(cr) moles='+str(NCuO)+' t(k)=298.15' + '\n' \
53      '      name Air moles='+str(NAir)+' t(k)=298.15' + '\n\n' \
54      'prob case=TMD'+str(TMD)+' uv rho,kg/m^3='+str(reff) + '\n' \
55      'insert AL2O3(a)' + '\n' \
56      'output siunits' + '\n' \
57      'end' + '\n\n')
58      ceainp2.write('reac name AL(cr) moles = '+str(NAl)+' t(k)=298.15' + '\n' \
59      '      name CuO(cr) moles='+str(NCuO)+' t(k)=298.15' + '\n' \
60      'prob case=TMD'+str(TMD)+' uv rho,kg/m^3='+str(reff) + '\n' \
61      'insert AL2O3(a)' + '\n' \
62      'output siunits' + '\n' \
63      'end' + '\n\n')
64      experiment[len(experiment)-1].append(TMD)
65      experiment2[len(experiment2)-1].append(TMD)
66      TMD = TMD/1.2
67  ceainp.close()
68  ceainp2.close()
69
70  #~~~~~~~~~~~~~~~~~~~~~ Run CEA scripts ~~~~~~~~~~~~~~~~~~~~~~#
71  os.system('echo ceafile | ./CEA.out')
72  os.system('echo ceafile2 | ./CEA.out')
73
74  #~~~~~~~~~~~~~~~~~~ Open CEA output files ~~~~~~~~~~~~~~~~~~~#
75  ceaout=open('ceafile.out', 'r')
76  ceaout2=open('ceafile2.out', 'r')
77
78  #~~~~~~~~~~~~~~~~~~~~~ Search for data ~~~~~~~~~~~~~~~~~~~~~~#
79  doc=ceaout.readlines()
80  linecount=1
81  for i in range(0,len(doc)):
82      line=doc[i]
83      # Look for and add pressures to experiment array in rows
84      if 'P, BAR' in line:
85          for c in line:
86              if c in ['0','1','2','3','4','5','6','7','8','9']:
87                  experiment[linecount].append(float(line[line.index(c):len(line)])/10) #
                        Divide by 10 to convert to MPa
88                  break
89      # Look for and add temperatures to experiment array in rows
90      if 'T, K' in line:
91          for c in line:
92              if c in ['0','1','2','3','4','5','6','7','8','9']:
93                  experiment[linecount].append(float(line[line.index(c):len(line)]))
94                  break
95      # Look for and add densities to experiment array in rows
96      if 'RHO, KG/CU M' in line:
97          for c in line:
98              if c in ['0','1','2','3','4','5','6','7','8','9']:
99                  experiment[linecount].append(line[line.index(c):len(line)-1])
100                 break
101     # Look for and add isentropic exponents to new data file
```

```
102     if 'GAMMAs' in line:
103         for c in line:
104             if c in ['0','1','2','3','4','5','6','7','8','9']:
105                 experiment[linecount].append(line[line.index(c):len(line)-1])
106                 break
107     # Look for mole fractions, and add the name of each species to row 0, if it does not
          yet exist to experiment array
108     if 'MOLE FRACTIONS' in line and len(line) < 20:
109         j=2
110         newline=doc[i+j]
111         while True:
112             if len(newline)==1:
113                 break
114             newline=doc[i+j]
115             for c in newline:
116                 if c in ['0','1','2','3','4','5','6','7','8','9'] and newline[newline.
                      index(c)-1] == ' ':
117                     if not inList(experiment[0],newline[0:newline.index(c)].strip()):
118                         experiment[0].append(newline[0:newline.index(c)].strip())
119             j +=1
120         linecount +=1
121
122 #~~~~~~~~~~~~~~~~~ Append zeroes everywhere ~~~~~~~~~~~~~~~~~~#
123 for k in range(1,len(experiment)):
124     while len(experiment[k])<len(experiment[0]):
125         experiment[k].append('0')
126
127 #~~~ Add mole fractions to appropriate column for each TMD ~~~#
128 linecount=1
129 for i in range(0,len(doc)):
130     line=doc[i]
131     if 'MOLE FRACTIONS' in line and len(line) < 20:
132         j=2
133         newline=doc[i+j]
134         while True:
135             if len(newline)==1:
136                 break
137             newline=doc[i+j]
138             for c in newline:
139                 if c in ['0','1','2','3','4','5','6','7','8','9'] and newline[newline.
                      index(c)-1] == ' ':
140                     ind=experiment[0].index(newline[0:newline.index(c)].strip())
141                     experiment[linecount][ind] = float(newline[newline.index(c):len(
                          newline)])
142             j +=1
143         linecount +=1
144 ceaout.close()
145
146 #~~~~~~~~~~~~~~~~~ Repeat search for data2 ~~~~~~~~~~~~~~~~~~#
147 doc=ceaout2.readlines()
148 linecount=1
149 for i in range(0,len(doc)):
150     line=doc[i]
```

```
151     # Look for and add pressures to experiment array in rows
152     if 'P, BAR' in line:
153         for c in line:
154             if c in ['0','1','2','3','4','5','6','7','8','9']:
155                 experiment2[linecount].append(float(line[line.index(c):len(line)])/10) #
                        Divide by 10 to convert to MPa
156                 break
157     # Look for and add temperatures to experiment array in rows
158     if 'T, K' in line:
159         for c in line:
160             if c in ['0','1','2','3','4','5','6','7','8','9']:
161                 experiment2[linecount].append(float(line[line.index(c):len(line)]))
162                 break
163     # Look for and add densities to experiment array in rows
164     if 'RHO, KG/CU M' in line:
165         for c in line:
166             if c in ['0','1','2','3','4','5','6','7','8','9']:
167                 experiment2[linecount].append(line[line.index(c):len(line)-1])
168                 break
169     # Look for and add isentropic exponents to new data file
170     if 'GAMMAs' in line:
171         for c in line:
172             if c in ['0','1','2','3','4','5','6','7','8','9']:
173                 experiment2[linecount].append(line[line.index(c):len(line)-1])
174                 break
175     # Look for mole fractions, and add the name of each species to row 0, if it does not
          yet exist to experiment array
176     if 'MOLE FRACTIONS' in line and len(line) < 20:
177         j=2
178         newline=doc[i+j]
179         while True:
180             if len(newline)==1:
181                 break
182             newline=doc[i+j]
183             for c in newline:
184                 if c in ['0','1','2','3','4','5','6','7','8','9'] and newline[newline.
                        index(c)-1] == ' ':
185                     if not inList(experiment2[0],newline[0:newline.index(c)].strip()):
186                         experiment2[0].append(newline[0:newline.index(c)].strip())
187             j +=1
188         linecount +=1
189
190 #~~~~~~~~~~~~~~~~~ Append zeroes everywhere2 ~~~~~~~~~~~~~~~~~~#
191 for k in range(1,len(experiment2)):
192     while len(experiment2[k])<len(experiment2[0]):
193         experiment2[k].append('0')
194
195 #~~~ Add mole fractions to appropriate column for each TMD2 ~~~#
196 linecount=1
197 for i in range(0,len(doc)):
198     line=doc[i]
199     if 'MOLE FRACTIONS' in line and len(line) < 20:
200         j=2
```

```
201         newline=doc[i+j]
202         while True:
203             if len(newline)==1:
204                 break
205             newline=doc[i+j]
206             for c in newline:
207                 if c in ['0','1','2','3','4','5','6','7','8','9'] and newline[newline.
                        index(c)-1] == ' ':
208                     ind=experiment2[0].index(newline[0:newline.index(c)].strip())
209                     experiment2[linecount][ind] = float(newline[newline.index(c):len(
                            newline)])
210             j +=1
211         linecount +=1
212 ceaout2.close()
213
214 #~~~~~~~~~~~~ Write experiment arrays to data file ~~~~~~~~~~~~#
215 for line in experiment:
216     for item in line:
217         data.write(str(item)+', ')
218     data.write('\n')
219 data.close()
220 for line in experiment2:
221     for item in line:
222         data2.write(str(item)+', ')
223     data2.write('\n')
224 data2.close()
225
226 #~~~~~~~~~~~~~~~~~~ Write gnuplot script ~~~~~~~~~~~~~~~~~~#
227 gnuplot=open('./gnuplot.plt', 'w')
228 gnuplot.write('reset \nset term postscript enhanced eps \nset output "./pressure.eps" \
        nset border linewidth 1.5 \nset xlabel "{/Symbol r}/{/Symbol r}_{TMD} (%)" \nset
        xrange[0.01:100] \nset ylabel "Pressure (MPa)" \nset pointsize 0.5\nset key bot
        right \nset key spacing 1.25 \nset logscale xy\nset datafile separator "," \nset
        size 0.45 \nplot "./data.csv" using 1:2 with l lt 2 title "With air" ,\\\n"./data2.
        csv" using 1:2 with l lt 4 title "Without air" \nreset \nset term postscript
        enhanced eps \nset output "./temperature.eps" \nset border linewidth 1.5 \nset
        pointsize 0.5\nset xlabel "{/Symbol r}/{/Symbol r}_{TMD} (%)" \nset xrange[0.01:100]
         \nset ylabel "Temperature (K)" \nset key bot right \nset key spacing 1.25 \nset
        logscale x\nset datafile separator "," \nset size 0.45 \nplot "./data.csv" using 1:3
         with l lt 2 title "With air" ,\\\n "./data2.csv" using 1:3 with l lt 4 title "
        Without air" \nreset \nset term postscript enhanced color eps \nset output "./
        species.eps" \nset xlabel "{/Symbol r}/{/Symbol r}_{TMD} (%)" \nset border linewidth
         1.5 \nset xrange[0.01:10] \nset ylabel "Mole Fraction, X_i" \nset yrange[0.001:]\
        nset key below \nset key spacing 1.25 \nset logscale xy \nset pointsize 0.5 \nset
        datafile separator "," \nset size 0.7 \nset key spacing 0.75 \nset key font ",10" \
        nplot "./data.csv" using 1:6 with lp title "'+str(experiment[0][5])+'" ,\\\n')
229 for i in range(7,len(experiment[0])):
230     gnuplot.write('     "./data.csv" using 1:'+str(i)+' with lp title "'+str(experiment
            [0][i-1])+'"'+' ,\\\n')
231 gnuplot.write('     "./data.csv" using 1:'+str(len(experiment[0]))+' with lp title "'+
        str(experiment[0][len(experiment[0])-1])+'" \n')
232 gnuplot.write('\nreset \nset term postscript enhanced color eps \nset output "./species-
        noair.eps" \nset xlabel "{/Symbol r}/{/Symbol r}_{TMD} (%)" \nset border linewidth
```

```
    1.5 \nset xrange[0.01:10] \nset ylabel "Mole Fraction, X_i" \nset yrange[0.001:]\
    nset key below \nset key spacing 1.25 \nset logscale xy\nset pointsize 0.5 \nset
    datafile separator "," \nset size 0.7 \nset key spacing 0.75 \nset key font ",10" \
    nplot "./data2.csv" using 1:6 with lp title "'+str(experiment2[0][5])+'" ,\\\n')
for i in range(7,len(experiment2[0])):
    gnuplot.write('     "./data2.csv" using 1:'+str(i)+' with lp title "'+str(
        experiment2[0][i-1])+'"'+' ,\\\n')
gnuplot.write('     "./data2.csv" using 1:'+str(len(experiment2[0]))+' with lp title "'+
    str(experiment2[0][len(experiment2[0])-1])+'"')
gnuplot.close()

#~~~~~~~~~~~~~~~~~~~~ RUN GNUPLOT SCRIPT ~~~~~~~~~~~~~~~~~~~~#
os.system('gnuplot gnuplot.plt')
```

F.3 Constant-volume pressure data analysis

```
#############################################################################
# Script to filter pressure signals and calculate
# pressurization rates of constant-volume reactions
# G. Maines, 2013

alpha1=0.2
alpha2=0.5
output2=open("./output.txt","w")
output2.write('Test'+'\t'+'%TMD'+'\t'+'Pmax(kPa)'+'\t'+'Prate(MPa/s)'+'\n')
TMDs=[1.0227,1.8309,0.9728,1.2222,0.4689,1.4467,0.7333,1.0077,2.5692,
1.6662,2.0703,1.5715,1.8159,2.2699,3.5670,4.2155,2.1701,2.2312,
2.4245,3.0531,1.1823,3.5270,5.2881,2.0903,0.7284,0.4739,2.9583]
for x in range(1,28):
    output=open("./T"+str(x)+"-Filtered.txt","w")
    file="./T"+str(x)+".txt"
    my_file=open(file,"r")
    time=[]
    pressure=[]
    pfiltered=[0]
    dPdt=[0]
    dPdtf=[0]
    for line in my_file:
        items=line.strip().split("\t")
        time.append(float(items[0]))
        pressure.append(float(items[1]))
    # Filtering and Calculating Pressurization Rate
    for i in range(1,len(pressure)):
        pfiltered.append(pressure[i]*alpha1+(1-alpha1)*pfiltered[i-1])
        dPdt.append((pfiltered[i]-pfiltered[i-1])/(time[i]-time[i-1]))
        dPdtf.append(dPdt[i]*alpha2+(1-alpha2)*dPdtf[i-1])
        output.write(str(time[i])+'\t'+str(pressure[i])+'\t'+str(pfiltered[i])+'\t'+str(
            dPdt[i])+'\t'+str(dPdtf[i])+'\n')
    pmax=max(pfiltered)
    dPdtmax=max(dPdtf)/1000 # Convert to MPa/s
    output2.write(str(x)+'\t'+str(TMDs[x-1])+'\t'+str(pmax)+'\t'+str(dPdtmax)+'\n')
```

F.4 Underwater pressure data analysis

```
import numpy as np
import scipy
from subprocess import call
output2 = open("./output.txt", "w")
output2.write('Test' + '\t' + 'Pmax,s(kPa)' + '\t' + 'Pmax,l(kPa)' + '\t' + 'Impulse(kPa-s)' + '\n')
for x in range(1,41):
    if (x == 12 or x == 22 or x == 24 or x == 25 or x == 26): # Tests 12,22,24,25,26 have no pressure data
        continue
    output = open("./T" + str(x) + "-Modified.txt", "w")
    file = "./T" + str(x) + ".txt"
    my_file = open(file, "r")
    time = []
    pressure1 = []
    pressure2 = []
    pressure3 = []
    pmaxshort = 0
    flag = 0
    flag2 = 0
    # Withdraw time and free-field pressure from the input file
    for line in my_file:
        if len(line) < 4: # Avoid blank lines
            continue
        items = line.strip().split("\t") # Strip lines for items
        if flag == 0: # Find correction factors
            correction1 = abs(float(items[1]))
            correction2 = abs(float(items[2]))
            correction3 = abs(float(items[3]))
            flag = 1
        time.append(float(items[0])) # Append time
        pressure1.append(float(items[1])+correction1) # Append corrected pressure
        pressure2.append(float(items[2])+correction2) # Append corrected pressure
        pressure3.append(float(items[3])+correction3) # Append corrected pressure
    # Write out all data
    for i in range(0,len(time)):
        # Write data to new file
        output.write(str(time[i]-time[0]) + '\t' + str(pressure1[i]) + '\t' + str(pressure2[i]) + '\t' + str(pressure3[i]) + '\n')
    # Calculate pmax,short for freefield
    for i in range(0,len(time)):
        if (pressure3[i] > 100 and pressure3[i] > pmaxshort and flag2 == 0):
            pmaxshort = pressure3[i]
            if (pressure3[i+1] < pressure3[i]):
                flag2 = 1
    # Calculate the point at which pressure dips below 50 kPa
    for i in range(500,len(time)):
        if (pressure3[i] < 50):
            integrationindex = i
            break
    # Calculate impulse
```

```
49      impulse = 0
50      for i in range(0,integrationindex):
51          impulse = impulse + ((time[i+1]-time[i])/2)*(pressure3[i+1]+pressure3[i])
52      pmaxlong = max(pressure3)
53      output2.write(str(x) + '\t' + str(pmaxshort) + '\t' + str(pmaxlong) + '\t' + str(
            impulse) + '\n')
54
55      gnuplot = open("./gnuplot.plt", "w")
56      gnuplot.write("set term postscript enhanced colour eps\n\
57      set ylabel \"Pressure (kPa)\"\n\
58      set xlabel \"Time ({/Symbol m}s)\"\n\
59      set output \"./Plots/T"+str(x)+"-close.eps\"\n\
60      set xrange[0:500]\n\
61      plot \"T"+str(x)+"-Modified.txt\" using ($1*1000000):2 w l title \"Wall 1\" ,\\\n\
62      \"T"+str(x)+"-Modified.txt\" using ($1*1000000):3 w l title \"Wall 2\" ,\\\n\
63      \"T"+str(x)+"-Modified.txt\" using ($1*1000000):4 w l title \"Free-field\"\n\
64      set output \"./Plots/T"+str(x)+"-far.eps\"\n\
65      set xrange[0:2500]\n\
66      plot \"T"+str(x)+"-Modified.txt\" using ($1*1000000):2 w l title \"Wall 1\" ,\\\n\
67      \"T"+str(x)+"-Modified.txt\" using ($1*1000000):3 w l title \"Wall 2\" ,\\\n\
68      \"T"+str(x)+"-Modified.txt\" using ($1*1000000):4 w l title \"Free-field\" ")
69      gnuplot.close()
70      call("gnuplot gnuplot.plt", shell=True)
```